ARTICLE IN PRESS
ATMOS-02122; No of Pages 52

Atmospheric Research xxx (2010) xxx–xxx

Contents lists available at ScienceDirect

Atmospheric Research

journal homepage: www.elsevier.com/locate/atmos

Towards a new synthesis for atmospheric dynamics: Space–time cascades

S. Lovejoy [a,b,*], D. Schertzer [c,d]

[a] Physics, McGill University, 3600 University st., Montreal, Que., Canada
[b] GEOTOP, UQAM, CP 8888, Succ. Centre Ville, Montreal, Que., Canada H3C 3P8
[c] Université Paris-Est, ENPC/CEREVE, 77455, Marne-la-Vallée Cedex 2, France
[d] Météo France, 1 Quai Branly, 75007 Paris, France

ARTICLE INFO

Article history:
Received 2 February 2009
Accepted 21 November 2009
Available online xxxx

ABSTRACT

In spite of the unprecedented quantity and quality of meteorological data and numerical models, there is still no consensus about the atmosphere's elementary statistical properties as functions of scale in either time or in space. This review paper proposes a new synthesis based on a) advances in the last 25 years in nonlinear dynamics, b) a critical re-analysis of empirical aircraft and vertical sonde data, c) the systematic scale by scale, space–time exploitation of high resolution remotely sensed data and d) the systematic re-analysis of the outputs of numerical models of the atmosphere including reanalyses, e) a new turbulent model for the emergence of the climate from "weather" and climate variability. We conclude that Richardson's old idea of scale by scale simplicity — today embodied in multiplicative cascades — can accurately explain the statistical properties of the atmosphere and its models over most of the meteorologically significant range of scales, as well as at least some of the climate range. The resulting space–time cascade model combines these nonlinear developments with modern statistical analyses, it is based on strongly anisotropic and intermittent generalizations of the classical turbulence laws of Kolmogorov, Corrsin, Obukhov, and Bolgiano.

Contents

---

* Corresponding author. Physics, McGill University, 3600 University st., Montreal, Que., Canada.
E-mail address: lovejoy@physics.mcgill.ca (S. Lovejoy).

doi:10.1016/j.atmosres.2010.01.004

Please cite this article as: Lovejoy, S., Schertzer, D., Towards a new synthesis for atmospheric dynamics: Space–time cascades, Atmos. Res. (2010), doi:10.1016/j.atmosres.2010.01.004

1. Introduction

1.1. The golden age paradox

As little as 25 years ago, few atmospheric data sets spanned more than two orders of magnitude in scale;yet they were challenging even to visualize. Global models had even lower resolutions, yet required heroic computer efforts. The atmosphere was seen through a low resolution lens. Today, in situ and remote data routinely span scale ratios of 10^3–10^4 in space and/or time scales and operational models are not far behind. We are now beginning to perceive the true complexity of atmospheric fields which span ratios of over 10^{10} in spatial scales (the planet scale to the dissipation scale).

Increasingly we are faced with the problem of achieving a scale by scale understanding of complex hierarchies of structures embedded within structures. One (still) popular approach is through phenomenological models based on subjectively defined morphologies or other ad hoc features; in some schools new models and mechanisms are introduced every factor of 2 or so in scale. A more theoretically satisfying approach is via statistical physics, i.e. turbulence theory. The still “standard” turbulence model was elaborated at the end of the 1960s (see e.g. Monin, 1972's influential book); it was

Please cite this article as: Lovejoy, S., Schertzer, D., Towards a new synthesis for atmospheric dynamics: Space–time cascades, Atmos. Res. (2010), doi:10.1016/j.atmosres.2010.01.004

critically based on the theory of two dimensional isotropic turbulence (Kraichnan, 1967; Leith, 1968) with (Charney, 1971)'s extension to geostrophic turbulence. This classical picture of the atmosphere consists of a 3D isotropic turbulence at small scales and a 2D isotropic turbulence at large scales with the two separated by a low energy “meso-scale gap” somewhere near the 10 km scale thickness. In addition to the scale at which this “dimensional transition” supposedly occurs, in principle two additional larger scales are needed: one for the 2-D energy (velocity variance) flux injection, another for the enstrophy (vorticity variance) flux injection. With all these scales to play with, it is easy to concoct complicated models. The more realistic proposals such as the “Gage–Lilly” model (Lilly, 1989) involve i) a small scale isotropic 3D turbulence regime with energy cascading to smaller scales, ii) an intermediate downscale 2-D isotropic enstrophy cascade regime and iii) a large scale, 2-D isotropic upscale energy cascade regime (see the schematic Fig. 4d and Lilly, 1983; Gage and Nastrom, 1986; Lilly, 1989; Gifford, 1988; Bartello, 1995; Ngan et al., 2004).

One might have expected that with today's quantity and quality of satellite, aircraft and other remote and in situ measurements, that this basic picture of the atmosphere would by now have been either accepted and then refined or rejected and then replaced, but this has not been the case; indeed, the status of this hierarchy of isotropic turbulence models is still under debate today. On the one hand, empirically the situation in the horizontal is still contradictory (see the discussion below) on the other hand, theoretically the finding that the 3D regime may destabilize (“three dimensionalize”) the 2D regime (Bartello, 1995; Ngan et al., 2004), raises issues about its internal consistency (see e.g. Takayashi et al., 2006; Hamilton et al., 2008 for a recent numerical investigations).

The behaviour of the horizontal wind is bad enough, but it gets worse. Even if we continue to restrict our attention to the horizontal, the 2D/3D models are clearly in trouble when considering scalar fields such as temperature or humidity (or presumably clouds and their radiances). This is because — unlike the vector wind field with two quadratic invariants (energy and enstrophy) — these fields have only one quadratic invariant and so the 2D/3D transition would be dramatic, and empirically, such drastic transitions are not observed anywhere near the purported 2D/3D transition scales (Schertzer and Lovejoy, 1985b).

If we consider instead the vertical structure of the atmosphere, the situation is even more embarrassing. This is because vertical spectra in three dimensional isotropic turbulence are totally different from those in 2D turbulence so that the violations of the predictions of the classical 2D/3D picture are all the more flagrant. Indeed, starting in the 1980's experiments claimed that the turbulence was anisotropic but scaling (Van Zandt, 1982; Schertzer and Lovejoy, 1985b), and during the 1990's for the key horizontal wind, the mainstream experimental community favoured a k_z^{-3} model for the vertical spectrum along with a $k_x^{-5/3}$ horizontal spectrum, and this out to scales $\gg 10$ km (k_z, k_x are vertical and horizontal wavenumbers respectively), i.e. a fundamentally anisotropic model. The most popular models reproducing this behaviour are the Saturated Wave Theory (SWT, Dewan, 1997), and the Diffusive Filtering Theory (DFT, Gardner, 1994). But both the SWT and DFT are based on (quasi) linear gravity waves which are at best only weakly turbulent so that the divorce between the dominant strongly nonlinear isotropic theories and the dominant weakly nonlinear and anisotropic interpretations of the experimental data is almost total.

1.2. Is the atmosphere irreducibly complex?

These inconclusive attempts to understand the scale by scale structure of the atmosphere have reinforced the idea that the atmosphere is irreducibly complex, that it is only amenable to brute force numerics. Yet, the history of science is replete with examples showing that apparent complexity can hide simplicity at another level. In the atmosphere it is ironic that the possibility of scale by scale simplicity — through the emergence of cascade processes — was first posed by precisely the pioneer of the brute force approach, Lewis F. Richardson (Richardson, 1926) (see Fig. 1 for a modern schematic of a cascade).

This paper is an overview of some recent work addressing this brute force complexity/scale by scale simplicity dichotomy i.e. the cascade alternative; it is timely for several reasons. The first is that the development of a multiscale synthesis based on an anisotropic cascade alternative to the dominant 2D isotropic/3D isotropic picture has reached a point where — profiting from the golden age — it has amassed a large and compelling body of empirical evidence in its favour. The second is that it can easily and naturally explain the most comprehensive existing empirical studies — and this without resorting to ad hoc/speculative models or reasoning. The third is that recent studies of large scale numerical models of the atmosphere show that these models are themselves accurately described by multiplicative cascade processes (Stolle, 2009; Stolle et al., submitted for publication) so that if we reject cascades, then we also reject the most advanced and prestigious numerical models. The final reason is that the stochastic cascade approach is increasingly needed for applications. This is particularly true since the last twenty years has witnessed a revolution in numerical weather prediction. Twenty years ago the goal of weather forecasting was to determine the (supposedly unique) state of the atmosphere at some time in the future, whereas today, *ensemble forecasting systems* have instead the goal of determining the possible states of tomorrow's weather including their *probabilities of occurrenc*e. This new goal therefore corresponds to a transition from deterministic to stochastic forecasts. Today's ensemble forecasting systems therefore require knowledge of the underlying stochastic structure of the deterministic equations, knowledge that the cascades conveniently provide.

1.3. The alternative: multiplicative cascades

During the 1960's and early 1970's, intermittency was increasingly acknowledged as an important phenomenon, but its effect was usually considered small, associated with small corrections to the spectral exponents. The main statistical models (such as those used in statistical closures) assumed “quasi-Gaussian statistics”. In order to obtain a Gaussian model with the classical Kolmogorov 1941 law $\Delta v = \varepsilon^{1/3}\Delta x^{1/3}$ (for velocity fluctuations Δv over distances Δx) — the real space equivalent of the Fourier space $E(k) \approx k^{-5/3}$ — one simply takes the energy flux ε as a Gaussian white noise process and give $\varepsilon^{1/3}$ a (fractional) integration of order 1/3 (i.e., a power law filter of

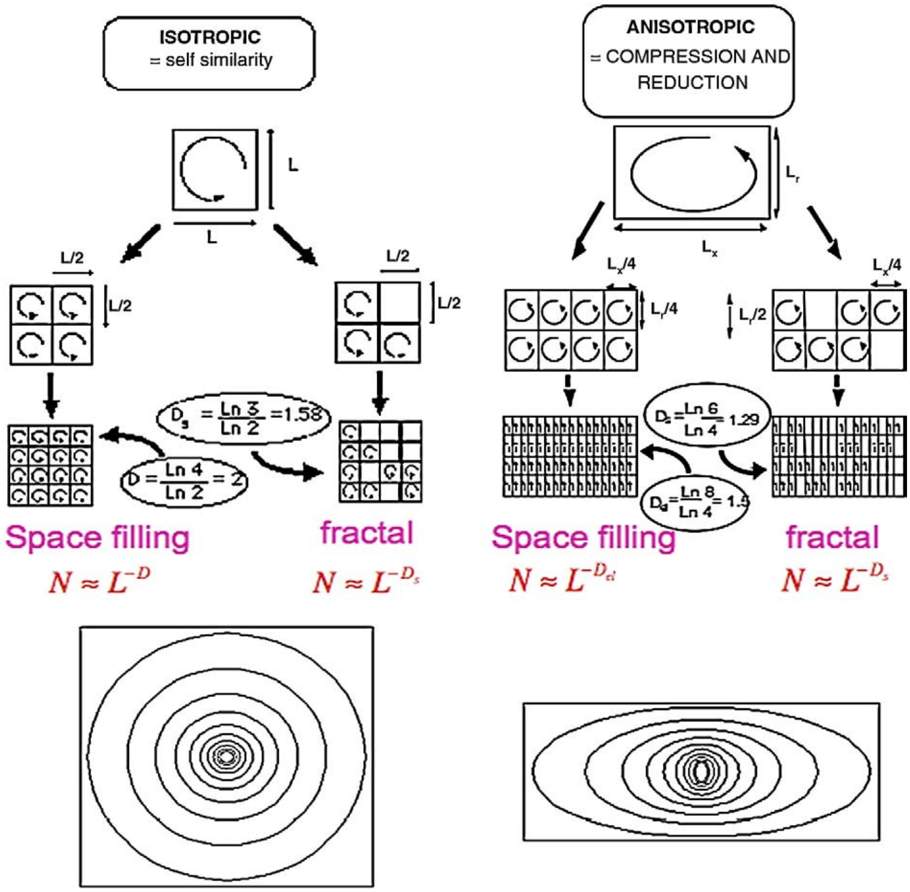

Fig. 1. The left of the figure shows a schematic of an isotropic cascade. Due to nonlinear interactions with other eddies or due to into instability, a large eddy/structure (indicated as a square) breaks up into daughter eddies (smaller squares). Following the left most arrow the energy flux is redistributed uniformly in space, the result is a homogeneous (non fractal) cascade. Following the right hand arrow, at each cascade step, we randomly allow one eddy in four to be "dead", the result is that turbulence is only active on a fractal set. At the bottom, we see the average shape as a function of scale of more realistic (isotropic eddies). The right hand column is the same except that it shows an anisotropic cascade, a model of a vertical cross-section of the atmosphere (on the left a homogeneous, on the right, inhomogeneous, fractal model). The degree of stratification is characterized by an elliptical dimension $D_{el} = 1.5$ in the example. Adapted from (Schertzer and Lovejoy, 1987).

order −1/3): the resulting v is a "fractional Brownian motion". In order to take into account intermittency, it suffices to replace the Gaussian ε in the above model by the result of a multiplicative cascade; this is the Fractionally Integrated Flux model (Schertzer and Lovejoy, 1987), see Section 4.4 for some mathematical details.

Fig. 1 shows the basic cascade idea: due to instability and/or interactions with other structures, an "eddy" breaks up into "daughter" eddies passing on (conserved) fluxes to the smaller structures. These phenomenological models are based on three basic aspects of turbulent fluid dynamics; a) the existence of a quantity conserved by the nonlinear terms in the equations, b) the existence of a wide range without characteristic scales, c) the fact that interactions are strongest between structures of neighbouring size: "locality in Fourier space". Some comments are needed. First, the conserved quantity is usually taken as the energy and/or enstrophy flux; sometimes potential enstrophy flux, but the cascade notion is much more general. Second, the notion of a scaling range is usually reduced to that of an "inertial range", i.e. a range without sources or sinks of flux, but this is also unnecessarily restrictive: it is sufficient that the sources and sinks are themselves scaling, hence the significance of the cascade study of the short and long wave radiances (Section 2, Lovejoy et al., 2009a). In other words, the scaling symmetries are taken as the basis and these are not restricted to isotropic scale symmetries. Third, while 3D turbulence is local in Fourier space, 2D turbulence is not, so that the finding of large scale multiplicative cascades is prima facie evidence against the relevance of 2D turbulence models to the atmosphere

Fig. 2. a: A schematic of a two-state (binomial, "α model") cascade in 1-D showing the first step in the cascade with randomly chosen boosts by factor $\lambda_0^{\gamma+}$ and decreases by factor $\lambda_0^{\gamma-}$. b: 2D extension of the α model shown in panel a (figure from Wilson et al., 1991). As we move from top to bottom on the left side, more and more cascade steps are added. We see that since on average the integral under the spikes is conserved so that while the strength of the spikes tends to increase at each step, this effect is offset by low intensities (low ε) throughout most of the region. On the right we indicate the "dressed" cascade obtained by integrating the completed "bare" cascade over the same scales. Note that occasionally the spikes on the right are much higher, due to the small scale activity which is not fully "averaged out" this extra activity is associated with the divergence of statistical moments, self-organized critical behaviour.

Please cite this article as: Lovejoy, S., Schertzer, D., Towards a new synthesis for atmospheric dynamics: Space–time cascades, Atmos. Res. (2010), doi:10.1016/j.atmosres.2010.01.004

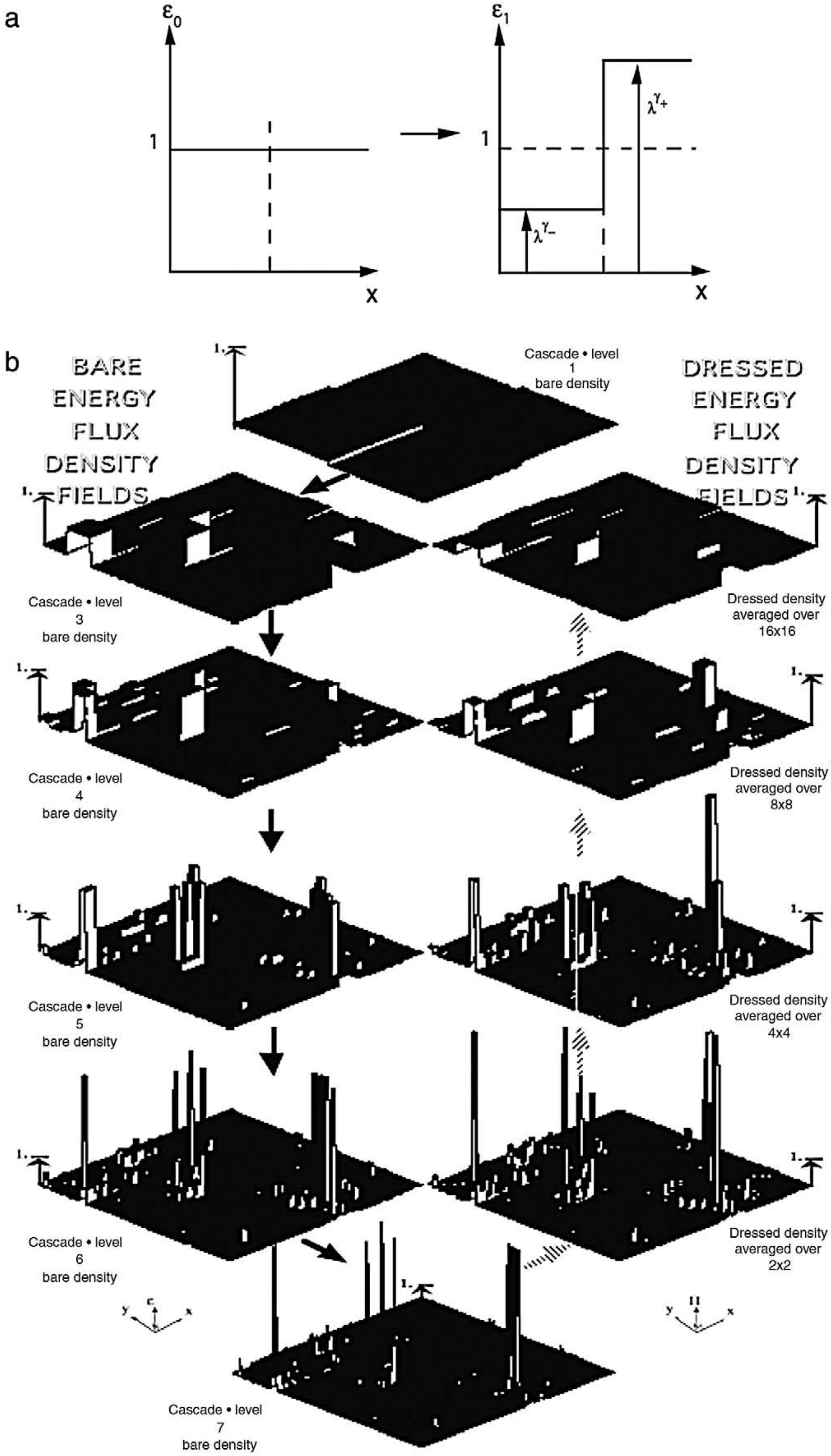

Please cite this article as: Lovejoy, S., Schertzer, D., Towards a new synthesis for atmospheric dynamics: Space–time cascades, Atmos. Res. (2010), doi:10.1016/j.atmosres.2010.01.004

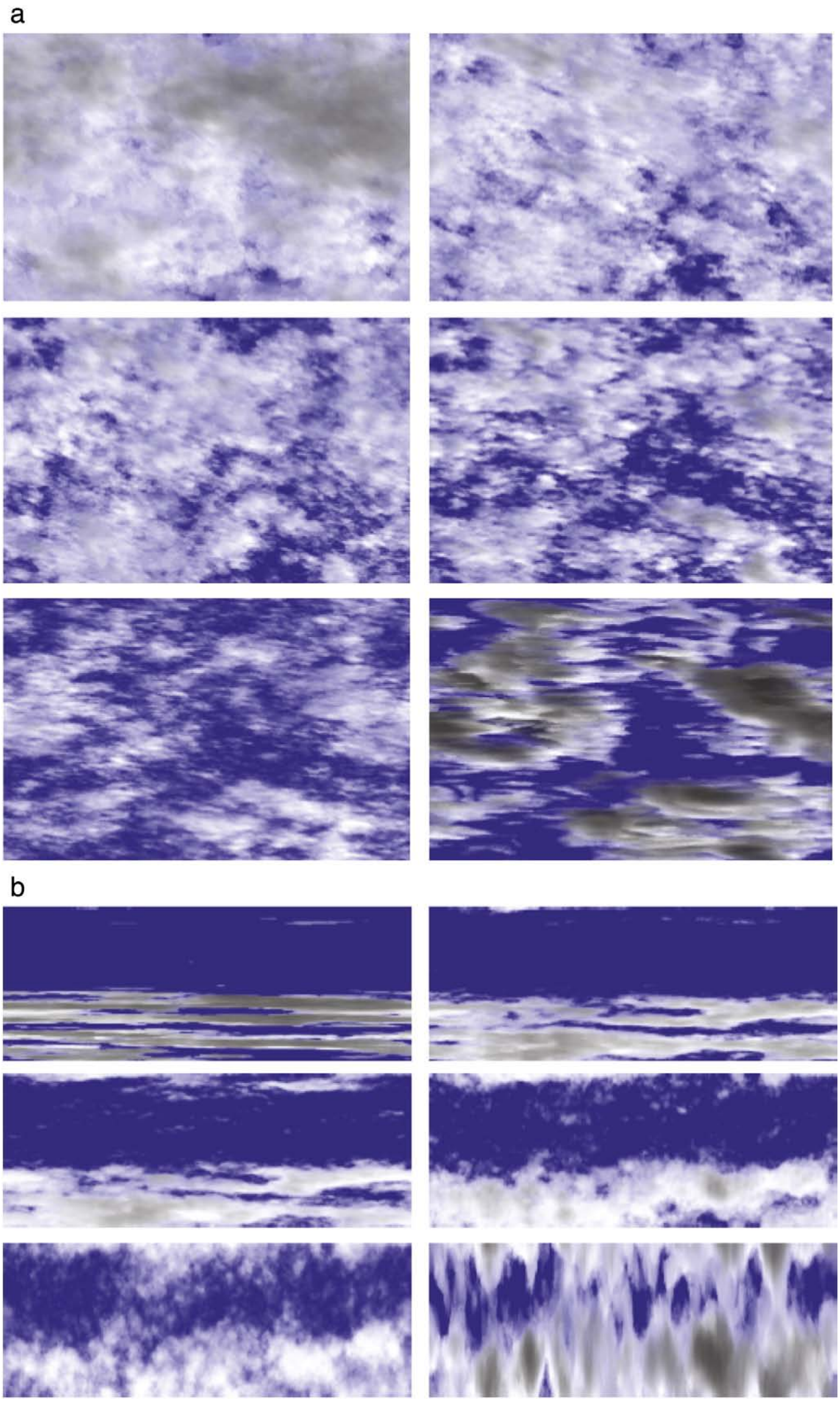

Please cite this article as: Lovejoy, S., Schertzer, D., Towards a new synthesis for atmospheric dynamics: Space–time cascades, Atmos. Res. (2010), doi:10.1016/j.atmosres.2010.01.004

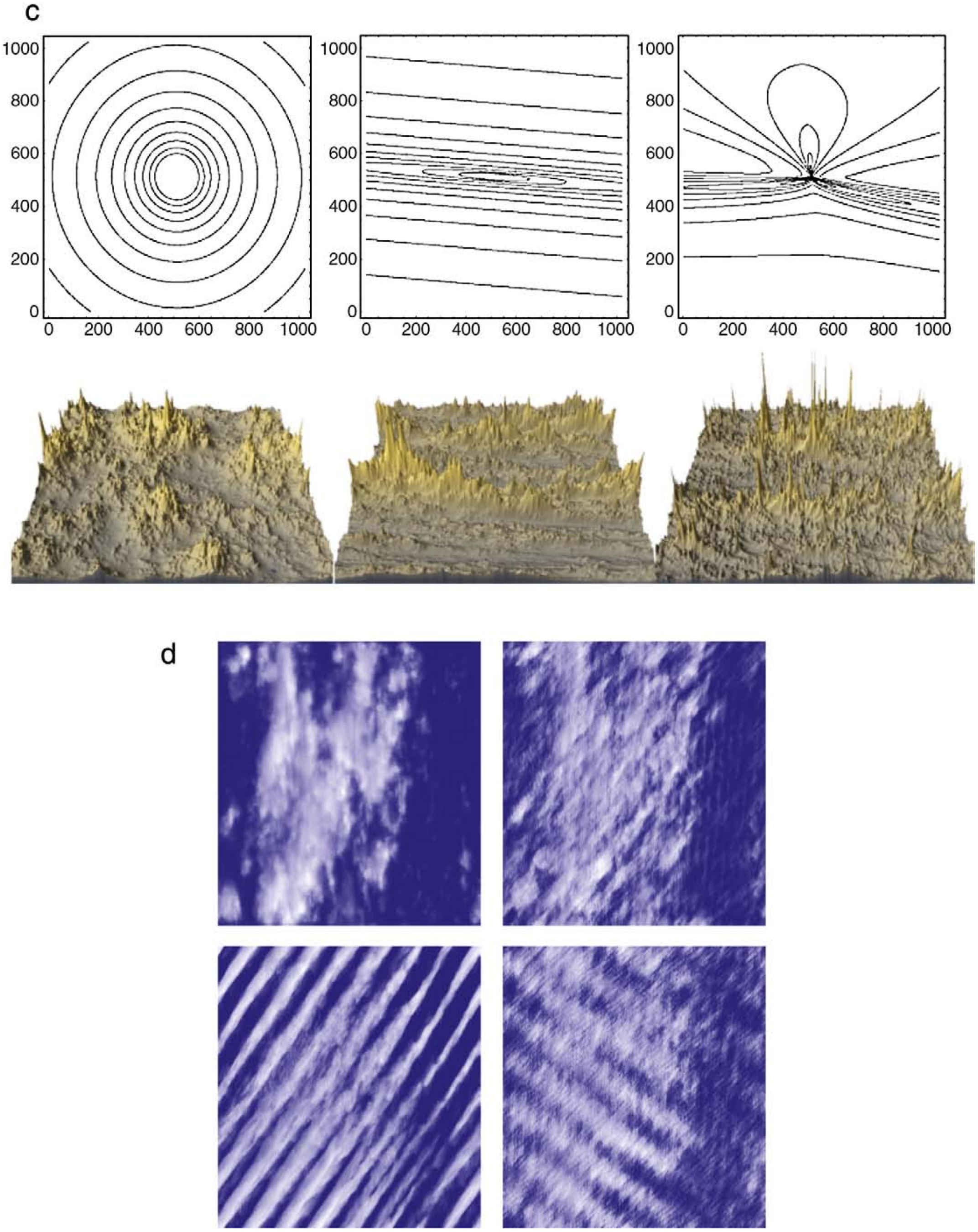

Fig. 3. a: Examples of continuous in scale anisotropic multifractals in 3D showing the effect of changing the sphero-scale (Section 3) on multifractal models of clouds. Only single scattering is used for the radiative transfer rendition. The cloud parameters are: $\alpha = 1.8$, $C_1 = 0.1$, $H = 1/3$, $r =$ vertical/horizontal aspect ratio at the horizontal sphero-scale, top to bottom : $r = 1/4$, 1, 4, left to right, horizontal sphero-scale $= 1$, 8. For technical details, see (Lovejoy and Schertzer, in press). b: The same clouds, but a side view showing how the stratification at each fixed scale changes with changing sphero-scale. However, the exponent ($H_z = 5/9$, $D_{el} = 23/9$) characterizing the differential (scale by scale) vertical stratification is the same in each case. c: The bottom row shows multifractal simulations of topography; the parameters ($\alpha = 1.8$, $C_1 = 0.12$, $H = 0.7$,) are those empirically determined (as discussed in Section 2.4); the only difference is the type of scaling anisotropy. The top row shows the corresponding scale functions which define the notion of scale. The left is a self-similar model (isotropic), the middle is linear GSI with generator $G = \begin{pmatrix} 0.8 & -0.05 \\ 0.05 & 1.2 \end{pmatrix}$ and with a canonical scale function, the right has the same G as the middle but a more complicated unit ball (adapted from Gagnon et al., 2006). d: This figure shows a model using scale functions respecting the anisotropic (vertically stratified) extension of the Corrsin–Obukhov scaling laws but which are localized only in space, not in space–time (i.e. they are wave-like). The degree of space–time delocalization increases clockwise from the upper left. The parameters are, $H = 0.33$, $C_1 = 0.1$, $\alpha = 1.8$. There is a small amount of differential anisotropy characterized by $G = \begin{pmatrix} 0.95 & -0.02 \\ 0.02 & 1.05 \end{pmatrix}$. The random seed is the same in all cases so that one can see how structures become progressively more and more wave-like while retaining the same scaling symmetries, close to observations (reproduced from (Lovejoy et al., 2008b)).

Please cite this article as: Lovejoy, S., Schertzer, D., Towards a new synthesis for atmospheric dynamics: Space–time cascades, Atmos. Res. (2010), doi:10.1016/j.atmosres.2010.01.004

(nevertheless the existence of multiplicative cascades in pure 2D turbulence cannot be ruled out).

In much of the atmospheric literature, cascades are invoked at a somewhat vague conceptual level. In conjunction with dimensional arguments based on the scale by scale conserved turbulent flux (primarily the energy flux ε and the enstrophy flux η) they are nevertheless able to determine the basic (nonintermittent) spectra (the classical $k^{-5/3}$, k^{-3} respectively) and with the help of statistical mechanical arguments, they can determine the cascade direction (downscale for energy flux in 3D and enstrophy flux in 2D, upscale for energy flux in 2D), see e.g. Chen and Wiin-Nielsen (1978), Boer and Shepherd (1983), Bartello (1995), Strauss and Ditlevsen (1999), Ngan et al. (2004) and Fig. 4d.

Further progress requires the development of explicit, multiplicative cascade models (Novikov and Stewart, 1964; Yaglom, 1966; Mandelbrot, 1974). We therefore digress to explain how these explicit cascade models work. Consider Fig. 2a which shows the development of a 1-D, 2-state discrete in scale cascade developed with discrete cascade ratio $\lambda_0 = 2$. The unit interval is divided into λ_0 parts and then an independent random multiplier $\mu\varepsilon$ is chosen for each half (each “daughter eddy”). In the 2-state process shown, the multiplier is one of two possible values $\mu\varepsilon = \lambda_0^{\gamma^+}$ or $\mu\varepsilon = \lambda_0^{\gamma^-}$ with $\gamma^+ > 0$, $\gamma^- < 0$ corresponding to boosts or decreases respectively. To enforce scale by scale conservation of the flux, we require the average multiplier to be normalized. Using ensemble (“canonical”) conservation, $<\mu\varepsilon> = 1$ we obtain the “α model” (Schertzer and Lovejoy, 1985b). If the much stronger “microcanonical” conservation $(\mu\varepsilon_{\text{left}} + \mu\varepsilon_{\text{right}})/2 = 1$ is used — as it is in much of the physics literature — the result is the “p model” (Meneveau and Sreenivasan, 1987). Due to the strong limitations that microcanonical conservation implies — they are unrealistically “calm” — we will not discuss microcanonical models further. The process of division and random multiplication is then continued to smaller and smaller scales, this limit is discussed below, see Fig. 2b for a 2D example.

By the mid 1980's, it was recognized that these multiplicative cascade models were quite general, leading to the following generic statistical behaviour:

$$\langle \varepsilon_\lambda^q \rangle = \lambda^{K(q)} \tag{1}$$

where $\lambda \geq 1$ is the overall ratio of scales (largest over smallest; $\lambda = \lambda_0^n$ for n steps of a model discrete in scale with scale ratio λ_0 per step) over which the cascade has developed and ε_λ is the scale by scale conserved flux. To see this, note that after n steps, at a given location in the space, the field ε_n is given by $\varepsilon_n = \varepsilon_0 \prod_{i=1}^{n} \delta\varepsilon_i$ while the overall scale range is $\lambda = \lambda_o^n$. If $\langle \delta\varepsilon^q \rangle = \lambda_0^{K(q)}$ we easily see that $\langle \varepsilon_n^q \rangle = \lambda^{K(q)}$ (Eq. (1)). $K(q)$ is the moment scaling function which contains the statistical information about the process. In comparison, the quasi-Gaussian (nonintermittent) classical model is the (trivial) special case $K(q) = 0$.

Before continuing, a word about notation. In the following, we use the codimension multifractal formalism (Schertzer and Lovejoy, 1987; Schertzer et al., 1997) which for stochastic multifractals has advantages when compared with the more common dimension multifractal formalism (Halsey et al., 1986) which was developed for applications to low dimensional deterministic chaos. In the codimension formalism $K(q)$ quantifies the multiscaling of the density of the turbulent flux; in the dimension formalism, the corresponding quantity, $\tau(q)$ characterizes the D-dimensional integral of the density (D is the dimension of space or subspace of integration); the two are thus related by $\tau(q) = (q-1)D - K(q)$. The codimension formalism has the advantage of being independent of the dimension of space (D) and is thus well adapted to stochastic multifractals processes which are defined on infinite dimensional probability spaces ($D \to \infty$).

At this very general level, $K(q)$ need only satisfy certain loose requirements, principally that it is convex and — due to the scale by scale conservation $<\varepsilon_\lambda> = 1$; $K(1) = 0$. However an appropriate multiplicative extension of the central limit theorem shows that under fairly general circumstances it is of the “universal multifractal” type, see the debate in Schertzer and Lovejoy (1987, 1997). Since the cascade is multiplicative, its logarithm $\Gamma_n = \log\varepsilon_n$, the “generator” is additive: $\Gamma_n = \Gamma_0 + \sum_i^n \Delta\Gamma_i$ (with $\Delta\Gamma_i = \log(\delta\varepsilon_i)$). It is therefore not surprising that — due to the additive central limit theorem for the sums of identical independently distributed random variables — there exist specific (stable, attractive) “universal” forms for the exponent $K(q)$ characterized by two basic parameters:

$$K(q) = \frac{C_1}{\alpha - 1}(q^\alpha - q) \tag{2}$$

Fig. 4. a: The enstrophy spectrum ($= n^2 E(n)$ where $E(n)$ is the wind spectrum and n is the principal spherical harmonic wavenumber), adapted from Boer and Shepherd 1983. The three curves are from January data; the solid line is for the vertically integrated atmosphere, the lines indicated stationary, (spatial spectrum of the monthly average) and the transient is the deviation from the monthly average. Over the range $n \approx 5$ to 30 (700–4000 km) the exponents of the spectra of the transient and vertically averaged atmosphere are extremely close to the vertical value $\beta \approx 2.4$, but the stationary spectrum exponent is $\beta \approx 4$. No $\beta \approx 3$ regime is observed (dashed line). b: This shows the isotropic spectrum of zonal component of the wind at 200, 300, 400, … 1000 mb from the ECMWF interim reanalysis for Jan. 2006 between ±45° latitude. The straight lines are *not* regressions, rather they have the slopes of the horizontal wind in the vertical direction as estimated by drop sondes in Lovejoy et al. (2007). It can be seen that the isobaric velocity spectra have exponents close to the vertical values (especially at the data rich lower levels). Reproduced from (Lovejoy et al., 2010). The scaling starts at $k = 2$–3 corresponding $n = 4$–6 in Fig. 4a. c: An intercomparison of the GASP and MOZAIC spectra from commercial aircraft flying on isobars, adapted from (Skamarock, 2004), reproduced from (Lovejoy et al., 2010). The red lines show the behaviour predicted if the atmosphere has a perfect $k^{-5/3}$ horizontal spectrum but estimated from an aircraft following roughly horizontal trajectories until about 100 km (indicated by the arrows) and then following gradually sloping trajectories (either on isobars or gradual changes in altitude due to fuel consumption). d: A schematic of the standard model updated to take into account the results of the GASP experiment. The figure is adapted from (Lilly, 1989) and schematically illustrates the “Gage–Lilly” model. Note that 2-D enstrophy cascade region spans less than on order of magnitude in scale whereas the speculative inverse energy flux cascade (dashed line) spans over two orders of magnitude. e: This shows sample spectra from WRF forecasts of zonal wind averaged over the isobaric surfaces covering roughly the range 3–9 km in altitude, adapted from (Skamarock, 2004) who claimed a “clear k^{-3} regime” for the solid (oceanic) spectrum which spans a range of only a factor 2–3 at the relatively unreliable extreme low wavenumbers (between the arrows, upper left). Except for the extremes, the spectra again follow the isobaric predictions $k^{-2.4}$ (red) very well over most of the range. Reproduced from (Lovejoy et al., 2010). f: Same as panel d except for the new interpretation afforded by anisotropic cascades. In accord with the scaling of satellite radiances, the solar energy flux is input over a wide range of scales in a scaling manner. Also, the large scale (transition at 40–200 km) is due to a (spurious) measurement of the vertical scale spectral exponent ($\beta \approx 2.4$), shown in blue.

Please cite this article as: Lovejoy, S., Schertzer, D., Towards a new synthesis for atmospheric dynamics: Space–time cascades, Atmos. Res. (2010), doi:10.1016/j.atmosres.2010.01.004

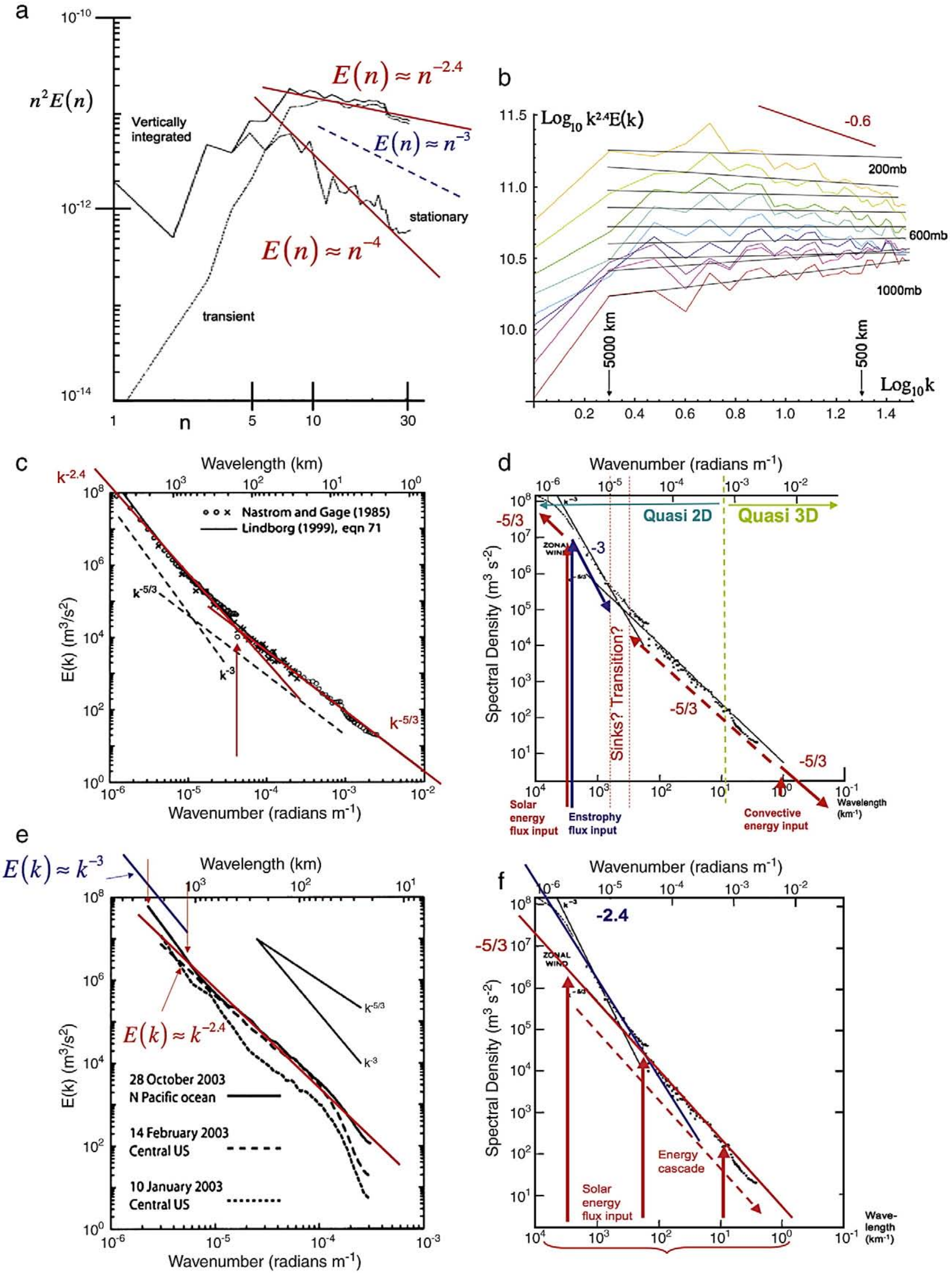

Please cite this article as: Lovejoy, S., Schertzer, D., Towards a new synthesis for atmospheric dynamics: Space–time cascades, Atmos. Res. (2010), doi:10.1016/j.atmosres.2010.01.004

where $0 \leq C_1 \leq D$ is the "codimension of the mean" (D is the dimension of the space over which the cascade is developed) and $0 \leq \alpha \leq 2$ is the "index of multifractality" characterizing the degree of multifractality: $\alpha = 0$ is the monofractal limit, $\alpha = 2$ the "lognormal" maximum. α is also the Levy index of the generator ($\Gamma = \log \varepsilon$; see Section 4.4).

So far we have described the "bare" cascade quantities, i.e. the statistical properties of a cascade developed over the finite scale ratio λ. However, it is important to realize that the small scale cascade limit ($\lambda \rightarrow \infty$) is highly singular. Indeed, from Eq. (1) we see that the second characteristic functions of Γ, i.e. $\log \langle e^{q\Gamma} \rangle = K(q) \log \lambda$ diverge; it turns out that meaningful limiting properties only exist for integrals of the cascade over finite sets (this is analogous to the Dirac δ function which is defined as a limit of functions and which is only meaningful under an integral sign). If these integrals are over sets at scale λ, then the resulting "dressed" processes (shown as the right hand column in Fig. 2b) have long probability tails such that all moments $q > q_D$ diverge i.e. $Pr(\varepsilon_\lambda > s) \approx s^{-q_D}$ for $s \gg 1$ where q_D is a critical order of divergence depending on both the statistical properties ($K(q)$) and the dimension D of the space in which the process is averaged/observed. There have indeed been many claims of such "self-organized critical" (SOC) behaviour (Bak et al., 1987) in atmospheric fields ranging from the wind, temperature and rain (Schertzer and Lovejoy, 1985b, 1987; Lovejoy and Schertzer, 1995, 2007; Tchiguirinskaia et al., 2006; Sardeshmukh and Sura, 2009); this cascade route to SOC is valid in systems with quasi stationary fluxes in contrast to "classical SOC" which is only valid in the less realistic zero-flux limit.

The cascades described above and the example in Fig. 2 are discrete in scale; they only exactly obey Eq. (1) for integer powers (n) of integer ratios: $\lambda = \lambda_0^n$. In themselves they are academic; real cascade processes are presumably continuous in scale (i.e. they respect Eq. (1) for any λ within a wide scaling range). In spite of this shortcoming, they nevertheless display all the basic features of more realistic continuous in scale (sometimes called "infinitely divisible", e.g. She and Levesque, 1994) models, in physics jargon they are called "toy models". Fig. 3a, b, c, d shows examples of more realistic continuous in scale cascades.

This paper is structured as follows. In Section 2 we give some basic theory (Section 2.1), we then discuss horizontal analyses of models (Section 2.2), remotely sensed radiances (Section 2.3), atmospheric boundary conditions (Section 2.4), aircraft measurements (Section 2.5). In Section 3 we turn our attention to the vertical, first discussing some theory of anisotropic scaling/stratification (Section 3.1), implications for aircraft measurements (Section 3.2), lidar measurements of atmospheric cross sections (Section 3.3), drop sondes (Section 3.4), and an intercomparison of the stratification of different atmospheric fields (Section 3.5). In Section 4 we consider the extension of spatial cascades to the time domain; Section 4.1 is a discussion, Section 4.2 gives some theory, Section 4.2.4 some evidence of space–time scaling from lidar, Section 4.3 from satellites and numerical models. In Section 4.4 we discuss the extension of the model to climate scales arguing that climate may be a dimensional transition (still) multiplicative process. In Section 5 we conclude.

2. Multiplicative cascades in the horizontal

2.1. Discussion

The ideal test of multiplicative cascades would be to have large quantities of dynamical wind data in both the horizontal and vertical directions, preferably on regular grids at fine resolutions — or failing that — of other high quality in situ measurements. But in situ data are often not what they seem: in situ surface measurements are typically spatially clustered over wide ranges of scale, the networks typically turn out to be geometrical fractal sets (Lovejoy et al., 1986; Korvin et al., 1990; Nicolis, 1993; Doswell and Lasher-Trapp, 1997; Mazzarella and Tranfaglia, 2000; Giordano et al., 2006) and require statistical corrections (Tessier et al., 1994). Similarly, aircraft trajectories are also fractal and require a theory of turbulence (isotropic/anisotropic) to interpret them (Lovejoy et al., 2004, 2009c) and see Section 2.5 below). Finally the state-of-the-art vertical analysis device — drop sondes — turn out to have multifractal outages and also require special analysis techniques (Lovejoy et al., 2009b) followed by statistical corrections for biases. Sophisticated data assimilation techniques such as 3D or 4D Var (e.g. Kalnay, 2003) are increasingly used to attempt to overcome these difficulties, but this at the price of introducing a number of ad hoc regularity and smoothness assumptions.

Another obstacle to testing the predictions of cascade models is that the atmosphere is "thin": its scale height is ≈10 km so for the cascades to operate over significant horizontal ranges, they must be stratified, anisotropic: we need a theory of anisotropic scaling turbulence (Section 3). It turns out that at least with regard to aircraft data the two difficulties are linked: a theory of anisotropic scaling turbulence is needed simply in order to properly interpret the data (Section 3.2).

Alternatively, we can take advantage of the fact that the different atmospheric fields are strongly nonlinearly coupled over wide ranges of scale. From a cascade perspective, this implies a model involving several interacting cascades (one for each conserved flux); this is a generalization of the classical Corrsin–Obhukov theory for passive scalar advection, (Corrsin, 1951; Obukhov, 1949) which involves nonlinear interactions between energy and passive scalar variance fluxes. Due to these couplings over wide ranges of scale, we expect fairly generally that atmospheric fields — including remotely sensed radiances — will display cascade structures. A straightforward way to progress is therefore to exploit the large quantities of remotely sensed data, we discuss this in Section 2.3; before that, we start with an analysis of the output of numerical models which are particularly easy to interpret.

2.2. Testing the predictions multiplicative cascades

2.2.1. The classical approach, conclusions from analyses and reanalyses

We have outlined a model of the atmosphere consisting of interacting cascades, each corresponding to a different scale by scale conserved turbulent flux. In order to test the model, we must have some way to determine the fluxes from the observations. The usual approach has been to use isotropic (2D, 3D) turbulence theories to decide *a priori* the appropriate flux (typically the energy or enstrophy flux) and to predict

Please cite this article as: Lovejoy, S., Schertzer, D., Towards a new synthesis for atmospheric dynamics: Space–time cascades, Atmos. Res. (2010), doi:10.1016/j.atmosres.2010.01.004

the spectral exponent of wind, temperature and other observables accordingly; the most important exponents being $\beta=5/3$ (energy flux cascades), $\beta=3$ (enstrophy or potential enstrophy cascades).

The existence of the special 2-D exponent $\beta=3$ — and the long absence of a credible alternative theory with $\beta>5/3$ — tempted even early investigators to "shoe-horn" their spectra into the k^{-3} mold. For example, by "eyeballing" four spectra over less an octave in scale, (Julian et al., 1970) already concluded that $2.7<\beta<3.1$ for the horizontal wind. When in the 1980's larger data sets became available it was possible to make more direct tests of 2D turbulence theory from atmospheric analyses (Boer and Shepherd, 1983) and later the same methodology was applied to the ECMWF ERA 40 reanalyses (Strauss and Ditlevsen, 1999; the result of applying modern data assimilation techniques to meteorological data). While Boer and Shepherd (1983) gave cautious support to $\beta\approx3$ and to a 2D interpretation, in hindsight, with the benefit of a simple theory predicting $\beta\approx2.4$ (see below), their conclusions seem unconvincing (see Fig. 4a). Similarly, when interpreting their reanalyses, (Strauss and Ditlevsen, 1999) state that "$\beta\approx2.5$–2.6 … significantly different than the classical turbulence theory prediction of 3", but again close to the value 2.4.

Today, we can revisit wind spectra using the state-of-the-art successor to the (Strauss and Ditlevsen, 1999) ERA 40 reanalysis — the ECMWF interim reanalysis — and calculate the spectrum directly without Strauss and Ditlevsen's, complex 2D preprocessing. Fig. 4b shows the isotropic spectrum of the zonal wind at each tropospheric 100 mb level, compensated by the average $k^{-2.4}$ behaviour so as to accentuate the small deviations. Also shown in the figure are straight *reference* lines. These are *not* regressions but rather the predictions of the model presented here: the slopes are those empirically estimated in the *vertical* direction from drop sondes (Lovejoy et al., 2007). Regressions on the reanalysis spectra from $k=2$ to $k=30$ (i.e. 5000–330 km) give β differing by less than 0.05 throughout the data rich lower 4 km, rising to only 0.2 at 10 km ($\approx$200 mb). These small differences could easily be the consequence of either intermittent aircraft and/or sonde motion, see below (see Lovejoy and Schertzer, in press). A complicating factor is that new (unpublished) analyses show that there can be significant NS/EW anisotropy so that exponents can be different in the two directions, see the discussion below on Generalized Scale Invariance.

2.2.2. The classical approach, conclusions from aircraft data

The interpretation of aircraft data of horizontal wind spectra continues to play an important role in supporting the 2D/3D model. Fig. 4c conveniently summarizes and compares the two largest campaigns to date; GASP and MOZAIC; again it can be seen that any k^{-3} regime must be very narrow and that in any case, $k^{-5/3}$ behaviour at small scales followed by $k^{-2.4}$ at large scales (without any k^{-3} regime) explains the observations quite accurately. By reproducing key figures and adding appropriate reference lines, (Lovejoy et al., 2009c) show that the same $k^{-5/3}$ to $k^{-2.4}$ behaviour with similar transition scales (40–200 km) explains other aircraft wind spectra (Bacmeister et al., 1996; Gao and Meriwether, 1998), and especially the little cited but most revealing GASP long haul spectra (up to 4800 km in scale, Gage and Nastrom, 1986) which is nearly perfectly $k^{-2.4}$ with no hint of any k^{-3} regime. (Lovejoy et al., 2009c) also find similar behaviour in tropospheric Gulfstream 4 scientific aircraft spectra (Fig. 9a); more details are given in Section 2.5, including an explanation for the origin of the $\beta\approx2.4$ exponent as caused by small but nonzero aircraft slopes.

2.2.3. Continuing difficulties with the classical model and inferences from numerical simulations

We have mentioned that theorists have produced a series of complicated ad hoc conceptual models which involve a small scale 3D direct ("downscale") energy cascade, a larger scale direct enstrophy cascade and finally a very large scale indirect energy cascade; the whole system involving three distinct sources of turbulent flux (e.g. Lilly, 1983). For example, in order to accommodate the results of the GASP experiment which notably showed that $k^{-5/3}$ wind spectra extended out to scales of several hundred kilometers, the more sophisticated "Gage–Lilly" model (Fig. 4d) was developed (Lilly, 1989). This model involved many unsatisfactory ad hoc features, especially the up-scale $k^{-5/3}$ energy flux regime from roughly 1 to $\approx$200 km (dashed line in Fig. 4d) which Lilly describes as "escaped" 3D energy transformed to quasi 2D stratified turbulence. The same unsatisfactory feature was termed "squeezed 3D isotropic turbulence" by (Högström et al., 1999). Other difficulties are the unknown flux sinks in the 2-D/3-D transition region, an unknown large scale energy flux dissipation mechanism (surface drag?), and speculative energy and enstrophy flux sources at $\approx$2000 km.

In order to improve on these speculative mechanisms, efforts have been made to reproduce "realistic" k^{-3} to $k^{-5/3}$ transitions in numerical models. As mentioned earlier, this is not a trivial question because of the possibility of "three dimensionalization" of two dimensional flows discussed in (Ngan et al., 2004). For the moment, the results are equivocal. For example, some numerical weather models do not display the transition (Palmer, 2001a), while others may display it although over very small ranges e.g. the (Skamarock, 2004), WRF (regional) model spectra are in fact very close to $k^{-2.4}$, see Fig. 4e. To date, the most convincing k^{-3} to $k^{-5/3}$ transitions in numerical models have been produced using the SKYHI model on the earth simulator in Takayashi et al. (2006) and Hamilton et al. (2008). In addition, Smith 2004 shows that in at least some cases, the transition to the high wavenumber $k^{-5/3}$ spectral "bump" is an artifact due to incorrectly "tuned" hyperviscosity. But even if the hyperviscosity is not to blame, as pointed out in Lovejoy et al. (2009e) they have the poorest fit to GASP observations precisely over the range $\approx$400–3000 km which their (painstakingly crafted) $k^{-5/3}$ to k^{-3} transition is supposed to explain. In other words, this model "success" may make them *less* rather than *more* realistic![1]

2.2.4. Estimating the fluxes in the dissipation and in the scaling ranges

We have argued that even if we ignore observations of the vertical structure, of remotely sensed fields and restrict our

---

[1] *Note added in press*: a new study of the ECMWF interim reanalysis has shown that the spectra of the horizontal wind and other fields shows some north–south/east–west scaling anisotropy which further complicates the issue since it implies different exponents in the north–south and east–west directions.

Please cite this article as: Lovejoy, S., Schertzer, D., Towards a new synthesis for atmospheric dynamics: Space–time cascades, Atmos. Res. (2010), doi:10.1016/j.atmosres.2010.01.004

attention purely to observations of the horizontal wind, that the 2D/3D model remains unconvincing. Returning to the GASP (combined, short, medium, long haul) spectrum, we can replace the complex Gage–Lilley model (schematic Fig. 4d) by the much simpler wide range scaling model with spurious $k^{-2.4}$ behaviour at large scales, Fig. 4f. Below, we shall see how this (vertical) exponent is spuriously detected in the horizontal, and we will also show how — starting from (nearly) first principles with small scale observations of the solar constant and the efficiency of solar to mechanical energy conversion — that the new wide range scaling but anisotropic model can be used to predict the intensity and lifetime of planetary scale structures.

In order to circumvent the isotropy/anisotropy issue and to test the general predictions of multiplicative cascades (Eq. (1)), we must analyze the data without relying on any specific theories of turbulence; we must use an approach that does not require *a priori* assumptions about the physical nature of the relevant fluxes; nor of their scale symmetries (isotropic or otherwise), the latter will in fact turn to out to be anisotropic and hence nonclassical. If atmospheric dynamics are controlled by scale invariant turbulent cascades of various (scale by scale) conserved fluxes φ then in a scaling regime, the fluctuations $\Delta I(\Delta x)$ in an observable I (e.g. wind, temperature or radiance) over a distance Δx are related to the turbulent fluxes by a relation of the form:

$$\Delta I(\Delta x)\approx\varphi\Delta x^{H} \tag{3a}$$

(this is a generalization of the Kolmogorov law for velocity fluctuations, the latter has $H=1/3$ and $\varphi=\varepsilon^{\eta}$, $\eta=1/3$ where ε is the energy flux to smaller scales). Without knowing η or H — nor even the physical nature of the flux — we can use this to estimate the normalized (nondimensional) flux φ' at the smallest resolution (Δx) of our data:

$$\varphi' = \varphi / <\varphi> \; = \Delta I / <\Delta I> \tag{3b}$$

where "<>" indicates statistical averaging. Note that if a flux ε is a realization of a pure multiplicative cascade then the normalized η power $\varphi=\varepsilon^{\eta}$ i.e. $\varepsilon^{\eta}/\langle\varepsilon\rangle^{\eta}$ is also a pure multiplicative cascade, ($<\varphi>$ is the ensemble mean large scale, i.e. the climatological value, it is independent of scale). The fluctuation, $\Delta I(\Delta x)$ can be estimated in various ways; in 1-D a convenient method (which works for the common situation where $0\leq H\leq 1$) is to use absolute differences: $\Delta I(\Delta x)=|I(x+\Delta x)-I(x)|$ with Δx the smallest reliable resolution and where x is a horizontal coordinate, (this is sometimes called "the poor man's wavelet"; other wavelets could be used). In 2-D, convenient definitions of fluctuations are the (finite difference) Laplacian (estimated as the difference between the value at a grid point and the average of its neighbours), or the modulus of a finite difference estimate of the gradient vector. The resulting high resolution flux estimates can then be degraded (by averaging) to a lower resolution L.

Following Eq. (1), the basic prediction of multiplicative cascades applied to a turbulent flux is that the normalized moments:

$$M_q = \langle\varphi_{\lambda}^{q}\rangle / \langle\varphi_1\rangle^{q} \tag{4a}$$

obey the generic multiscaling relation:

$$M_q = \left(\frac{\lambda}{\lambda_{eff}}\right)^{K(q)}; \; \lambda = L_{earth}/L; \; \lambda_{eff} = L_{earth}/L_{eff} \tag{4b}$$

where "<>" indicates statistical (ensemble) averaging and L_{eff} is the effective outer scale of the cascade. λ is a convenient scale ratio based on the largest great circle distance on the earth: $L_{earth}=20{,}000$ km and the scale ratio λ/λ_{eff} is the overall ratio from the scale where the cascade started to the resolution scale L, it is determined empirically, although from the foregoing discussion we expect $L_{eff}\approx L_{earth}$ so that $\lambda_{eff}\approx 1$ corresponding to planetary scale cascades. Note that $<\varphi_1>=<\varphi_{\lambda}>=<\varphi>$ i.e. the first moment is independent of resolution since in that case the spatial and ensemble averaging operators commute.

Since empirical data are nearly always sampled at scales much larger than the dissipation scales, the above scaling-range based technique for estimating fluxes has widespread applicability. If instead we have dissipation range data (for example if we estimate fluxes from the outputs of numerical models at the model dissipation scale), then the basic approach still works, but the interpretation is a little different. To see this, we continue with the example of the energy flux, recalling that at the dissipation scale:

$$\varepsilon\approx\nu\,\underline{v}\cdot\nabla^{2}\underline{v} \tag{5}$$

where ν is the viscosity, $\underline{v}$ the velocity. Standard manipulations give:

$$\varepsilon\approx\nu\sum_{i,j=1}^{3}\left(\frac{\partial v_i}{\partial x_j}+\frac{\partial v_j}{\partial x_i}\right)^{2} \tag{6}$$

so that if Δx is in the dissipation range (e.g. the finest resolution of the model) then:

$$\Delta v\approx\left(\frac{\varepsilon}{\nu}\right)^{1/2}\Delta x \tag{7}$$

Since the models actually use hyper-viscosities with hyper-viscous coefficient ν^{*} and a Laplacian taken to the power h (typically $h=3$ or 4), we have:

$$\varepsilon\approx\nu^{*}\underline{v}\cdot\nabla^{2h}\underline{v} \tag{8}$$

which leads to the estimate:

$$\Delta v\approx\left(\frac{\varepsilon}{\nu^{*}}\right)^{1/2}\Delta x^{h} \tag{9}$$

In all cases, we therefore have (independent of h):

$$\varphi' = \frac{\Delta v}{\langle\Delta v\rangle} = \frac{\varepsilon^{1/2}}{\langle\varepsilon^{1/2}\rangle} \tag{10}$$

We see that this is the same as Eq. (3b), the only difference is that for the wind field, the exponent $\eta=1/2$ holds in the dissipation range rather than $\eta=1/3$ which holds in the scaling regime. If we introduce $K_{\eta}(q)$ which is the scaling exponent for

Please cite this article as: Lovejoy, S., Schertzer, D., Towards a new synthesis for atmospheric dynamics: Space–time cascades, Atmos. Res. (2010), doi:10.1016/j.atmosres.2010.01.004

the normalized η flux $\varphi' = \varphi/\langle\varphi\rangle = \varepsilon^{\eta}/\langle\varepsilon\rangle^{\eta}$, then $K_{\eta}(q) = K(q\eta) - qK(\eta)$ which for universal multifractals yields $K_{\eta}(q) = \eta^{\alpha}K(q)$ (note: $K_1(q) = K(q)$), i.e. in obvious notation:

$$C_{1,\eta} = \eta^{\alpha} C_{1,1} \tag{11a}$$

(c.f. Eq. (2)) so that comparing the dissipation estimate ($\eta = 1/2$) and the scaling range estimate ($\eta = 1/3$), we have:

$$C_{1,diss} = \left(\frac{3}{2}\right)^{\alpha} C_{1,scaling} \tag{11b}$$

Since we find (for the wind field) that $\alpha \approx 1.8$ we have $C_{1diss}/C_{1scaling} \approx 1.5^{1.8} \approx 2.07$.

The extension of this discussion to passive scalars is also relevant and shows that the interpretation of the empirically/numerically estimated fluxes in terms of classical theoretical fluxes can be nontrivial. Denoting by ρ the density of the passive scalar, and χ its variance flux, the dissipation range formula analogous to Eq. (5) is $\chi \approx \rho\kappa\nabla^2\rho$ (κ is the molecular diffusivity, assumed constant) leading to $\Delta\rho \approx (\chi/\kappa)^{1/2}\Delta x$ whereas the corresponding formula in the scaling range is $\Delta\rho \approx \chi^{1/2}\varepsilon^{-1/6}\Delta x^{1/3}$ (the Corrsin Obukhov law) which has the same dependency on χ, but which also involves the energy flux; the combined effective flux $\varphi \approx \chi^{1/2}\varepsilon^{-1/6}$ measured by the scaling method thus involves two (presumably statistically *dependent*) cascade quantities rather than just one. In summary, although both dissipation and scaling ranges can be used to test for multiplicative cascades and to quantify their variability, the relation between the two normalized fluxes is not necessarily trivial.

2.2.5. Tests on GEM, GFS numerical models and ERA40, ECMWF interim, 20th century reanalyses

We can now return to the reanalyses mentioned above; we summarize the salient points of (Stolle et al., 2009) who used three years of the ERA40 project reanalyses based on the ECMWF model (Uppala, 2005). In comparison, we refer to more limited results the most recent ECMWF reanalysis product, the ECMWF "interim" reanalysis; these are somewhat higher resolution versions of the reanalyses studied by (Strauss and

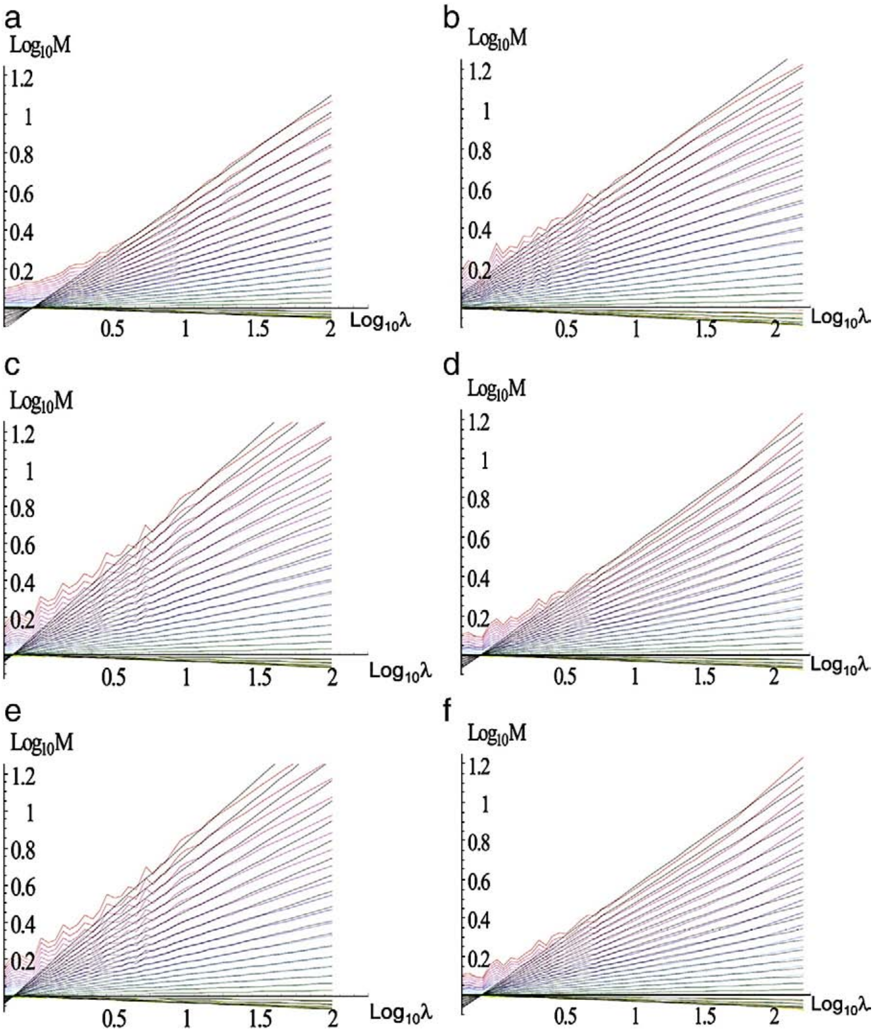

Fig. 5. Moments of fields at 1000 mb for $q = 0.$ to 2.9 in steps of 0.1. The x axis is $\log_{10}\lambda$, $\lambda = L_{earth}/L$, $L_{earth} = 20{,}000$ km. The left column is the ERA40 reanalyses, the right column is the GEM analysis ($t = 0$). The rows top to bottom are temperature, east–west wind, humidity. For the parameters, see Tables 1a, 1b. From (Stolle et al., 2009).

Please cite this article as: Lovejoy, S., Schertzer, D., Towards a new synthesis for atmospheric dynamics: Space–time cascades, Atmos. Res. (2010), doi:10.1016/j.atmosres.2010.01.004

Table 1a

Intercomparison of initial ($t=0$) fields for at 1000, 700 mb. The triplets of values are for, ERA40, GEM, GFS respectively. The aircraft estimates are from Section 2.5 and are at about 200 mb (the figure in parentheses is the Section 2.5 result, the second is corrected by the factor $(3/2)^{1.8}=2.07$ needed — at least for the wind field — to estimate the dissipation scale C_1 from the scaling range C_1, see Eq. (11)).

	C_1	α	L_{eff} (km)	δ (%)
T (1000)	0.113, 0.125, 0.142	1.94, 1.64, 1.72	21,900, 25,800, 28,000	0.31, 0.27, 0.59
T (700)	0.094, 0.077, 0.080	2.11, 1.94, 2.00	14,500, 8300, 8600	0.29, 0.47, 1.02
T (aircraft)	(0.053), 0.110	2.15	5000	0.5
U (1000)	0.105, 0.121, 0.114	1.93, 1.68, 1.80	12,900, 11,000, 12,300	0.33, 0.32, 0.54
U (700)	0.096, 0.104, 0.082	1.93, 1.86, 1.87	12,000, 11,000, 9000	0.24, 0.29, 0.83
U (aircraft)	(0.046), 0.095	2.10	25,000	0.8
h (1000)	0.121, 0.109, 0.128	2.03, 1.81, 1.86	19,800, 15,900, 21,700	0.33, 0.51, 0.46
h (700)	0.094, 0.100, 0.091	1.75, 1.60, 1.74	11,000, 11,800, 9000	0.26, 0.37, 0.46
h (aircraft)	(0.055), 0.114	2.10	10,000	0.5

Table 1b

An intercomparison of the 1000 mb fields, the triplets representing the parameter estimates for integrations of $t=0$, 48, 144 h.

	C_1	α	L_{eff} (km)	δ (%)
T (GEM)	0.125, 0.115, 0.112	1.64, 1.68, 1.69	25,700, 20,500, 25,700	0.27, 0.26, 0.80
T (GFS)	0.142, 0.138	1.72, 1.71	27,900, 26,000	0.59,0.60
U (GEM)	0.121, 0.122, 0.123	1.68, 1.62, 1.61	11,000, 11,000, 12,300	0.32, 0.36, 1.24
U (GFS)	0.114, 0.107	1.80, 1.84	12,300, 11,200	0.54, 0.64
h (GEM)	0.109, 0.106, 0.112	1.81, 1.80, 1.77	15,900, 13,800, 14,100	0.51, 0.49, 1.51
h (GFS)	0.128, 0.128	1.86, 1.81	21,700, 20,900	0.46, 0.46

Ditlevsen, 1999). We also include some results on the interesting 20th Century reanalysis (Compo et al., 2006, in preparation), which has the advantage of allowing long time behaviour to be studied (≈110 years). Recall that a reanalysis is by no means a pure empirical field, it is rather a highly elaborated "product" obtained in the ERA40 and ECMWF interim cases by using respectively sophisticated 3-D and 4-D variational data assimilation techniques, and in the 20th century reanalysis by using an ensemble Kalman filter method both of which are based on various smoothness and regularity assumptions (i.e. they don't take the strong resolution dependencies — Eq. (1) — into account, they assume that at scales smaller than one pixel $K(q)=0$).

Fig. 5a–f shows the result for the lowest level (1000 mb) horizontal wind temperature and humidity fields respectively (due to topography, the interpretation of the global 1000 mb field is not without problems; however the results at higher levels were qualitatively and quantitatively very similar, see (Stolle et al., 2009) and Tables 1a, 1b). From the existence of converging straight lines at $\lambda=\lambda_{eff}$, we see that the predictions of the cascade model are accurately obeyed (we quantify this below). This "effective outer scale" is the scale at which a pure multiplicative cascade would have to start in order to explain the observed variability over the measured range. The fact that it is of the order of the largest great circle distance 20,000 km is as expected. In some cases, $L_{eff}>20{,}000$ km ($\lambda_{eff}<1$) which simply indicates that even at 20,000 km there is a residual variability due to interactions with other fields. $L_{eff}<20{,}000$ km ($\lambda_{eff}>1$) indicates on the contrary that it takes a certain range of scales for the cascade to develop.

What is particularly striking about the figure is that not only are the outer scales near those of the planet, but in addition that power laws are accurately followed up to at least ≈5000 km so that Eq. (1) holds over nearly the full available range. This is perhaps surprising since one might have expected a larger range of scales to be required before this "asymptotic" cascade

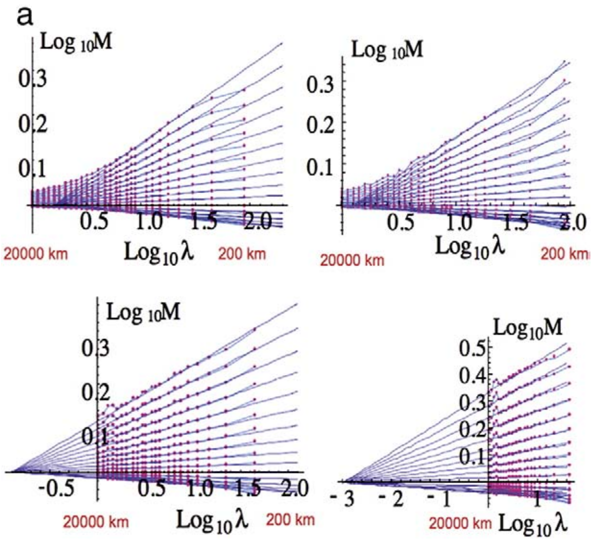

Fig. 6. a: EW analysis of 700 mb Laplacian of the zonal wind (left, top), Laplacian of the surface pressure (right, top) for every 6 h at 42° N. The bottom row shows the same fields but from the whole planet averaged over a year and then the Laplacian taken. The parameters are daily wind: $C_1=0.090$, outer scale = 12,600 km (c.f. ERA40: $C_1=0.096$, outer scale = 12,000 km), daily surface pressure: $C_1=0.10$, annual wind: $C_1=0.062$, outer scale ≈10^5 km, annual pressure: $C_1=0.054$, outer scale ≈10^7 km. b: This shows the spatial analysis of the Laplacian of the time flux of the daily 0.995 sigma level (near surface) temperature averaged over longitudes from 1891 to 2006 and for different latitude bands, from the 20th C reanalysis in the EW direction. The parameters are $C_1=((0.089, 0.095), (0.095, 0.095), (0.108, 0.143), (0.092, 0.112))$, outer scale = ((22000, 170000), (16000,32000), (34000,34000), (40000,40000)) km (all top to bottom, left to right). The mean is 0.104 ± 0.018, this is close to but lower than the 1000 mb T in Table 1a, and the outer scale is C_1 and the (geometric) mean outer scale is ≈37000 km which is slightly larger. Note that the reference scales used in the figure are 20000 cos(latitude) so that the value $\lambda=1$ corresponds to 19700, 17300, 12800 and 6800 km for 10, 30, 50, 70 degrees latitude.

Please cite this article as: Lovejoy, S., Schertzer, D., Towards a new synthesis for atmospheric dynamics: Space–time cascades, Atmos. Res. (2010), doi:10.1016/j.atmosres.2010.01.004

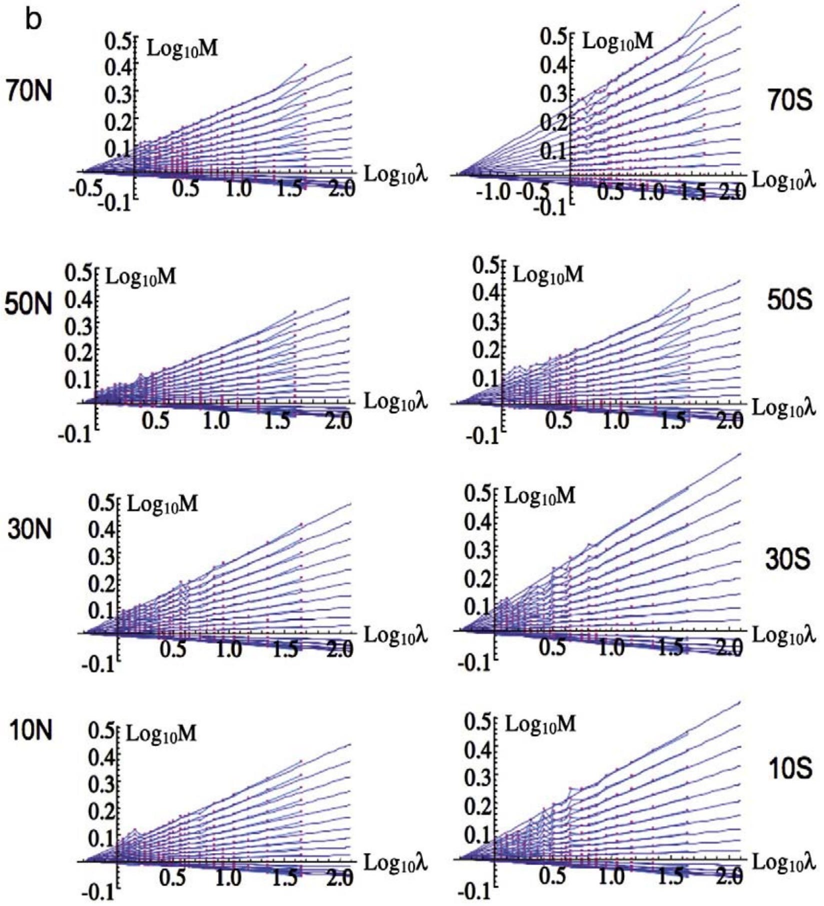

Fig. 6 (*continued*).

structure is attained at smaller scales. Similarly, Fig. 6a shows analogous spatial cascade structures in the 20th century reanalysis, here using both daily and yearly averaged pressure and wind data. In the latter case, the fluxes and hence the cascades are different corresponding to weather and climate scale processes respectively. In Fig. 6b we show the east–west cascade structures of the daily near surface (0.995 sigma level) temperatures averaged over the period 1891–2006. We see that there is some but not much latitudinal variation; we return to this in the time domain in Section 4. Before proceeding, we may already mention that for the zonal wind analyses, we used the (absolute, finite difference) Laplacian which is an estimate of the energy flux. This already indicates that the energy flux does indeed cascade throughout the available range, a point to which we return in Section 4.1.

In order to quantify the accuracy to which this cascade scaling is obeyed, we can determine the small deviations by estimating the mean absolute residuals:

$$\Delta = \overline{\left| \log_{10}\left(M_q\right) - K(q)\log_{10}\left(\lambda/\lambda_{eff}\right) \right|};\ \delta = 100 \times \left(10^{\Delta} - 1\right) \quad (12)$$

For each q, Δ is determined from the linear regression on Fig. 4b; the slopes yield $K(q)$ and λ_{eff} is determined from the intercept (fixed to be the same for all q). The overbar in Eq. (12) indicates averaging over the different λ (at intervals of $10^{0.2}$) over the available range of scales up to 5000 km and over the moments $0 \le q \le 2$ (corresponding to >90% of the data). δ is the percentage deviation; we typically find $\delta \approx \pm 0.5\%$, the details are given in Tables 1a, 1b along with estimates of the outer scales and the corresponding characterization by universal multifractals (i.e. the parameters C_1, α in Eq. (2)).

From the table, we see that very similar results were found for forecasts of a Canadian global weather model GEM (Fig. 5b, d, f) and the National Weather Service GFS model; for example the deviations are of the order ±0.3% for the reanalyses, ±0.3% for GEM and ±0.5% for GFS (Tables 1a, 1b). These small deviations allow us to conclude that the analyses and models accurately have a cascade structure. Overall, from the table we can also see that the $K(q)$ "shape parameter" — the difficult to estimate multifractal index α — is roughly constant at $\alpha = 1.8 \pm 0.1$. From Table 1a, we see that the scale by scale characterization of the intermittency near the mean (C_1) has a tendency to decrease with altitude, this effect being somewhat amplified by a decrease in the external scale (which decreases all the moments by the same factor). Interestingly, the C_1 is very similar for the different fields (it is slightly larger for the humidity), although as expected from our discussion of the difference between dissipation and scaling range flux estimates the C_1 are quite a bit larger than

Please cite this article as: Lovejoy, S., Schertzer, D., Towards a new synthesis for atmospheric dynamics: Space–time cascades, Atmos. Res. (2010), doi:10.1016/j.atmosres.2010.01.004

those measured by aircraft (Section 2.5), also shown in the table, the difference is roughly the factor of 2 estimated in Eq. (11b) for the velocity field (i.e. the dissipation versus the scaling range flux estimate).

In Table 1b, we compare the two forecast models (GEM, GFS) in order to see if there are any systematic trends as the model integrations increase (i.e. as the effects of initial conditions becomes less and less important). No systematic trends are obvious, although for the 144 hour GFS forecast, the scaling is notably poorer (although still excellent) with deviations less than about ± 1.5%. Note that because even the longest available forecast is still statistically influenced by the analyses, these results do not (quite) establish that the long time behaviour of the model is cascade-like. Below, we examine the cascade behaviour in the time domain.

We also show the results using the much longer 20th century reanalysis. Fig. 6a shows the EW analyses of the (finite difference Laplacian) flux from the 700 mb zonal wind and surface pressure. The top row shows the results at “weather scales”, i.e. the daily or 6 hourly fields with outer scales and C_1's close to those for ERA 40 (Table 1a). the bottom row shows the result for the climate resolution fields obtained from the annually averaged fields. The C_1 parameters are not too different, but the outer scales are much larger corresponding to very long climate scales (see the corresponding Figs. 19b, 20a). Finally, we can exploit the long 20th century reanalyses to obtain good statistics at single latitude bands and hence study the latitudinal dependence of the cascades; see Fig. 6b for the near surface temperature (0.995 sigma level). Although there is some variation in both C_1 and the outer scale, they are surprisingly small.

2.3. The cascade structure of radiances

2.3.1. Ground and space radar measurements of rain

An early empirical test of multiplicative cascade models was made on radar reflectivities of rain (Fig. 7a, (Schertzer and Lovejoy, 1987)). This analysis extended over the range 1–128 km which is roughly the widest range possible for a single ground based radar. From the linearity of log M_q versus log λ shown in the figure, we see that it gives strong support for the multiplicative cascade idea. The radar reflectivity factor is proportional to the sum of the squares of the drop volumes so that it is nontrivially related to the rain rate (which is proportional to the sum over the drops of the products of the volumes with the vertical fall speeds). However — at least above a minimum detectable threshold — the radar reflectivity is an accurately measured atmospheric signal and is strongly coupled with the rain rate so that the cascade structure of the reflectivities is strong evidence in favour of the cascade hypothesis for rain and the other fields.

In Fig. 7a we see that the regressions over the observed scales apparently cross at about $\log_{10}\lambda = -0.2$ corresponding to a scale 32,000 km. We can extend the ground based radar range of 128 km by using ground measurements of rain rates from rain gauges; Fig. 7b shows the result using 29 years of NOAA's Climate Prediction Center hourly US precipitation data, gridded and smoothed (Higgins et al., 2000) (the number of data points used in the figure are $21 \times 13 \times 254{,}040$: (east–west) × (north–south) × (time). We return to a temporal analysis of this data in Section 4). We see that the CPC precipitation (here, rainrate) data also has a clear cascade structure in the EW and NS directions, and that the extrapolated outer scale is nearly the same as for the ground based radar reflectivities in Fig. 7a.

In order to achieve even larger scale estimates, networks of ground based radar can be used to obtain continental scale reflectivities. However, the resulting mozaics involve large numbers of partially overlapping radars giving coverage which is far from uniform. In order to directly verify the cascade behaviour up to planetary scales, it is therefore better to use satellite data. Fig. 7c shows the result using the first orbiting weather radar, the precipitation radar (PR) instrument on the Tropical Rainfall Measuring and Mission (TRMM) satellite (Lovejoy et al., 2008a). From the figure we see that again, the scaling (log–log linearity) is excellent, the main exception being for the low q values. Adopting the convention that any number $x^0 = 1$ if $x \neq 0$ and $x^0 = 0$ if $x = 0$, we find that the $q = 0$ curve corresponds to the scaling of the raining areas. However the PR instrument has a very high minimum detectable signal: it is double the mean value and such thresholding breaks the scaling. In Lovejoy et al. (2008a) with the help of numerical multifractal simulations this scale breaking (curved lines for low q) was reproduced as a simple threshold effect. If we use a standard power law Z–R relation: $Z = aR^b$ and assume the statistics follow the universal multifractal form, then Eq. (11a) shows that $b^{\alpha} = C_{1Z}/C_{1R} = 0.63/0.50 = 1.26$. Taking the (spatial) $\alpha = 1.5$ (an estimate sensitive to low and zero rain rates, hence to be taken with caution), then we find $b \approx 1.2$ which is a little lower than the usually cited $b \approx 1.4$ for TRMM reflectivities, we return to this question when considering the corresponding temporal cascades.

2.3.2. Long and short wave radiances, passive microwaves: the scaling of the earth's energy budget

By estimating the Laplacian of the horizontal wind at the model and reanalysis dissipation scales, we have already given evidence that the energy flux does indeed cascade over the entire available range of scales. By using satellite radiance data, we will now show that the corresponding energy forcings and sinks (i.e. the short and long wave radiances) are also scaling with corresponding cascade structures — including cascade parameters and outer scales. To do this, we again used the TRMM satellite which in addition to the Precipitation Radar instrument had a visible and infra red (VIRS; 5 wavelengths) instrument as well as a passive microwave (TMI; 5 wavelengths) instrument. These were analyzed in Lovejoy et al., 2009a, the corresponding analyses for the key energy containing short wave (visible) and long wave (thermal IR) wavelengths are shown in Fig. 7d, e. We see once again excellent scaling to within about the same degree of accuracy but with somewhat smaller outer scales; Tables 2a and 2b show the details and comparison with a much more limited earlier study (Lovejoy et al., 2001). These results are bolstered by those from thermal infra red data from the geostationary satellite MTSAT (Fig. 7f, (J. Pinel, in preparation)). Sections from 30°S to 40°N, and over a range of about 13,000 km in the east–west over the Pacific ocean were used; every hour for two months (1440 images in all). It is interesting to note that the MTSAT analyses were carried out in both east–west and north–south directions, Fig. 7f is the

Please cite this article as: Lovejoy, S., Schertzer, D., Towards a new synthesis for atmospheric dynamics: Space–time cascades, Atmos. Res. (2010), doi:10.1016/j.atmosres.2010.01.004

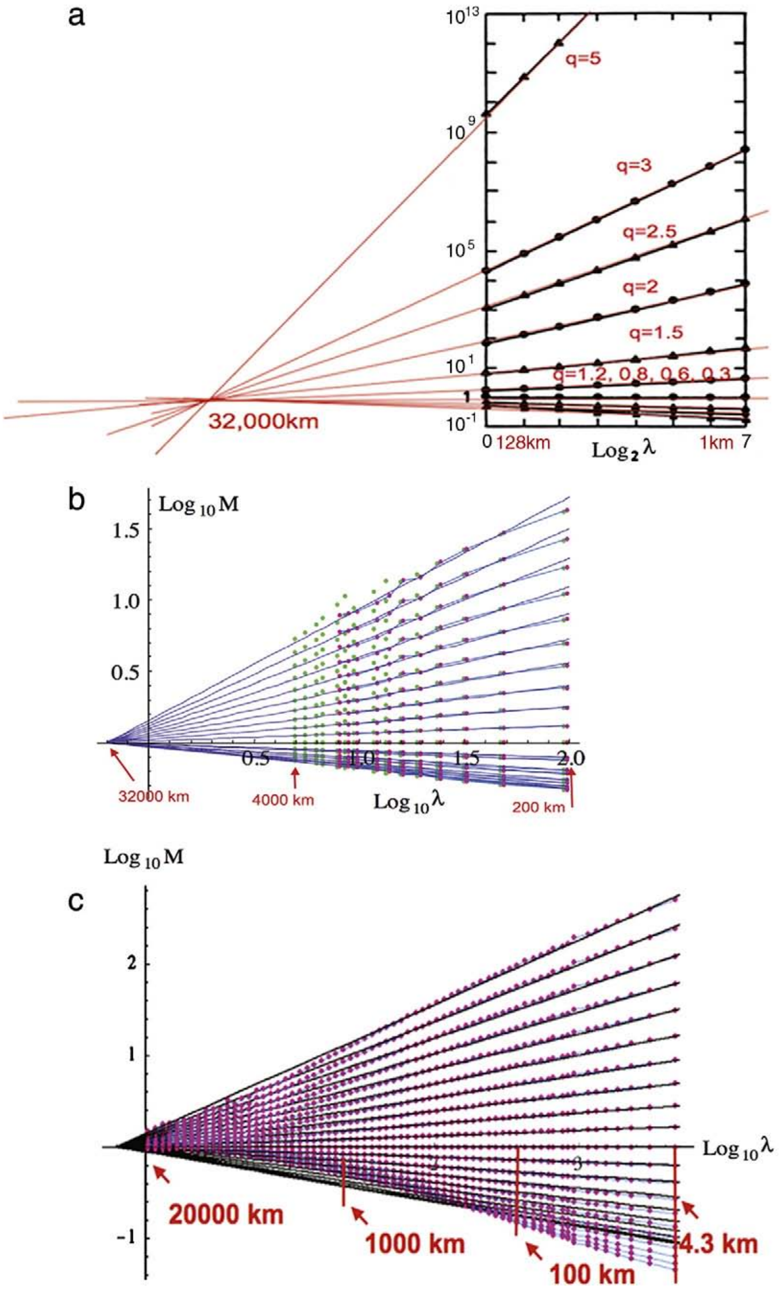

Fig. 7. a: The moments M_q of the normalized radar reflectivity for 70 constant altitude radar maps at 3 km altitude from the McGill weather radar (10 cm wavelength, 1 km pulse length for the q values indicated). The basic figure was adapted from Schertzer and Lovejoy (1987) in Lovejoy et al. (2008a) who added the straight lines converging to an outer scale at 32,000 km. b: Analysis of the CPC hourly gridded precipitation (rainrate) product for the years 1948–1976. The data were detrended annually and daily, there were 21 × 13 series, each 254,040 points long. Stations were gridded using a modified Cressman Scheme into 2° × 2.5° boxes that extended over the region long: −122.5° to −72.5° (every 2.5°), lat: 30° to 54° (every 2°). Green points are for the EW analysis, pink are from the NS analysis of temporal flux estimates. The parameters were $C_{1NS} = 0.51$, outer scale = 32,000 km, $C_{1EW} = 0.49$, the outer scale = 32,000 km. The curves are for moments of order $q = 0.0, 0.1, 0.2, ...1.9, 2.0$. c: The same as panel a except for the TRMM reflectivities (4.3 km resolution, 1100 orbits). The moments are for $q = 0, 0.1, 0.2, \ldots 2$, from (Lovejoy et al., 2008a). The poor scaling for the low q values can be explained as artifacts of the fairly high minimum detectable signal. $L_{ref} = 20{,}000$ km so that $\lambda = 1$ corresponds to 20,000 km, the lines cross at the effective outer scale ≈ 32,000 km, $C_1 \approx 0.63$. d: TRMM visible data (0.63 mm) from the VIRS instrument, channel 1 with fluxes estimated at 8.8 km. Only the well — lit 15,000 km orbit sections were used. $L_{ref} = 20{,}000$ km so that $\lambda = 1$ corresponds to 20,000 km, the lines cross at the effective outer scale ≈ 9800 km (reproduced from Lovejoy et al., 2009a). e: Same as Fig. 7d except for VIRS thermal IR (channel 5, 12.0 μm), external scale 15,800 km (see Table 2a for details, reproduced from Lovejoy et al., 2009a). f: M_q versus $\log_{10}\lambda$ for 2 months (1440 images, 1 hour resolution in time) of MTSAT, thermal IR, 30 km resolution over the region 40° N to 30° S, 130° east–west over the western Pacific, the average of east–west and north–south analyses. $L_{ref} = 20{,}000$ km so that $\lambda = 1$ corresponds to 20,000 km, the lines cross at the effective outer scale ≈ 32,000 km (from Pinel et al., in preparation) and $C_1 \approx 0.074$ (close to the TRMM thermal IR results, Table 2a, VIRS 4, 5).

Please cite this article as: Lovejoy, S., Schertzer, D., Towards a new synthesis for atmospheric dynamics: Space–time cascades, Atmos. Res. (2010), doi:10.1016/j.atmosres.2010.01.004

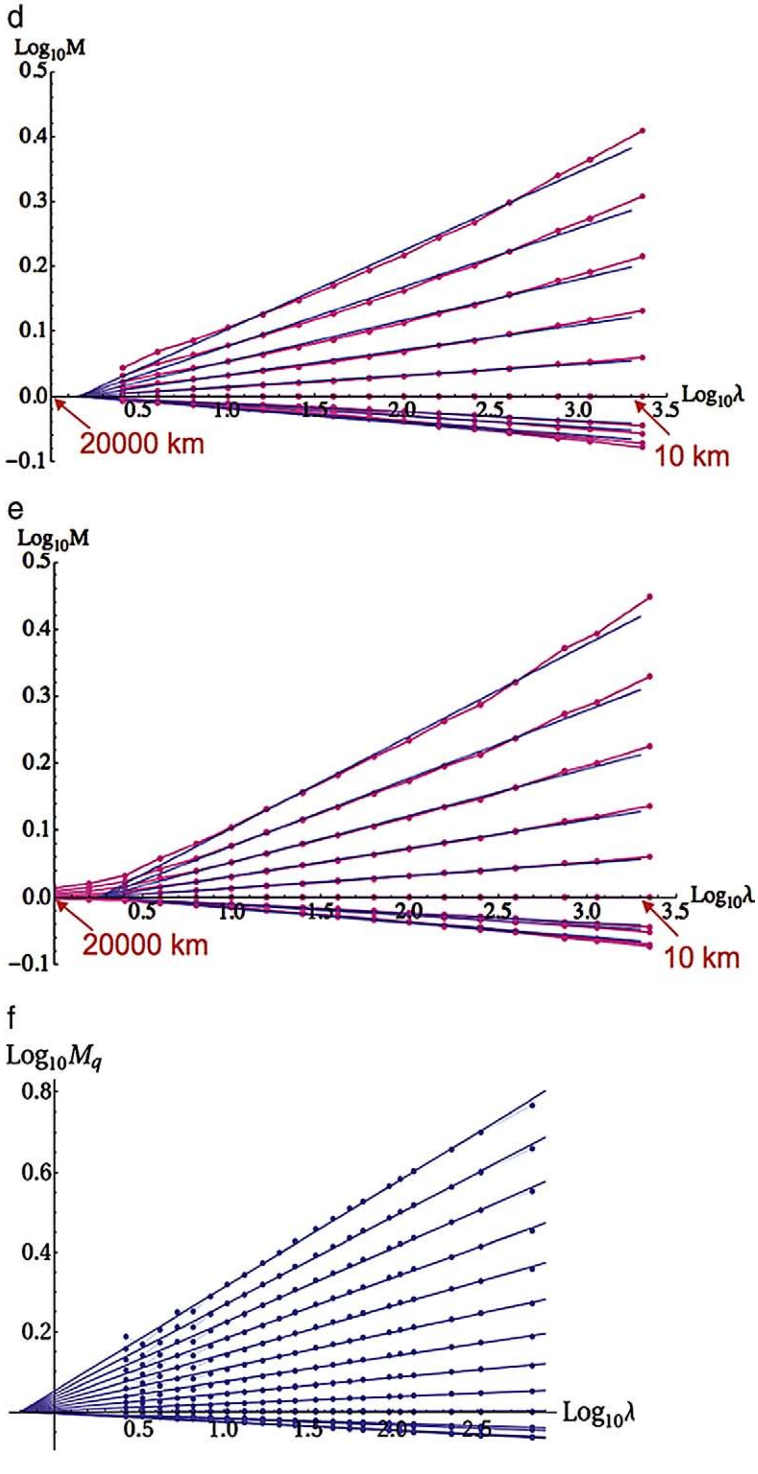

Fig. 7 (*continued*).

mean, presumably closer to the TRMM analyses which were made along the satellite track, typically oriented *N–E* or *S–W*. In Fig. 18a we show the *E–W* MTSAT analysis (compared with the temporal analysis of the same data) showing that the scaling is not so good at larger scales — but that the NS statistics almost exactly compensate leading to the excellent scaling in Fig. 7f. The scaling behaviour of these radiances is consistent with the large scale cascade structure of the wind and temperature fields. This is because while the corresponding ranges are clearly not the source and sink free regimes postulated for a turbulent inertial range, these cascades imply that the energy sources and sinks are

Table 2a
This shows the characteristics of the five visible and infra red channels (VIRS instrument, TRMM and two AVHRR channels). The H estimates are based on structure functions. The mean residues (δ, Eq. (12)) are given both with respect to the restrictive hypothesis that the cascades are universal multifractals (i.e. they respect the cascade Eq. (4) with the universal form for $K(q)$, Eq. (2) with $\alpha = 1.5$, $C_1 = 0.08$), and for the less restrictive hypothesis, that they only respect Eq. (4).

Channel	Wavelength (μm)	Resolution (km)	δ (%) line [b]	δ (%) uni [c]	α	C_1	H	L_{eff} (km)
VIRS 1	0.630	8.8	0.60	0.71	1.35	0.077	0.19	9800
VIRS 2	1.60	8.8	0.83	1.37	1.41	0.079	0.21	5000
VIRS 3	3.75	22.	1.10	1.58	1.99	0.065	0.27	17,800
VIRS 4	10.8	8.8	0.48	0.53	1.56	0.081	0.26	12,600
VIRS 5	12.0	8.8	0.47	0.81	1.63	0.084	0.33	15,800
AVHRR 14 vis [a]	0.58–0.68	2.2			1.92	0.075	0.32	18,700
AVHRR 14 IR [a]	11.5–12.5	2.2			1.91	0.079	0.36	25,200

[a] These were from 153 visible, 214 IR scenes each 280 × 280 km over Oklahoma, from Lovejoy et al.(2001) and Lovejoy and Schertzer (2006).
[b] This is the residual with respect to pure power law scaling.
[c] This is the residual with respect to universal multifractal scaling with $\alpha = 1.5$, $C_1 = 0.08$, only the outer scale is fit to each channel.

themselves scaling so that the basic assumptions of the cascade model are still apparently satisfied. In addition, the radiances and cloud fields are strongly nonlinearly coupled so that the scaling of the radiances is in itself strong evidence for the scaling of the clouds and hence presumably of the dynamics. In this regard the statistical physics problem of the interactions of radiation and scaling cloud fields is pertinent see e.g. Lovejoy et al. (1990), Davis et al. (1993), Borde and Isaka (1996), Naud et al. (1996), Schertzer et al. (1998), Lovejoy et al. (2009d), Watson et al. (2009).

2.4. Atmospheric boundary conditions: the topography

Physically, the TRMM reflectivity signal comes purely from the atmosphere whereas the visible and infra red radiances depend on the states of both the atmosphere and the surface. Just as various surface features affect the radiances, so they also directly affect the atmosphere; they are important lower boundary conditions. Another important atmospheric boundary condition is the topography; if it had a strong characteristic scale then it could impose this on the atmospheric fields and break the scaling. Fig. 8a shows the spectral analysis of the largest statistical study of the topography to date showing that it has accurate spectral scaling (roughly $E(k) \approx k^{-2.1}$) over a range of roughly 10^5 in scale. This is the latest update of the original $\approx k^{-2}$ spectrum first proposed by (Venig-Meinesz, 1951), itself updated repeatedly over the last 50 years (Balmino et al., 1973; Bell, 1975; Fox and Hayes, 1985; Gibert and Courtillot, 1987; Balmino, 1993; Lavallée et al., 1993). Note that a pure multiplicative cascade has a spectrum $E(k) \approx k^{-\beta}$ with $\beta = 1 - K(2)$; this is because spectra are Fourier transforms of the autocorrelation function which is a second order ($q = 2$) moment. For observables related to the fluxes by Eq. (3a) the extra Δx^H corresponds to k^{-H} filtering so that $\beta = 1 - K(2) + 2H$.

Fig. 8b shows the cascade structure of the topographic gradients obtained by combining four different data sets spanning the range 20,000 km down to sub-metric scales. The cascade structure holds quite well until around 40 m. (Gagnon et al., 2006) argues that this break is due to the presence of trees (for the high resolution data set used over Germany, 40 m is roughly the horizontal scale at which typical vertical fluctuations in the topography are of the order of the height of a tree). Over the range of planetary scales down to ≈40 m, it was estimated that the mean residue of the universal scaling form with parameters $C_1 = 0.12$, $\alpha = 1.79$ (for all moments $q \le 2$) was ±45% over this range of nearly 10^5 in scale (this error estimate was for the "reduced" moments $<\varphi^q>^{(1/q)}$, i.e. the definition is a little different from Eq. (12) here, so the values are not directly comparable).

2.5. Aircraft measurements of wind, temperature, humidity, pressure and potential temperature

2.5.1. The biases in the wind statistics

We mentioned that aircraft do not fly on perfectly flat trajectories, that over significant ranges of scale, their trajectories are typically fractal; this opens the possibility that their vertical fluctuations might significantly influence their measurements. This has been confirmed on both stratospheric flights at roughly constant Mach number (Lovejoy et al., 2004) and in tropospheric flights at roughly constant pressure levels (Lovejoy et al., 2009c). The latter results are particularly pertinent since all the published tropospheric turbulence campaigns have used data from roughly isobaric flights (or flights with other sources

Table 2b
This shows the characteristics of the five TMI channels and the PR reflectivity from Lovejoy et al, (2009a). All used vertical polarization. The H estimates are based on structure functions.

Channel	Wave-length	Resolution (km)	δ (%) line [a]	δ (%) uni [b]	α	C_1	H	L_{eff} (km)
TMI1	3.0 cm (10.6 GHz)	111.4	1.40	1.55	1.35	0.255	0.50	15,900
TMI 3	1.58 cm (19.35 GHz)	55.6	1.71	1.93	1.76	0.193	0.331	6900
TMI 5	1.43 cm (22.24 GHz)	27.8	1.62	1.82	1.93	0.157	0.453	5000
TMI 6	8.1 mm (37 GHz)	27.8	1.73	1.95	1.76	0.15	0.377	4400
TMI 8	3.51 mm (85.5 GHz)	13.9	1.40	1.70	1.90	0.102	0.238	6300
TRMM Z	2.2 cm (13.2 GHz)	4.3	6.0*	4.6*	1.50	0.63	0.00	32,000

[a] This is the residual with respect to pure power law scaling.
[b] This is the residual with respect to universal multifractal scaling with $\alpha = 1.5$, $C_1 = 0.08$, only the outer scale is fit to each channel.

Please cite this article as: Lovejoy, S., Schertzer, D., Towards a new synthesis for atmospheric dynamics: Space–time cascades, Atmos. Res. (2010), doi:10.1016/j.atmosres.2010.01.004

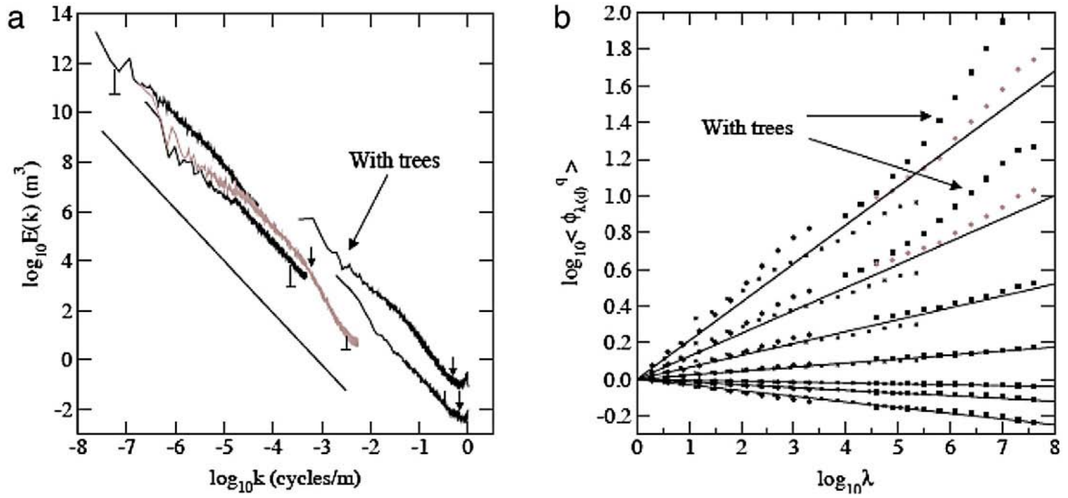

Fig. 8. a: A log–log plot of the spectral power as a function of wavenumber for four Digital Elevation Models. From right to left Lower Saxony (with trees, top), without trees (bottom), continental US (in grey, at 90m resolution), GTOPO30 and ETOPO5 (lower and upper left hand black curves). A reference line of slope −2.10 is shown for comparison. The small arrows show the frequency at which the spectra are not well estimated due to their limited dynamical range (for this and scale dependent corrections, see Gagnon et al., 2006). b: Log/log plot of the normalized moments M_q versus the scale ratio $\lambda = L_{ref}/l$ (with $L_{ref} = 20{,}000$ km) for the three DEMs (circles correspond to ETOPO5, X's to U.S. and squares to Lower Saxony). The solid lines are there to distinguish between each value of q (from top to bottom, $q = 2.18$, 1.77, 1.44, 1.17, 0.04, 0.12 and 0.51). The trace moments of the Lower Saxony DEM with trees for $q = 1.77$ and $q = 2.18$ are on the graph (indicated by arrows). The theoretical lines are computed with the global $K(q)$ function. Figure reproduced from Gagnon et al. (2006).

of small vertical drift caused by fuel consumption or other factors). This paper provides a detailed analysis based on 24 flight segments ("legs") of the Gulfstream 4 (NOAA) aircraft each 1120 km long at 1 s (≈280 m) resolution (this experiment is described in detail in (Hovde et al., 2009); it involved 10 aircraft flights over a roughly 2 week period over the northern Pacific each dropping the 20–30 drop sondes.

Fig. 9a shows the ensemble spectra for the altitude, pressure, longitudinal and transverse wind components and for the temperature and humidity. For clarity, the spectra are displaced in the vertical and in order to amplify the deviations from $k^{-5/3}$ scaling they have been normalized or "compensated" by dividing by the theoretical Kolmogorov spectrum ($k^{-5/3}$) so that flat regions thus have spectra $\approx k^{-5/3}$. In addition, in order to show the behaviour more clearly — with the exception of the lowest 10 wavenumbers — we have averaged the spectrum over logarithmically spaced bins, 10 per order of magnitude. From the figure we can make out the following features a) the altitude and pressure spectra show that there are three regimes characterizing the trajectory (roughly <3 km, 3–40 km and >40 km), b) there are two regimes characterizing the wind (roughly <40 km and >40 km) and c) a single regime for temperature and

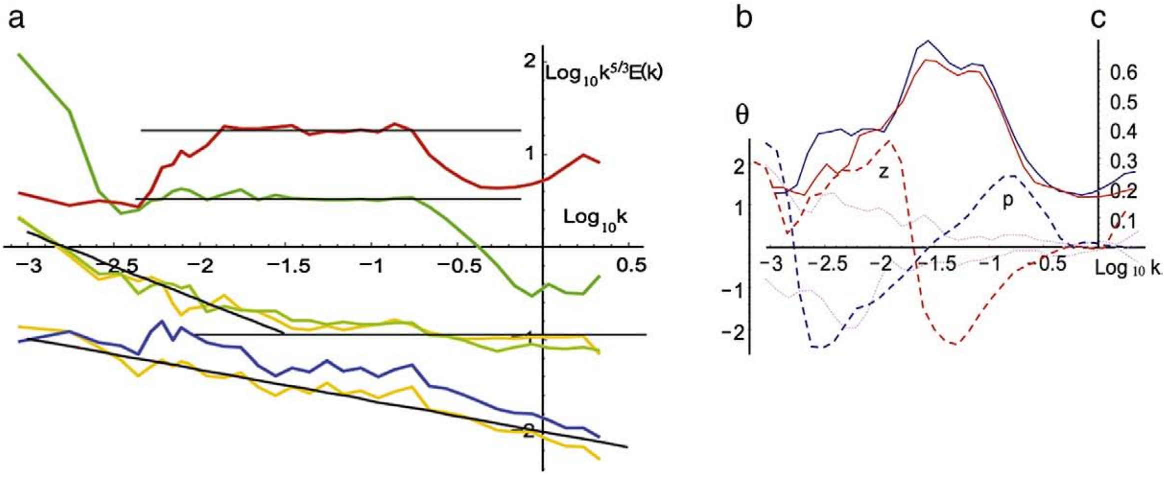

Fig. 9. a: Top bottom: this shows the compensated pressure (red), altitude (green), east–west, north south winds (middle), humidity and temperature (blue, orange, bottom). Reference slopes corresponds to $k^{-5/3}$ (flat), $k^{-2.4}$ and k^{-2}. The spectra are for 24 legs each 1120 km long, averaged over 10 per order of magnitude. Units of k: (km)$^{-1}$. Adapted from Lovejoy et al., (2009c). b: Coherencies (C, right axis) and phases (θ in radians, left axis) of the longitudinal wind with pressure (blue) and altitude (red). Solids are coherencies; those greater than ≈0.2 are statistically significant, they are highly significant over most of the range. Thick dashed lines are phases, thin purple dashed lines are the one standard deviation confidence intervals for the phases (they increase at low wavenumbers due to the smaller number of samples). A positive phase means that the wind leads (pressure or altitude), a negative phase, that it lags behind. Reproduced from Lovejoy and Schertzer (in press).

Please cite this article as: Lovejoy, S., Schertzer, D., Towards a new synthesis for atmospheric dynamics: Space–time cascades, Atmos. Res. (2010), doi:10.1016/j.atmosres.2010.01.004

humidity. Detailed leg by leg analysis shows that the exact transition point to the large scale regime varies considerably from leg to leg, 40 km being only an average. In order to understand this better, (Lovejoy et al., 2009c) considered the spectral coherencies and phase relations between the altitude and pressure wind, temperature and humidity.

Fig. 9b shows an extract of the latter results for simplicity showing only the results for the longitudinal (the along trajectory) component of the wind. We calculated the cross-spectrum which is a kind of wavenumber by wavenumber cross-correlation coefficient. However, unlike the usual cross-correlation, it is complex-valued hence it is usual to introduce the modulus — called the "coherency" (C) — and argument, the "phase" (θ; see e.g. Landahl and Mollo-Christensen, 1986). An important difference between the coherency and a cross-correlation is that C is always positive; in Fig. 9b, $C>\approx 0.2$ implies a statistically significant relation. On the other hand, a positive phase in Fig. 9b implies that the wind leads (pressure or altitude), a negative phase, that it lags behind. From the figure we see that between about 4 and 40 km, the altitude leads the wind but the pressure lags behind: the situation is reversed at larger scales (smaller wavenumbers). The direct interpretation is that for the higher wavenumbers ($(4\ \text{km})^{-1}>k>(40\ \text{km})^{-1}$, corresponding to time scales of 10–150 s) the aircraft autopilot and inertia *cause* the change in altitude with the pressure then *following* the altitude. For

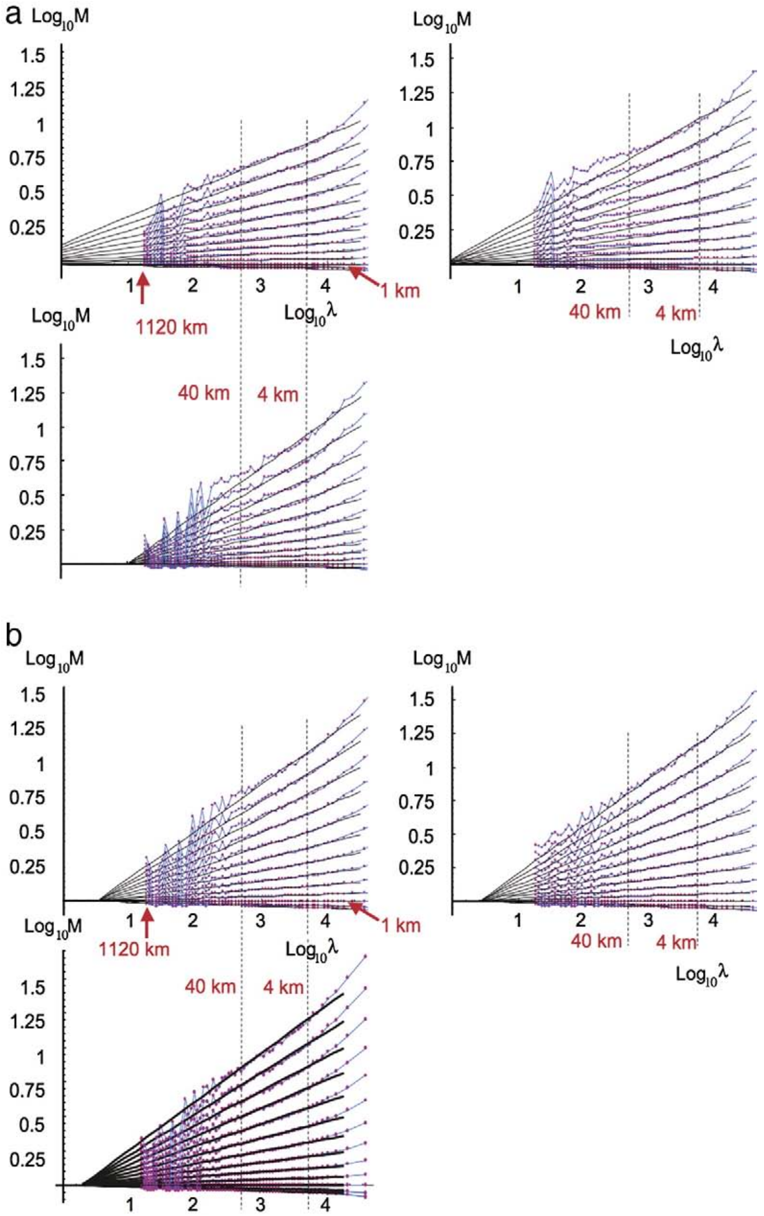

Fig. 10. a: Cascade structures for the fields strongly affected by the trajectories: the longitudinal wind (top left), the transverse wind (top right), pressure (lower left). From Lovejoy et al. (2010). b: Same as panel a but for the fields that are relatively unaffected by the trajectory: temperature (top left), relative humidity (top right), log potential temperature (lower left right). From Lovejoy et al. (2010). The reference scale is at 20,000 km, the resolution is 280m.

Please cite this article as: Lovejoy, S., Schertzer, D., Towards a new synthesis for atmospheric dynamics: Space–time cascades, Atmos. Res. (2010), doi:10.1016/j.atmosres.2010.01.004

the smaller wavenumbers ($k<(40\ \text{km})^{-1}$), the situation is reversed with the pressure changes leading (presumably *causing*) the change in wind and altitude; this is the regime where the aircraft tightly follows the isobars.

The coherency and phase analysis suggests that the main effect of the trajectory fluctuations is on the wind field and that its influence will be smaller for the other atmospheric fields. Going beyond phases and coherencies, let's consider the detailed statistics of the trajectories. For scales less than about 4 km, the aircraft inertia smoothes them out; the main variations are smooth and are associated with various roll modes and the pilot/autopilot response. However, at scales from about 4 to 40–100 km (and from ≈3 to about 300 km for the stratospheric ER-2 trajectories along isomachs), the trajectory is fractal with the altitude lagging behind the (horizontal) wind fluctuations. Finally at scales >≈40 km the aircraft follows the isobars quite closely so that the wind lags behind the pressure. These conclusions were reached by considering the average for 24 aircraft legs flying between roughly 11 and 13 km, each 1120 km long as well as through a leg by leg analysis which showed considerable variability in the scale at which these transitions occurred. According to this analysis we may anticipate that there will be a strong effect of the variability (indeed, intermittency) of the aircraft altitude on the measurements — at least for scales smaller than about 40 km where the wind leads the altitude, imposing its strong intermittency on the aircraft.

From Fig. 9a, we see that this is also the regime where the wind spectrum follows the $k^{-2.4}$ rather than $k^{-5/3}$ law; (Lovejoy et al., 2009c) argue that it is this "imposed" vertical displacement that leads to the spurious appearance of the vertical spectral exponent ≈2.4 (see the discussion of the vertical statistics in Section 3). It is significant that detailed re-examination of all the major tropospheric campaigns (GASP, Gage and Nastrom, 1986), MOZAIC, (Cho and Lindborg, 2001; Lindborg and Cho, 2001) and also (Gao and Meriwether, 1998)) display nearly identical statistics i.e. transitions from $\approx k^{-5/3}$ to $\approx k^{-2.4}$ behaviours at average scales 30–200 km. Finally, application of the anisotropic scaling model on the individual flight legs discussed in Section 3 shows that it can explain the first order structure function statistics to within ±7% over the range 0.28–500 km so that the break is indeed likely spurious.

It is interesting that the temperature and coherency/phase analysis shows that over the regime $(40\ \text{km})^{-1}<k<(3\ \text{km})^{-1}$ there are only low coherencies and small phases for both, becoming statistically insignificant for $k<(100\ \text{km})^{-1}$. The most significant — the temperature phases — indicate that there is a lag with respect to the altitude, as expected if the altitude fluctuations were imposed. The overall weak coherency between the trajectory statistics and the temperature and humidity fluctuations is thus consistent with their excellent spectral scaling $k^{-\beta}$ over the entire range (Fig. 9a).

2.5.2. Aircraft estimates of horizontal cascade parameters

From the coherency and phase analyses it is at least plausible that the aircraft can adequately determine horizontal temperature, humidity and potential temperature statistics — since these have low coherencies with the altitude and pressure — but also the transverse wind — at least over the range where the coherency is low, i.e. up to about 30–50 km. Beyond that, we expect that the aircraft will spuriously measure the vertical wind statistics; e.g. the spectrum $k^{-2.4}$ indicated in Fig. 9a.

We can now refer the reader to Fig. 10a,b which shows the flux analysis results for the longitudinal, transverse wind, pressure, temperature and humidity, potential temperature. (Lovejoy et al., 2010) analyzed this in detail concluding that as far as estimating horizontal scaling parameters is concerned, that the range 4–40 km is optimal (between the dashed lines in the figures): at smaller scales the trajectory is too turbulent while at the longer scales, one obtains isobaric rather than isoheight statistics. We nevertheless see fairly convincing cascade structure for the wind (Fig. 10a) — at least while (as in Fig. 9a) the temperature, humidity and potential temperature (Fig. 10b) show excellent scaling throughout. We could also mention that the outer scales (except for altitude) are of the order of the size of the earth although the wind is somewhat larger — the variability being presumably increased by the variability of the altitude (which is also cascade-like with outer scale of 30–50 km see (Lovejoy et al., 2010)). Table 3a and 3b compares the parameter estimates using the optimal range.

3. The vertical stratification

3.1. Discussion

The horizontal cascade structures discussed in Section 2 covered scales starting near those of the planet, hence if they are realizations of an isotropic turbulent process, it must be two dimensional. However, the same scaling regimes continue on down to scales much smaller than the scale thickness (≈10 km) — in the case of aircraft and lidar — down to ≈100–300 m which is much too small to be part of a 2-D turbulent regime. We are therefore lead to the conclusion that atmospheric scaling cannot have the same exponents in the vertical as in the horizontal. The

Table 3a

The optimum parameters at the 200 mb level (roughly the aircraft altitude, bold face) are given for the temperature, zonal wind and humidity for the analysis of the ERA40, GFS and GEM reanalysis, models (estimated from the model hyper dissipation scales up to 5000 km, taken from Table 2 of Stolle et al. (2009)). The principle value is the mean and the "±" indicates the model to model spread about the mean. For h (200 mb) the model values for L_{eff} were 10,000 (GFS), 33,000 (GEM), 50,000 (ERA40) so that the geometric mean but no spread is given. For the C_1 aircraft estimates, the second value is from Table 2, the first (in parentheses) is the same but increased by the factor 2.07 as a rough attempt to correct for the difference in the fluxes estimated in the scaling and dissipation regimes (eq. 11a).

	C_1	α	L_{eff}	δ
T **(200 mb)**	**0.075 ± 0.05**	**1.89 ± 0.04**	**10,500 ± 2000**	**0.6**
T (aircraft)	(0.107), 0.056	1.78	5000	0.5
U **(200 mb)**	**0.078 ± 0.006**	**1.88 ± 0.03**	**13,700 ± 4000**	**0.4**
U (aircraft)	(0.088), 0.040	1.94	25,000	0.8
h **(200 mb)**	**0.098 ± 0.012**	**1.66 ± 0.10**	**25,000**	**0.6**
h (aircraft)	(0.083), 0.040	1.81	10,000	0.5

Please cite this article as: Lovejoy, S., Schertzer, D., Towards a new synthesis for atmospheric dynamics: Space–time cascades, Atmos. Res. (2010), doi:10.1016/j.atmosres.2010.01.004

Table 3b
Horizontal parameter estimates. These are over the range 100 km down to 2 km except for z which is over the range 20 km to 0.5 km. Error estimates only for those which are apparently unaffected by the aircraft trajectory, they are half the difference of the parameters when estimated over the range 200 km to 20 km and those estimated from 20 km to 2 km. Note that the aircraft α estimates are a bit too big since the theoretical maximum is $\alpha = 2$. They were estimated with the double trace moment technique which depends largely on the statistics of the weaker events and these could be affected by aircraft turbulence. The H parameters were estimated from spectral exponent β and the value $K(2)$ using the equation $H = (\beta - 1 + K(2))/2$. Since the humidity is very low at the aircraft altitude, the equivalent potential temperature was extremely close to the potential temperature, hence the statistics were indistinguishable and are therefore not explicitly given in the table. The parameter values for the pressure should be taken with caution since the aircraft was attempting to follow an isobar.

	T	$\log\theta$	h	v_{long}	v_{trans}	p	z	B
H	0.50 ± 0.01	0.51 ± 0.01	0.51 ± 0.01	0.46	0.37	0.36	0.43	0.33
C_1	0.052 ± 0.012	0.052 ± 0.010	0.040 ± 0.012	0.033	0.046	0.031	0.068	0.076
α	*1.78*	1.82	1.81	2.10	2.10	2.2	2.15	1.83
L_{eff} (km)	5000	10,000	10,000	10^5	25,000	1600	50	25,000
δ (%)	0.5	2.0	0.5	0.4	0.8	0.5	2.6	0.5

schematic Fig. 11a shows the shapes of vertical sections with various degrees of scaling stratification.

Let us consider a fairly general case of anisotropic but scaling turbulence so that the fluctuations in the horizontal velocity over a horizontal lag Δx and vertical lag Δz follow:

$$\Delta v = \varphi_h \Delta x^{H_h}; \Delta v = \varphi_v \Delta z^{H_v} \tag{13}$$

where φ_h, φ_v are the turbulent fluxes dominant in the horizontal and vertical directions respectively and H_h, H_v are the corresponding exponents. The (isotropic) Kolmogorov law is recovered with $\varphi_h = \varphi_v = \varepsilon^{1/3}$, $H_h = H_v = 1/3$ where ε is the energy flux. In comparison, the 23/9 D model of anisotropic turbulence (Schertzer and Lovejoy, 1985b) in which the horizontal is dominated by the energy flux (ε, m^2 s^{-3}) and the vertical by buoyancy variance flux (ϕ m^2 s^{-5}) is obtained with $\varphi_h = \varepsilon^{1/3}$, $\varphi_v = \phi^{1/5}$, $H_h = 1/3$, $H_v = 3/5$. Similarly, the popular quasi-linear gravity wave models (Dewan, 1997; Dewan and Good, 1986; Gardner, 1994; Gardner et al., 1993) typically take $\varphi_h = \varepsilon^{1/3}$, $\varphi_v = N$ so that $H_h = 1/3$, $H_v = 1$ (N is the Brunt Väisäla

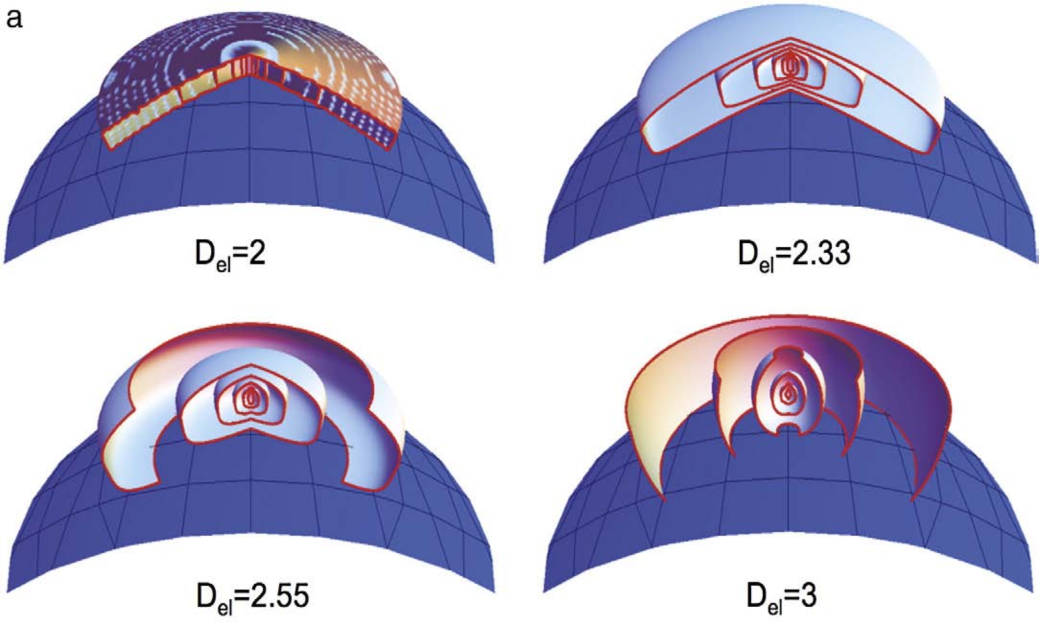

Fig. 11. a: A schematic diagramme showing the change in shape of average structures which are isotropic in the horizontal (slightly curved to indicate the earth's surface) but with scaling stratification in the vertical; H_z of increases from 0 (upper left) to 1 (lower right); $D_{el} = 2 + H_z$. In order to illustrate the change in structures with scale, the ratio of tropospheric thickness to earth radius has been increased by nearly a factor of 1000. In units of the sphero-scale (also exaggerated for clarity) here $l_s = 1/10$ the tropospheric thickness, i.e. about 10^3–10^4 times the typical value), the balls shown are ½, 1, 2, 4, 8, 16, 32 times the sphero-scale (so that the smallest is vertically oriented, the second roundish and the rest horizontally stratified). Note that in the $D_{el} = 3$ case, the cross sections are exactly circles, the small distortion is an effect of perspective due to the mapping of the structures onto the curved surface of the earth. b: A sequence "zooming" into vertical cross section of an anisotropic multifractal cloud with $H_z = 5/9$. Starting at the upper left corner, moving from left to right, from top to bottom, we progressively zoom in by factors of 1.21 (total factor ≈ 1000). Notice that while at large scales, the clouds are strongly horizontally stratified, when viewed close up they show structures in the opposite direction. The sphero-scale is equal to the vertical scale in the left most simulation on the bottom row. The multifractal parameters were $H = 1/3$, $C_1 = 0.1$, $\alpha = 1.8$ (The film version of this and other anisotropic space–time multifractal simulations can be found at: http://www.physics.mcgill.ca/~gang/multifrac/index.htm).

Please cite this article as: Lovejoy, S., Schertzer, D., Towards a new synthesis for atmospheric dynamics: Space–time cascades, Atmos. Res. (2010), doi:10.1016/j.atmosres.2010.01.004

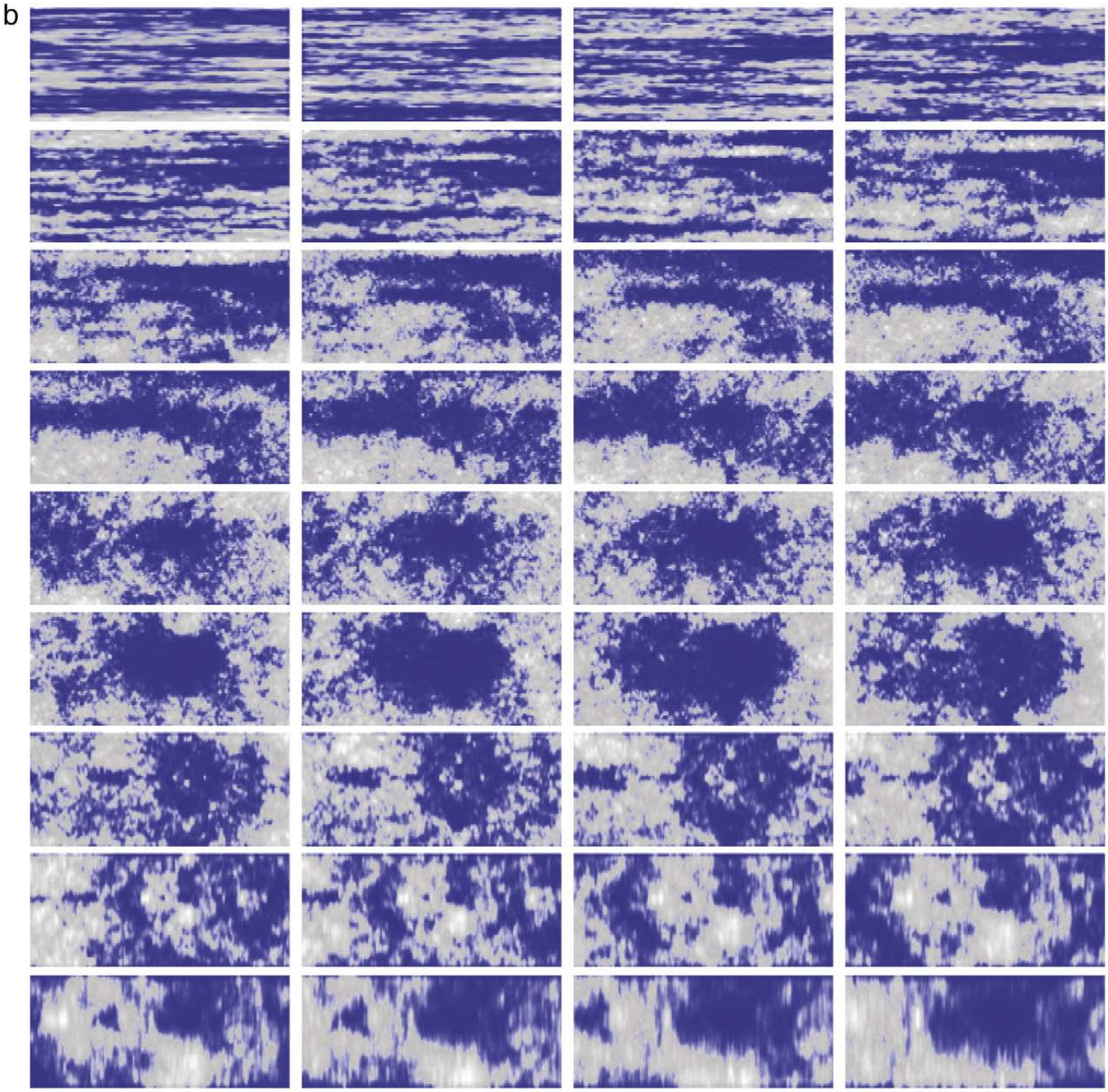

Fig. 11 (*continued*).

frequency; actually this is not a turbulent flux, a fact which is a serious weakness of that theory).

In order to write these anisotropic models in a form valid for any vector $\underline{\Delta r}=(\Delta x, \Delta y, \Delta z)$ we can use the formalism of Generalized Scale Invariance (Schertzer and Lovejoy, 1985a) and write:

$$\Delta v = \varphi_h \,||\underline{\Delta r}||^{H_h} \tag{14}$$

where the scale function (indicated by the double bars) replaces the usual vector norm appropriate for isotropic turbulence. In general, the scale function satisfies the scale equation:

$$||T_\lambda \,\underline{\Delta r}|| = \lambda^{-1}||\,\underline{\Delta r}||; \quad T_\lambda = \lambda^{-G_s} \tag{15}$$

where T_λ is the scale changing operator and G_s is its spatial generator. For the case of pure stratification in the vertical plane and assuming horizontal isotropy, we take:

$$G_s = \begin{pmatrix} 1 & 0 & 0 \\ 0 & 1 & 0 \\ 0 & 0 & H_z \end{pmatrix}; \; H_z = \frac{H_h}{H_v} \tag{16}$$

(see Section 4 for the generalization to space–time). When G_s is a matrix (corresponding to linear group generators), the notion of scale is position independent. When the generator is nonlinear, the G's are more general nonlinear operators which will depend on the coordinates; the notion of scale will be position dependent. For the case in which G is the identity matrix, we have the usual isotropic, self-similar scale changes. In the special case of "linear GSI", where G is a diagonal matrix, the system is "self affine" and we obtain stratification along a coordinate axes (e.g. Figs. 3b and 11b). Finally, when G has off-diagonal elements (Fig. 3c) we have differential rotation and stratification. The idea is that the basic dynamical symmetries determine the G's and the scale function is then determined by solving the functional scale Eq. (15) for specific boundary conditions, i.e. by specifying all the unit vectors (the "unit balls"; see below). By acting on the unit vectors in this way T_λ then generates all the other vectors, it determines the scale.

Figs. 3 and 11b provide visual illustrations of the "phenomenological fallacy" (Lovejoy and Schertzer, 2007) i.e. the confounding of morphology with mechanism. This is because GSI allows for quite striking morphologies which evolve with scale but yet are generated by the same basic scale invariant dynamic (via G). GSI concretely demonstrates that in general this identification is not warranted.

We may now define $D_s = Trace\ G_s$ as the "elliptical dimension" characterizing the spatial anisotropy. With the above dimensionally determined exponents we find $D_s = 23/9$. D_s is a dimension since changing the scales of the vectors by λ (by operating with λ^{-G}) changes their volumes by $det(\lambda^{-G}) = \lambda^{-Trace(G)}$, they are therefore exponents which quantify the change of volume with scale.

In the vertical (x, z) plane, a simple ("canonical") solution of the scale Eq. (15) is:

$$\|\Delta r\| = l_s\left(\left(\frac{\Delta x}{l_s}\right)^2 + \left(\frac{\Delta z}{l_s}\right)^{2/H_z}\right)^{1/2};\ H_z = \frac{H_h}{H_v};\ l_s = \left(\frac{\varphi_h}{\varphi_v}\right)^{1/(H_v - H_h)} \tag{17}$$

where H_z is the exponent characterizing the degree of stratification ($H_z = 1$ corresponds to isotropic 3D turbulence, $H_z = 0$ to isotropic 2-D turbulence) and l_s is the "sphero-scale" so-called because the structures are roundish at that scale; it is the unique scale defined by the fluxes φ_h, φ_v. The scale function needs only to satisfy the fairly general scale Eq. (15), so that the above "canonical" form is only the simplest scale function but is adequate for our purposes. It can be verified that if we successively take $\underline{\Delta r} = (\Delta x, 0)$ and $\underline{\Delta r} = (0, \Delta z)$ that we recover Eq. (13).

In this framework the quasi-linear gravity wave model has $H_z = 1/3$ and therefore $D_{el} = 7/3$ and we have noted that the classical 2D and 3D isotropic turbulences have $H_z = 0, 1$ hence $D_{el} = 2, 3$ respectively see Fig. 11a. The 23/9 D model of stratification was found to be obeyed quite precisely for passive scalar densities estimated by lidar (i.e. with the above scale function replacing the vector norm in the isotropic Corrsin–Obukhov law of passive scalar advection ((Lilley et al., 2004, 2008); c.f. $H_z = 0.55 \pm 0.02$). If $0 < H_z < 1$, then structures larger than the sphero-scale become progressively flatter at larger and larger scales; see the simulations in Fig. 11b.

3.2. The implications for aircraft statistics

We may now revisit the aircraft measurements analyzed above. In order to understand the effect of the vertical trajectory variability on the horizontal wind statistics, consider a large scale section roughly following a sloping isobar with slope s:

$$\Delta v = \varphi_h l_s^{H_h}\left(\left(\frac{\Delta x}{l_s}\right)^2 + \left(\frac{s\Delta x}{l_s}\right)^{2/H_z}\right)^{H_h/2} \tag{18}$$

When considering the stratospheric ER-2 trajectory, (Lovejoy et al., 2004) pointed out that in the simplest model of vertical drift where s was constant, then there would exist a critical lag $\Delta x_c = l_s s^{1/(H_z-1)}$ such that for $\Delta x > \Delta x_c$, the second term would dominate the first and we would obtain:

$$\begin{aligned} \Delta v &= \varphi_h \Delta x^{H_h};\ \Delta x << \Delta x_c \\ \Delta v &= \varphi_v s^{H_v} \Delta x^{H_v};\ \Delta x >> \Delta x_c \end{aligned} \tag{19}$$

We would therefore expect a spurious break in the horizontal scaling at Δx_c after which the aircraft would measure the vertical rather than horizontal statistics with exponent H_v rather than H_h. Since empirically, the mean l_s was roughly 0.1m, the empirical H_z was roughly 0.44 and slopes were often of the order 0.0005, so that we find that Δx_c can readily be less than 1000 km. In the spectra, this transition corresponds to a transition from $k^{-5/3}$ ($H = 1/3$) to $k^{-2.4}$ ($H \approx 0.7$); Figs. 4c, d and 9a show that this is indeed a good estimate of the small wavenumber part of the spectrum, see the discussion in Section 2.5. See (Tuck, 2008) for more discussion (and a slightly different view) of a generalized scale invariance in the atmosphere and aircraft measurements.

3.3. Direct verification of the anisotropic cascades using lidar backscatter of aerosols

3.3.1. Simultaneous horizontal and vertical analyses

The difficulty with using aircraft data to understand the nature of atmospheric stratification is that even if we overcome the aircraft measurement problems, the results must then be compared to in situ data from a different instrument in the vertical (unless perhaps we use ascent and descent aircraft legs, c.f. (Tuck et al., 2004). Clearly, the ideal way to study the vertical stratification is through remotely sensed vertical sections, hence we start our investigation of the vertical cascade structure by exploiting a unique dataset of airborne lidar backscatter. The data were taken over three afternoons in Aug. 2002 near Vancouver, British Columbia, see Fig. 12a, and the zoom, Fig. 12b for an example showing the extremely fine details, including hints that at the small scales that structures are no longer flat, but start to be stretched in the vertical (Fig. 12b; compare this with the simulation in Fig. 11b). The lidar backscatter is primarily from aerosols; Lilley et al. (2004) compared the first order horizontal and vertical structure functions, and Radkevitch et al. (2007, 2008) studied the corresponding spectra, including a new anisotropic scaling analysis technique (ASAT) involving nonlinear coordinate transformations. Lilley et al. (2008) contain a literature review and additional anisotropy analyses including of the fluxes estimated from gradients of the backscatter ratio. The conclusions were broadly that the backscatter statistics can be accurately described if the ratio of horizontal to vertical scaling exponents was $H_z \approx 0.55$. In addition, the scale at which

Please cite this article as: Lovejoy, S., Schertzer, D., Towards a new synthesis for atmospheric dynamics: Space–time cascades, Atmos. Res. (2010), doi:10.1016/j.atmosres.2010.01.004

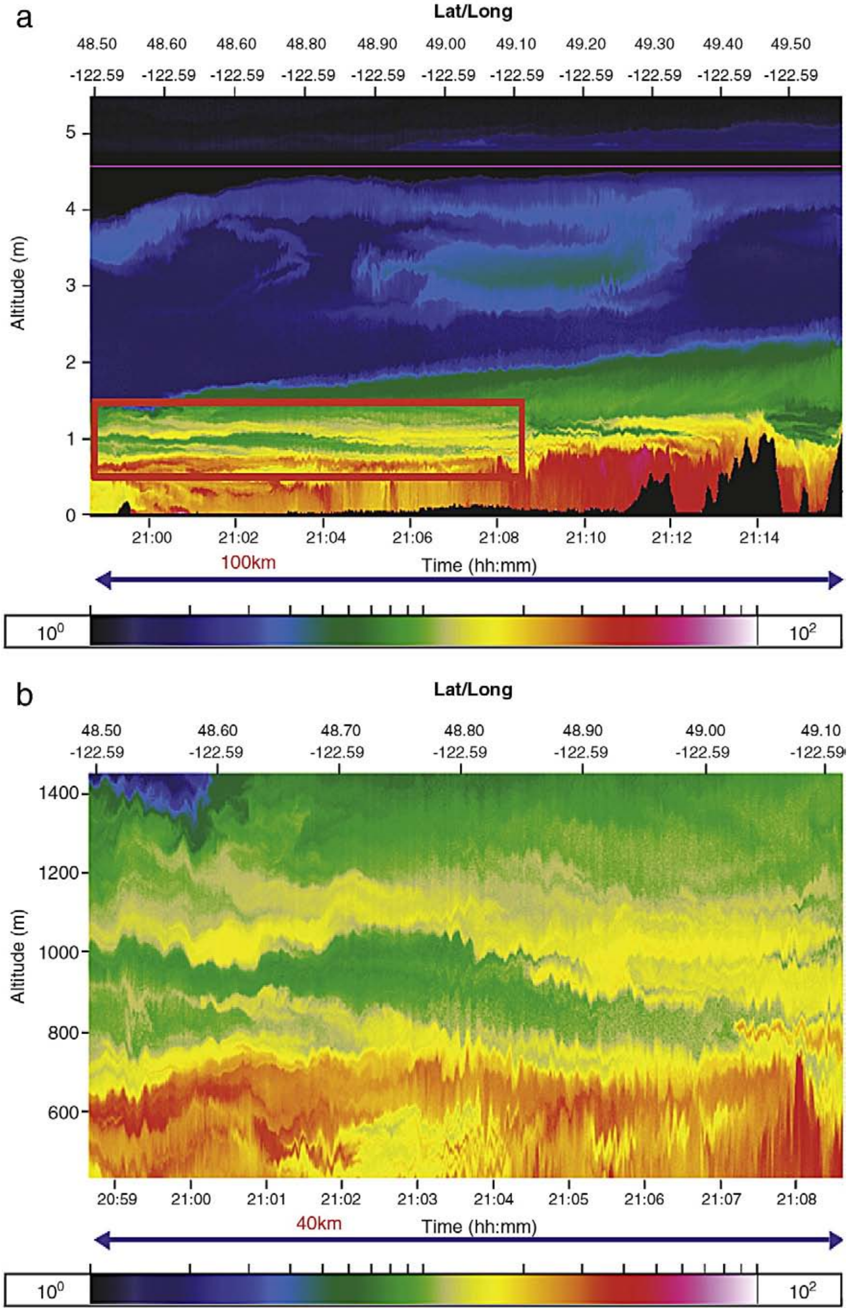

Fig. 12. a: This is a vertical cross-section of lidar backscatter on 14 August 2001. The scale on the bottom is a logarithmic color scale: darker is for smaller backscatter (aerosol density surrogate), lighter is for larger backscatter. The vertical is 4.5 km and the horizontal is 120 km. The horizontal resolution is 100 m and the vertical resolution is 3 m. The range of scales in this data set is 1200 × 1500 (horizontal × vertical). The region in the red rectangle is blown up in panel b. The black shapes along the bottom are mountains in the British Columbia region. b: A blow-up of the region within the red rectangle in *a*, it is 40 km wide and 1000 m thick. This panel highlights the high spatial resolution and the wide dynamic range. There is no saturated signal and high sensitivity to low signal return. Note that while at large scales, the structures are horizontally flat, at the smaller scales, we can begin to see structures that are more roundish, or even vertically aligned; compare with Fig. 11. This and panel a are courtesy of K. Strawbridge. For other similar examples, see Lilley et al. (2004).

horizontal and vertical fluctuations are of equal magnitude (“the sphero-scale”) was directly estimated for the first time (it varied between about 3 cm and 80 m).

A direct horizontal/vertical intercomparison of the normalized fluxes M_q is given in Fig. 13a, b. We see that the cascade structure predicted by Eq. (4) is well respected: not only are the lines quite straight, they also “point” to the effective outer scale of the process, — i.e. the scale at which a multiplicative cascade would have to start in order to account for the statistics over the observed range. We see that as before, for the horizontal analysis, L_{eff} is a little larger than the physical scales (≈25,000 km, 50 km for the horizontal and

Please cite this article as: Lovejoy, S., Schertzer, D., Towards a new synthesis for atmospheric dynamics: Space–time cascades, Atmos. Res. (2010), doi:10.1016/j.atmosres.2010.01.004

vertical respectively). Table 4 shows some of the parameters characterizing $K(q)$ and shows that they are indeed quite different for the horizontal and vertical directions.

3.3.2. The construction of space–space diagrammes from lidar data

If we define a "structure" in a field f as a fluctuation in the value of f of magnitude Δf, then we can use this to statistically define the relation between the horizontal and vertical extents of structures. For example, using the first order structure function we can equate the horizontal and vertical fluctuations: $\langle|\Delta f(\Delta x)|\rangle = \langle|\Delta f(\Delta z(\Delta x))|\rangle$ which gives an implicit relation $\Delta z(\Delta x)$ between the horizontal and vertical extents (Δx, Δz respectively). Using the scale function (Eq. (17)) and the relation 14 for the fluctuations in terms of the scale function, we see that this is equivalent to using $\|(\Delta x,0)\| = \|(0,\Delta z(\Delta x))\|$ or $\Delta z = l_s(\Delta x/l_s)^{H_z}$. The same idea is used in Section 4 on space–time cross-section data to produce classical "space–time" ("Stommel") diagrammes, so that here we use the expression "space–space" diagrammes. The existence of spatial vertical lidar cross-section data spanning many orders of magnitude in scale allows us to empirically determine this statistical correspondence directly and accurately.

Fig. 13c shows the result using 9 vertical cross-sections (using a slightly different subset of the same data that were described and analyzed in (Lilley et al., 2004)). We see that on a log–log plot the inferred $\log \Delta x - \log \Delta z$ relationship is reasonably linear and that the slope is very near the theoretical value $H_z = 5/9$ (shown by reference lines; the scaling is not as good at the larger distances where the statistics are poor). However, what is particularly striking about the figure are the implications of extrapolating the lines both to larger and to smaller scales. First, at smaller scales, we can estimate the sphero-scale (l_s is determined by the intersection of the extrapolation of the empirical line with the solid black reference line, $\Delta x = \Delta z$); we find it in the range 20 cm to 2 *m*; similar to the other estimates discussed above; it thus seems that the extrapolation is quite reasonable down to metric scales or less. However equally impressive is the extrapolation to larger scales: we see that extrapolation to the planetary scale (20,000 km) gives a corresponding vertical extent of ≈10 km i.e. the thickness of the troposphere. In other words, there is no obvious reason why the scaling stratification should have a break anywhere in the meteorologically significant range of scales. Note that there are various ways to generalize and extend the method for estimating space–space and space–time relations. For example, we could use the same method to determine the horizontal/vertical relations for weak and strong events by considering structure functions with exponents $q<1$ or $q>1$ (see an example of this method in Section 4). Alternatively, we could use the statistics of the fluxes (the normalized moments M_q) to establish the relation using $M_q(\Delta x) = M_q(\Delta z(\Delta x))$; this method is used in Section 4. Also in Section 4 we use this method to determine space–time ("Stommel") diagrammes.

3.3.3. Reconciling convection with wide range scaling

On the face it, our claims of wide range horizontal and vertical scaling fly in the face of the phenomenology of atmospheric convection which — ever since (Riehl and Malkus, 1958) — has relied on phenomenological models based on scale separations (although see Lilly, 1986a,b) for attempts to reconcile it with turbulence theory with the help of helicity). The apparent incompatibility of horizontal scaling and convection was debated by Yano (2009) and the appendix of Lovejoy et al. (2009c). In Section 1, we have already mentioned the phenomenological fallacy, i.e. the dangers of inferring mechanism from form, from phenomenology. In principle, then convective phenomenology need not contradict the observation of wide range anisotropic scaling. To make this more concrete and convincing, we need to show how to get structures traversing the troposphere in height while being only 100 km or so across (the "typical" horizontal scale cited for convection). In terms of Generalized Scale Invariance this implies vertical cross-sections being roundish in shape at around 1–10 km i.e. with "sphero-scales" being much larger than the range 0.01–1 m observed in passive scalars or in the horizontal wind.

To see if this is possible, we can appeal to orbiting radars on the Tropical Rainfall Monitoring Mission satellite (TRMM, 4.3 km resolution horizontal, 500 m in the vertical, 3.2 cm wavelength, 1997–present, see Section 2) and CloudSat (1.08 km in the horizontal, 250 m in the vertical, 3 mm wavelength, 2006–present, see Fig. 13d for an example). We have already shown in Section 2 that although the radars have problems measuring weak effective reflectivity factors (Z) that the fluxes φ estimated from Z follow the basic prediction of multiplicative cascades — Eq. (1) — over the entire range 4.3 km to 20,000 km with accuracies of ±4.6% (TRMM, 1176 orbits, near surface).

For precipitation the main limitation of the TRMM radar is its poor measurement of the weak (and zero) rain rate regions. With its much smaller wavelength (3 mm, 94 GHz), the CloudSat radar can detect signals about 10^4 times lower (down to $Z \approx 0.01\ \mathrm{mm}^6/\mathrm{m}^3$) and therefore can detect much smaller drops. Since Z is proportional to the sum of the squared drop volumes it is highly correlated with the sum of the volumes, i.e. the LWC (liquid water content) and is thus a good surrogate for convection. Also, relevant here is the study of TRMM and MTSAT short and long wave radiances (Section 2.3.2) that found that the predictions of multiplicative cascades were obeyed to within ±0.5% over the than 8.8 to 5000 km, i.e. right through the "convective scale" of 100 km (see Fig. 7e, f).

We can use the CloudSat data to determined structure functions (as in the previous subsection) and from there, determine the corresponding space–space diagrammes; Fig. 13e shows the result for fluctuations defined from orbit by orbit averages as well from an ensemble average over all the orbits. The mean of the individual orbit by orbit $\Delta x(\Delta z)$ curves and the ensemble are nearly identical; the orbit to orbit spread is shown as one standard deviation curves above and below (the curves are occasionally double valued along the Δx axis due to statistical fluctuations). In addition to the empirical curves, we have provided two theoretical reference lines with slopes $H_z = 5/9$, 1. The basic behaviour is very similar to that of the lidar backscatter (Fig. 13c). The main difference is the value of the "sphero-scale" determined by the intersection of the two lines, here about 100 m. Structures at larger scales are flat, while at smaller scales they are elongated in the vertical. Although the exponents for Z and for lidar aerosol backscatter are

Please cite this article as: Lovejoy, S., Schertzer, D., Towards a new synthesis for atmospheric dynamics: Space–time cascades, Atmos. Res. (2010), doi:10.1016/j.atmosres.2010.01.004

nearly identical (given by the theoretical anisotropic Corrsin–Obhukov values), the corresponding sphero-scales l_s are about a factor 1000 larger (although as can be seen from the error, there is a large scatter; the mean of $\log_{10} l_s$ with l_s in km is $\approx -1.6 \pm 0.9$ i.e. one standard deviation bars are 5 m to 500 m, geometric mean 50 m). Fig. 13f shows the corresponding average contours of cloud reflectivity structures showing how they very gradually tend to rounder shapes at the larger scales. It thus seems possible that the fundamental distinction between of convective as opposed to stratiform dynamics is the much larger sphero-scale in the former. In the 23/9D model, this would be the natural consequence of the variations in the buoyancy variance flux in convection (the φ_v in Eq. (17)).

3.4. Vertical cascades using drop sondes

3.4.1. Description of the data set

The lidar and satellite radar data analysed in Section 3.3 are uniformly spaced in orthogonal directions with high signal to

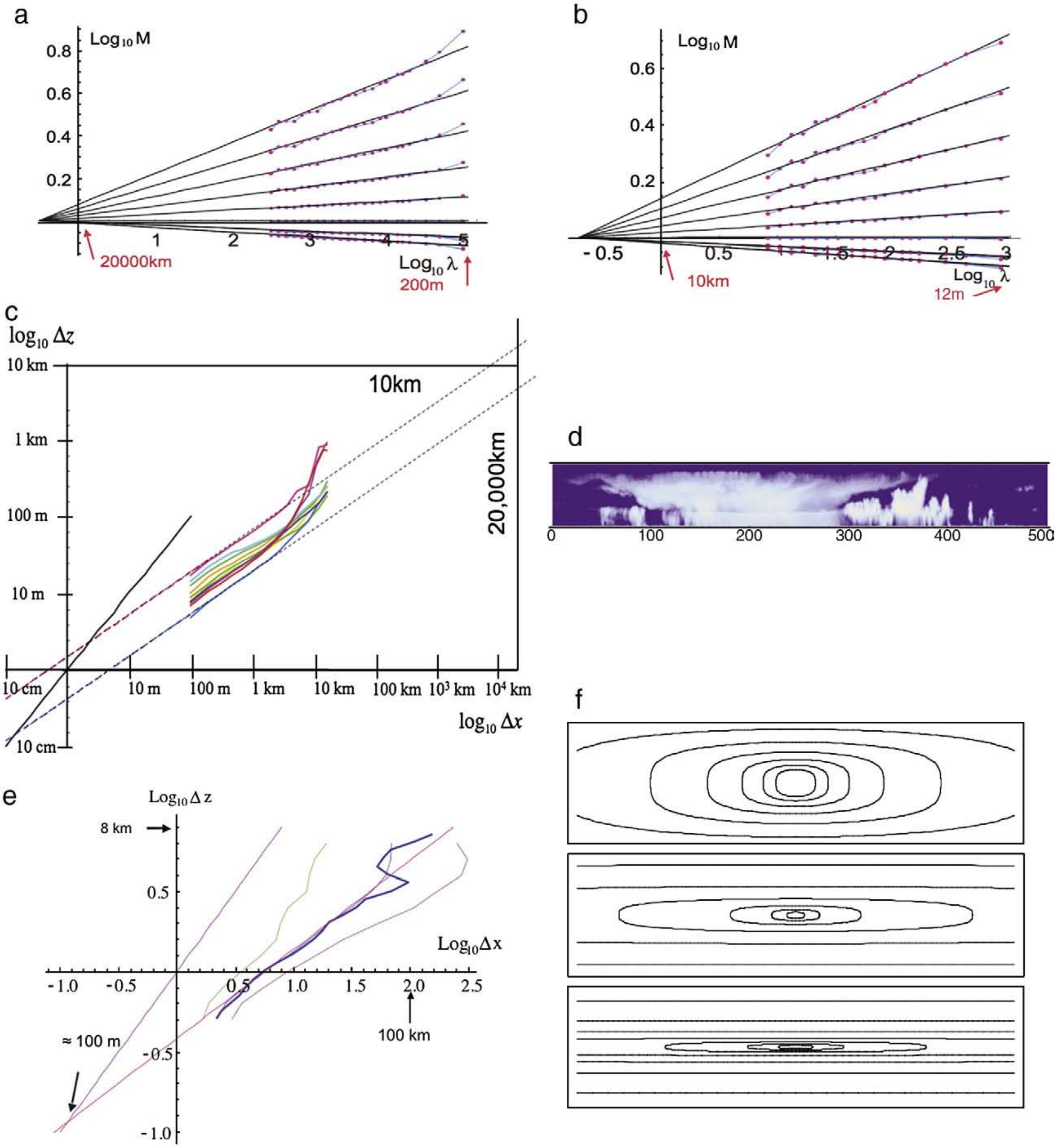

Please cite this article as: Lovejoy, S., Schertzer, D., Towards a new synthesis for atmospheric dynamics: Space–time cascades, Atmos. Res. (2010), doi:10.1016/j.atmosres.2010.01.004

Table 4
Statistics derived from backscatter ratios of 10 vertical lidar cross-sections. Table from Lovejoy et al. (2009b).

Field	Resolution (m)	$\overline{\delta}$ (%)	C_1	H	α	L_{eff} (km)
B vertical	12 m x192m	0.4	0.11	0.60	1.82	50
B horizontal	12 m x192m	0.5	0.076	0.33	1.83	25,000

noise ratios and are thus relatively straightforward to analyze. However if we seek to study the usual dynamic or thermodynamic variables, we are forced to turn to in situ measurements. Traditionally over a substantial part of the troposphere, radiosondes have been the only way to get such vertical information. However, they have numerous problems including payloads swinging into and out of the balloon's wake, low vertical resolutions (typically of the order of 100 m) and slow ascent speeds which — in areas of strong downdrafts — can even temporarily become descents. As mentioned earlier, these technical difficulties have contributed to the absence of consensus on the nature of the vertical stratification.

In the last ten years, the development of GPS drop sondes has drastically changed this situation (Hock and Franklin, 1999). Drop sondes are free of problems with swinging payloads and wakes and they have rapid descent times (less than 15 min from the top of the troposphere) and — with the help of GPS tracking — they have high vertical resolutions (of the order of 5 m, although see the discussion below). The data discussed here were part of the same Winter Storms 2004 experimental discussed in Section 2.5 using the NOAA Gulfstream 4 aircraft. During a 2-week period, ten flights each dropped 20–30 sondes, a total of 262. Of these, 237 reasonably complete sets were analyzed in Lovejoy et al. (2007, 2008c), here we consider the 220 sonde subset which started at altitudes >10 km and we summarize the findings of (Lovejoy et al., 2009b).

3.4.2. Intermittent multifractal sampling: the problem of outages

The cascade structure Eq. (1) is the consequence of variability building up scale by scale over a potentially large scale ratio λ. In order to verify Eq. (1) and to estimate $K(q)$, we attempt to invert the cascade process by systematically degrading the resolution of the fluxes by averaging. This is straightforward enough for data sampled at regular intervals, but for data with highly irregular resolutions we must take into account the variability of the resolution. The drop sonde resolution is variable for two reasons: first, even if the sampling was at the nominal 0.5 s, the variable vertical sonde fall speed would lead to variable vertical sampling intervals. This source of variability is not too large: the mean vertical sonde velocity decreases from about 18 m/s to about 9 m/s near the surface (due to increased air resistance); turbulence induced fluctuations increase this range of resolution by about another factor of 2. However, the variability problem is made much worse because of data outages — even though these affected only 9.5% of the observations. The problem is that they affected every sonde, that they were highly clustered and sometimes very large (i.e. occasionally several km in size).

By treating the measurement intervals in both the vertical and in time Lovejoy et al. (2009b) obtained a surprising result: the outages had almost exact cascade structures with rather large intermittencies ($C_{1time} \approx 0.21$, $C_{1vert} \approx 0.23$) with outer scales near the outer scale of the data ($\approx$200 s and $\approx$3 km respectively). In order to overcome this outage problem, two developments are needed. The first is a robust technique to estimate the fluxes, the second a method of statistical correction to the scaling exponents in order to correct for the strongly variable resolutions (Lovejoy et al., 2009b).

When these techniques were applied to the drop-sonde data, the moments displayed in Fig. 14a, b were obtained. The quantities that we analysed can be roughly grouped into two categories: dynamical and thermodynamical variables. The dynamic variables (Fig. 14a) were the modulus of the horizontal wind v, the pressure p, the total air density (ρ, including that due to humidity), and the sonde vertical velocity w_s. We also separately analyzed the north–south and east–west components of the horizontal wind but the results were not much different and we will not discuss them further. For the vertical sonde velocity, the fluctuations around a quadratic fit (corresponding to a constant deceleration from 18 m/s to 9 m/s) were used. Due to the parachute drag, the fluctuations in w_s depend on both the vertical and horizontal wind so that it should not be used as a surrogate for the vertical wind.

The thermodynamic variables are temperature (T), log potential temperature ($\log\theta$), log equivalent potential temperature ($\log\theta_E$) and humidity (h), see Fig. 14b. The $\log\theta$ and $\log\theta_E$ are proportional to the entropy densities of the dry and humid air respectively. In addition, their structure is important for the overall atmospheric (static) stability, for example $g d\log\theta/dz$ is the square of the Brunt–Väisälä frequency so that where the latter is negative, the

Fig. 13. a: Horizontal analysis of the moments of the normalized lidar backscatter ratio for 10 atmospheric vertical cross-sections (L_{ref} = 20,000 km corresponding to $\lambda = 1$). The curves are for the moments of order $q = 0.2, 0.4, \ldots 2$. The largest directly accessible scale is ≈100 km, and the lines converge to an effective outer scale of $L_{eff} \approx 25{,}000$ km. Reproduced from (Lovejoy et al., 2009b). b: The same cross-sections as in panel a but analyzed in the vertical direction, (L_{ref} = 10 km corresponding to $\lambda = 1$). The largest directly accessible scale is ≈3 km, the point of convergence is $L_{eff} \approx 50$ km, see Table 1a. Note that the vertical axis is not the same as for the horizontal analysis; this is a consequence of the scaling anisotropy; the exponents are roughly in a constant ratio (reproduced from Lovejoy et al., 2009b)). c: A space–space (horizontal/vertical) diagramme from 9 vertical lidar sections obtained from first order structure functions (this is from a slightly different subset of the data analysed in panels a,b). The dashed lines have theoretical slopes 5/9, the thick black line is the bisectrix ($x = y$). The sphero-scale is the intersection of the empirical lines with the bisectrix. It can be seen that the sphero-scales are somewhat variable, but mostly between 10 cm and 1 m. At the larger scales, we see that the earth size (20,000 km) roughly corresponds to the troposphere thickness (10 km). Note that the empirical statistics are not so good at the largest scales. We thank A. Radkevitch for help with this analysis. d: This is a small sample of the first of the 16 CloudSat orbits analysed in this paper (log density plot). The cross-section is 16 km high, 650 km wide (presented with a 1:4 aspect ratio). Notice the large convective cell about 15 km high, 200 km across. e: A space (horizontal)–space (vertical) diagramme estimated from the absolute reflectivity fluctuations (first order structure functions) from 16 CloudSat orbits. Reproduced from Lovejoy et al. (2009c). f: This shows the theoretical shapes of average vertical cross-sections using the CloudSat derived mean parameters from Fig. 2: $H_z = 5/9$, with sphero-scales 1 km (top), 100 m (middle), 10 m (bottom), roughly corresponding to the geometric mean and one standard deviation fluctuations. The distance from left to right is 100 km, from top to bottom is 20 km. It uses the canonical scale function (Eq. (17)). The top figure in particular shows that structures 100 km wide will be about 10 km thick whenever the sphero-scale is somewhat larger than average. Reproduced from Lovejoy et al. (2009c).

Please cite this article as: Lovejoy, S., Schertzer, D., Towards a new synthesis for atmospheric dynamics: Space–time cascades, Atmos. Res. (2010), doi:10.1016/j.atmosres.2010.01.004

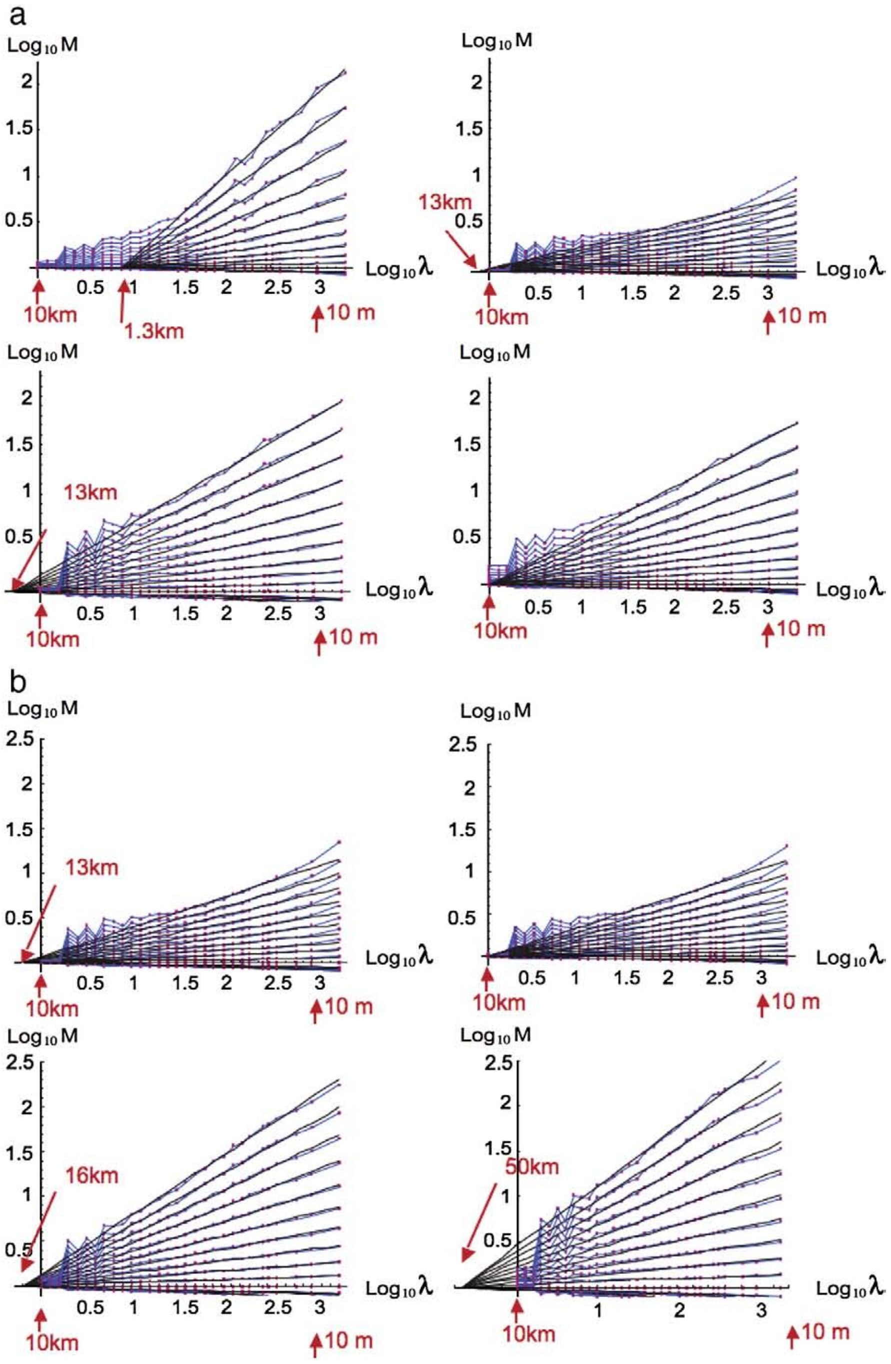

Fig. 14. a: The dynamical fields v, p, ρ, w_s (clockwise from upper left) for $q=0.2$, 0.4, ...2. Reproduced from Lovejoy et al. (2009b). b: The same as for panel a except for the thermodynamic fields T, log θ, h, log θ_E (clockwise from upper left). Reproduced from Lovejoy et al. (2009b).

atmosphere is considered conditionally unstable. Similarly, it is convectively unstable when $g\mathrm{dlog}\theta_E/\mathrm{d}z$ is negative.

From the figures we can see that with small deviations (c.f. the Table 5) all the fields have small residuals with respect to the predictions of cascade theories (Eq. (4); the residuals (Eq. (12)) were averaged over the range 1 km to 10 m).

The H exponents are from the fluctuation analyses (see Lovejoy et al., 2009b) and are the means of the fits from 30–300 m and 300–3000 m, the spread is half the difference. α was estimated to the nearest 0.05 using the double trace moment technique which involves repeating the cascade analysis but with the flux raised to a series of different powers (Lavallée et al., 1993). All the regressions were taken over range $1.5<\log_{10}\lambda<3$ with λ defined as the ratio of the reference scale 10 km to the resolution scale (i.e. corresponding to 300 m to 10 m).

Please cite this article as: Lovejoy, S., Schertzer, D., Towards a new synthesis for atmospheric dynamics: Space–time cascades, Atmos. Res. (2010), doi:10.1016/j.atmosres.2010.01.004

Table 5
Vertical parameter estimates: These are the vertical parameters from drop sondes, corrected for the sonde intermittency. For C_1, and L_{eff} they are estimates for the part of the trajectory above 6 km.

	T	$\log\theta$	$\log\theta_E$	h	v	p	ρ
H	1.07 ± 0.18	1.07 ± 0.18	0.87 ± 0.10	0.78 ± 0.07	0.75 ± 0.05	1.95 ± 0.02	1.31 ± 0.12
C_1	0.072	0.071	0.069	0.091	0.088	0.072	0.077
α	1.70	1.90	1.90	1.85	1.90	1.85	1.95
L_{eff} (km)	5.0	4.0	25.	16.	1.3	5.0	13
δ	1.4	1.2	1.9	1.4	2.3	1.1	1.4

3.5. Intercomparison of the stratification of different fields, estimating H_z, D_{el}

We have shown that atmospheric fields are scaling over much of the meteorologically significant range in both the horizontal and vertical so that the dynamics are scaling, turbulent but anisotropic. The simplest anisotropic turbulence model involves a unique scale function for all the fields. This would imply that the ratio of horizontal and vertical components is $H_{hor}/H_{ver} = H_z =$ constant, so that for universal multifractals $\alpha_{hor} = \alpha_{ver}$ and $C_{1hor}/C_{1ver} = H_z$. In (Lilley et al., 2008) there was an extensive analysis of this for the lidar data reviewed in Section 3.3.

Combining the results from the aircraft and the drop sonde and taking into account a small apparent altitude dependence of the sonde exponents (so as estimate them at the ≈200 mb aircraft level), we obtain Table 6. It should be noted that although in Table 6 we give the ratio of the C_1 values, that since they are small, their relative errors are large and consequently their ratios have large uncertainties. Since the H's are larger, the ratio H_{hor}/H_{ver} is more reliable than C_{1hor}/C_{1ver}, indeed in the latter case the error is very hard to reliably estimate and is not indicated except in the lidar case. The main conclusion of is that T, $\log\theta$ and B are within a standard error bar of the 23/9D result $H_z = 5/9$ whereas for h it is somewhat larger. At the same time, the v, T, $\log\theta$ fields are apparently anomalously low with regard to the 23/9D prediction of 5/9; this was the conclusion of detailed trajectory by trajectory analysis of aircraft data in (Lovejoy et al., 2009c), see the summary Section 2.5.

If the ratios in Table 6 are taken at face value then we are lead to the conclusion that two or more scale functions are required to specify the scale of atmospheric structures. While this is certainly possible, let us for the moment underline the various difficulties in obtaining the in situ estimates: the nontrivial vertical outages, the nontrivial aircraft trajectory fluctuations. In addition, detailed analysis of the altitude dependence of the horizontal velocity exponent in Lovejoy et al. (2007) indicates that starting with the theoretical Boligano–Obukhov value 3/5 near the surface, that the exponent increases somewhat with altitude to the value ≈0.75 at 10–12 km. Similarly, the humidity may have both horizontal and vertical variations which may account for their high H_z values. We should therefore regard these studies as only first attempts to quantify the stratification.

4. Space–time cascades

4.1. Discussion

4.1.1. The relation between space and time in fluid mechanics

A basic property of fluid systems is that there exists a relatively well-defined lifetime for structures of a given size, the "eddy turn over time". These statistical size/duration relations are the basic physics behind the "space–time" or "Stommel" diagrammes presented in meteorology textbooks as conceptual tools, but which are in practice never empirically calculated. Likewise, although space–time relations are in fact used all the time in meteorological measurements, they are usually implicit rather than explicit, in the form of "rules of thumb". For example, many automatic digital weather stations average measurements at the fairly arbitrary period of 15 min. If the meso-scale gap existed, this might have had some justification, but if there is no gap, how long should the averaging be made? Alternatively, how often should a weather radar scan if the spatial resolution is 1 km? If it is 4 km? Conversely if only "climate" time scale (say monthly) estimates are needed what should be the spatial scale of the corresponding maps? In the same vein, in situ measurements are often considered to be "point measurements" i.e. with infinite (or very high) resolutions, but this is misleading since even if they are at points in *space*, they are never also instantaneous, i.e. they are not points in *space–time*, and it is their *space–time* resolutions that are important for their statistics.

4.1.2. The transition from weather to the climate: first principles estimates

Turning our attention to time scales of weeks to months, we may ask what is the distinction between meteorology and

Table 6
The table uses the estimate of the vertical H_v, C_{1v} from sondes (Table 2 in Lovejoy et al., 2009b). The (horizontal) values for H_h for T, $\log\theta$, h are from Table 2 (from 4–40 km, see above), for the lidar reflectivity B it is from (Lilley et al., 2008). Finally, the C_1 for v is for the range 4–40 km using flux moments. For the horizontal v, the transverse wind component was used since it was not very coherent with the altitude fluctuations and was considered more reliable.

	T	$\log\theta$	h	v	B
$\boldsymbol{H_z = H_h/H_v}$	**0.47 ± 0.09**	**0.47 ± 0.09**	**0.65 ± 0.06**	**0.46 ± 0.05**	**0.55 ± 0.02**
$H_z = C_{1h}/C_{1v}$	0.72	0.71	0.44	0.45	0.69 ± 0.2

Please cite this article as: Lovejoy, S., Schertzer, D., Towards a new synthesis for atmospheric dynamics: Space–time cascades, Atmos. Res. (2010), doi:10.1016/j.atmosres.2010.01.004

the climate? Although meteorology and climatology are increasingly considered to be distinct sciences, the actual boundary between "climate scales" and "meteorological scales" is not clear and there are no universally accepted definitions. It is still hard to improve upon the Farmer's Almanac "the climate is what you expect, the weather is what you get". For example, the National Academy of Science essentially accepts this stating in more scientific terms: "Climate is conventionally defined as the long-term statistics of the weather…" proposing only "…to expand the definition of climate to encompass the oceanic and terrestrial spheres as well as chemical components of the atmosphere" (Committee on Radiative Forcing Effects on Climate, 2005).

If there is (at least statistically) a one-to-one relation between space and time scales, we can ask what is the time scale of planetary scale structures? Let us briefly consider the consequences of applying the Kolmogorov relation $V \approx \varepsilon^{1/3} L^{1/3}$ — which we have argued holds in the horizontal up to planetary scales L (V is the typical velocity across a structure of size L, the corresponding time scale $T = L/V$). First, we can estimate the mean energy flux ε by using the fact that the mean solar flux absorbed by the earth is 200 W/m^2 (e.g. Monin, 1972). If we distribute this over the troposphere (thickness $\approx 10^4$ m), with mean air density ≈ 0.75 kg/m^3, and we assume a 2% conversion of energy into kinetic energy (Palmén, 1959; Monin, 1972), then we obtain a value $\varepsilon \approx 5 \times 10^{-4}$ m^2/s^3 which is indeed typical of the values measured in small scale turbulence (Brunt, 1939; Monin, 1972); (the geometric mean ε measured in the aircraft legs discussed in Section 2 was 4.3×10^{-4} m^2/s^3). If we now assume that the horizontal dynamics are indeed dominated by the energy flux, then we can use Kolmogov's formula to extrapolate these first principles estimates up to planetary scales to estimate the large scale velocity difference across a hemisphere, we obtain $V \approx 21$ m/s. The corresponding eddy-turn over time, lifetime, is therefore 9.5×10^5 s ≈ 11 days. This is roughly the time associated with synoptic — global scale phenomena; early analyses by (Van der Hoven, 1957; Kolesnikov and Monin, 1965; Panofsky, 1969) and others who found corresponding "synoptic" maxima in plots of $\omega E(\omega)$ versus log ω at around 4–20 days notably for temperature and pressure spectra (see e.g. Monin and Yaglom, 1975 for some early references). Below, we will discuss this with more modern data.

Although this "first principles" calculation of the weather velocity and time scales from the solar energy input is seductive, as far as we can tell, it has never been published, presumably because the Kolmogorov law was believed to only hold in its isotropic form which couldn't possibly apply to such large scales. Ironically, (Richardson, 1926) who wasn't constrained by modern notions of isotropic turbulence and claimed on the basis of original and ingenious experiments that the forerunner of the Kolmogorov 1941 law — the scaling "Richardson 4/3 diffusion" law held up to a thousand or more kilometers. Interestingly, Monin 1972 states his agreement with this wide range for the 4/3 law but uses the speed of sound rather than the eddy velocity to deduce a "synoptic" length scale! Let us now show with the help of the state-of-the-art ECMWF interim reanalysis (for Jan. 2006) that use of the Kolmogorov law in the horizontal up planetary scales (implying anisotropic turbulence) is indeed well justified. We can estimate $\varepsilon \approx \Delta v^3/\Delta x$ at small (3°) scales using east–west, north–south and "isotropic" estimates (the smallest 1.5° resolution data was slightly too smooth due to the hyperviscosity used in the reanalyses and so that the 3° lags were used). Fig. 15a shows the resulting ε averaged over the troposphere ($p > 200$ mb) as a function of latitude; since the theory assumes that the fluid density is constant when averaged over different levels, we have weighted the ε estimates from the different pressure levels by the air density. Fig. 15b the mean shows ε as a function of pressure level averaged over latitudes (no density weighting). We can see that the midlatitudes have up to 10 times the mean ε as the equator and that it is mostly concentrated in the upper troposphere (near the 300 mb level) where it is about 5–6 times that of the lower atmosphere. Also indicated (dashed line) is the overall (isotropic, density weighted) mean 9.25×10^{-4} m^2/s^3 which is within a factor of 2 of the first principles estimate above (the comparable figures for the east–west and north–south gradients are 7.50×10^{-4} m^2/s^3 and 1.40×10^{-3} m^2/s^3).

We can now compare this "first principles" estimate to the observed mean "hemispheric antipode" velocity differences (i.e. the opposite side of the earth in the same hemisphere; we found that this is very close to the true antipode difference). We see (Fig. 15c) that it follows the same pattern with latitude as the variations of ε. The overall means (averaging over $p > 200$ mb) are 11.1 m/s, 7.43 m/s, 14.7 m/s for the east–west component, north–south component and vector difference respectively. If we now use the ε estimated at 3° to infer the 180° difference using the Kolmolgorov law (i.e. over a factor of 60 in scale), then the extrapolated velocity difference is really the cube root of the mean cube; this is shown in Fig. 15d (along with the mean and rms values). We see that the agreement between the predicted hemispheric antipodes difference and the observed difference is to within ±19% but is even better between 30°N and 10°S. where it is to within ±7%. We may also compare the overall means to the "first principles" estimate (21 m/s): the mean of the cubic estimate is 17.33 ± 5.7 m/s and the mean "extrapolated" large scale velocity difference is 20.7 ± 7.4 m/s (the error bars represent the spread in the values for different latitudes).

We can now re-estimate the lifetime ("eddy turn-over time") $T = L/V$ of the largest (planetary scale) eddies. Using the isotropic ε estimate, we obtain $T = 8.7 \times 10^5$ s $= 10.0$ days which is quite close to the "first principles" estimate (11 days) and to those of (Radkevitch et al., 2008) who used analyses at a scale 6000 km to determine the statistical distribution of eddy turn-over times finding a mean of 9.5×10^5 s with only a narrow dispersion.

The extrapolation of the small scale velocity differences to planetary scales was based on the assumption that the energy flux was indeed independent of scale, it is important to verify this directly. Fig. 15e shows the calculation of $\Delta v^3/\Delta x$ where Δv is the modulus of the vector difference and Δx is taken as a zonal and meridional lag, averaging over the entire troposphere ($p > 200$ mb) and averaging over all longitudes and latitudes between ±45° latitude. We can see that although there is a huge variability (the one standard deviation latitude to latitude variations of the log corresponds to variations of a factor ≈ 3 about the mean) that the mean is relatively constant; to within a factor of ≈ 1.7 over the range 330–

Please cite this article as: Lovejoy, S., Schertzer, D., Towards a new synthesis for atmospheric dynamics: Space–time cascades, Atmos. Res. (2010), doi:10.1016/j.atmosres.2010.01.004

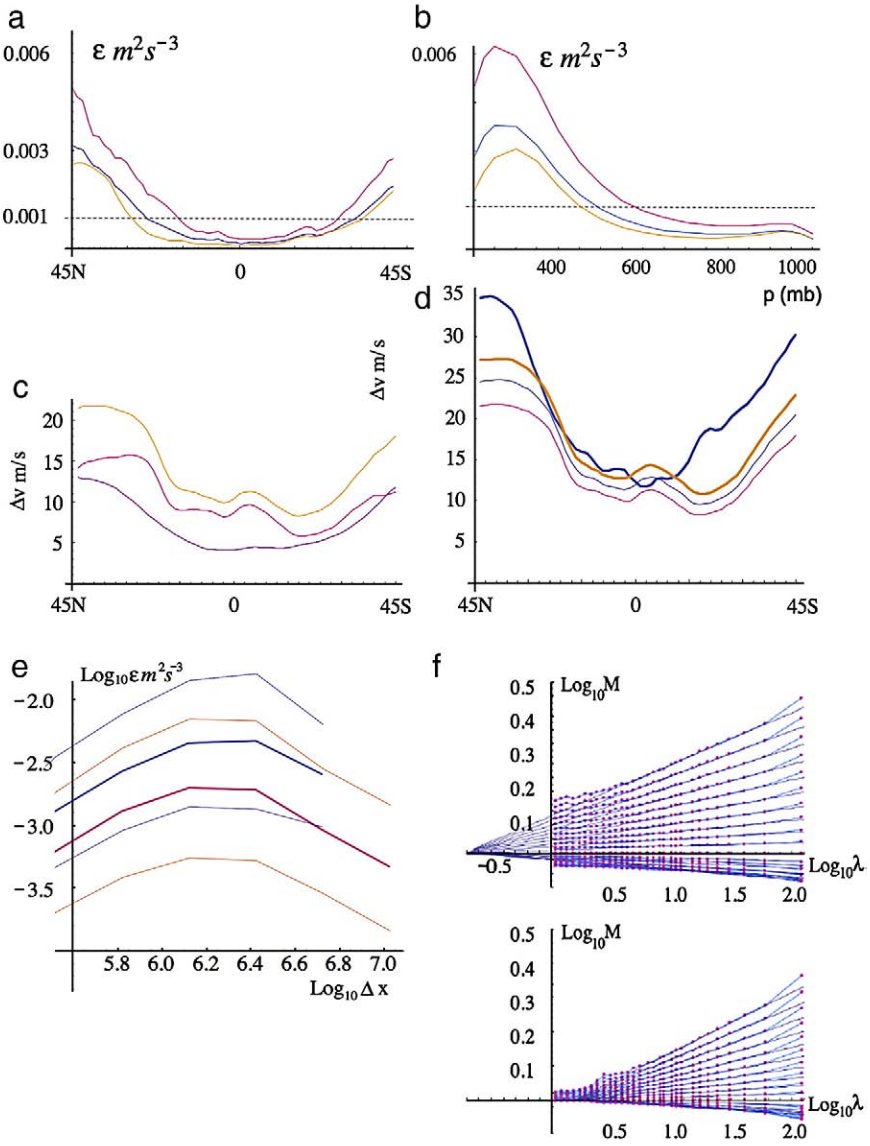

Fig. 15. a–d: From ECMWF interim for Jan. 2006. a: upper left: Estimates of ε using gradients of the vector wind at resolution (3°: 330 km at equator), all averages over <200 mb levels, as functions of latitude starting at 45 N, the contribution from the different pressure levels have been weighted by the air density. Orange is based on EW gradients, red, on NS gradients and blue is an isotropic average using the mean variance in NS and EW directions. The dashed line is isotropic latitude average = 0.00093 m^2/s^3. b: upper right: The same (without density weighting) this time averaged over latitudes and given as a function of pressure level. c: middle Left: This shows the hemispheric antipode mean difference in velocity averaged over <200 mb. Orange is the vector difference, red is the NS component difference and orange is the EW component difference. Very similar results are obtained for the true antipode differences. d: middle Right: Blue is the predicted hemispheric antipode large scale difference obtained from the isotropic estimate of ε (upper left; 20.7 ± 7.37 m/s) and Kolmogorov's law, the orange is the cube root of the mean cube hemispheric difference (17.3 ± 5.7 m/s), the dark blue, the root mean square (15.7 ± 5.2 m/s), the pink, the mean (same as orange at left, 13.8 ± 4.6 m/s). e: This shows zonal (solid red, error bars orange; these are latitude to latitude variations), and meridional (solid blue, error bars thin blue) error bars are one standard deviation of the logarithm, Δx is in meters. Averaging was over layers below 200 mb and was weighted by the air density. Data, same as above: Jan. 2006, ±45° latitude. f: The ECMWF interim reanalysis of the zonal wind in the east–west direction (top), and the north–south direction (bottom) for moments $q = 0.1, 0.2, \ldots 1.9, 2.0$, averaged over all the layers below 200 mb and obtained by using the finite difference Laplacian at the smallest scales (same data as above for January 2006). Analysis of the meridional component gave virtually identical results and is not shown. The outer scale ($\lambda = 1$) is 180 degrees; this corresponds to an average of 12,700 km in the EW direction (averaging over latitudes; in the NS direction it is 20,000 km.

10,000 km. From the figure, we can see that the success of the extrapolation was partially due to the smooth "hump" near 2000 km so that the estimates of ε at large and small scales are very close. These results are more evidence against the existence of a 2-D regime, since in the latter, $H = 1$ so that in a 2D regime, $\Delta v \propto \Delta x$ and velocity differences build up much faster (i.e. $\varepsilon \approx \Delta v^3/\Delta x \approx \Delta x^2$ rather than being constant with scale).

Although small in magnitude, the scale dependence of the energy flux (the "hump" in Fig. 15e) deserves closer scrutiny, in particular we should compare it with the direct analysis of the turbulent flux as outlined in Section 2, i.e. without the

Please cite this article as: Lovejoy, S., Schertzer, D., Towards a new synthesis for atmospheric dynamics: Space–time cascades, Atmos. Res. (2010), doi:10.1016/j.atmosres.2010.01.004

explicit assumption that the cascading quantity is the energy flux. Fig. 15f shows the result for the zonal wind; the cascade is respected extremely well (from 300 to 5000 km, root mean square residues with respect to the regression shown are ≈±0.2%). There is no sign of the "hump" (Fig. 15e) near 2000 km (i.e. $\log_{10}\lambda = 1$), the deviations from pure

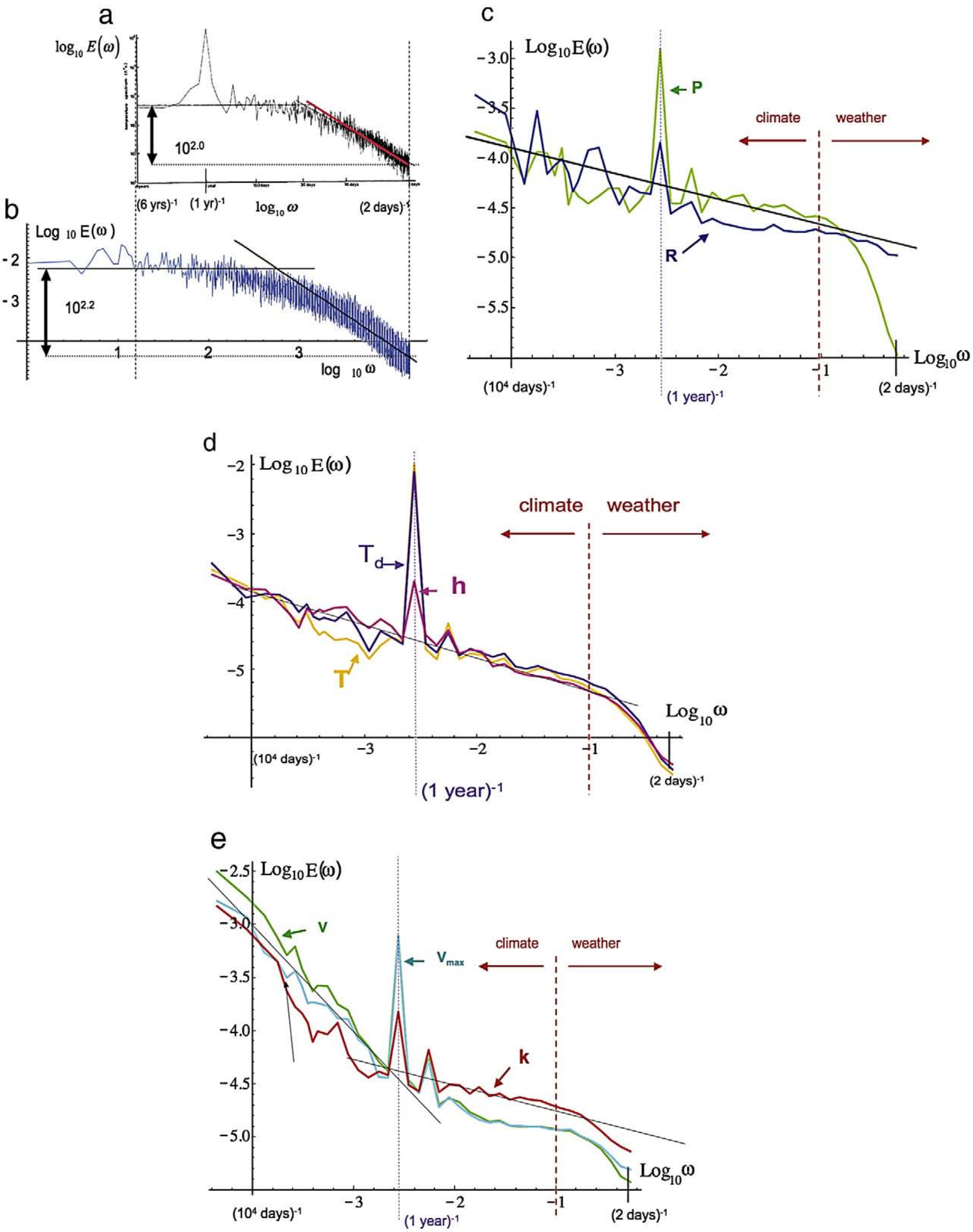

Please cite this article as: Lovejoy, S., Schertzer, D., Towards a new synthesis for atmospheric dynamics: Space–time cascades, Atmos. Res. (2010), doi:10.1016/j.atmosres.2010.01.004

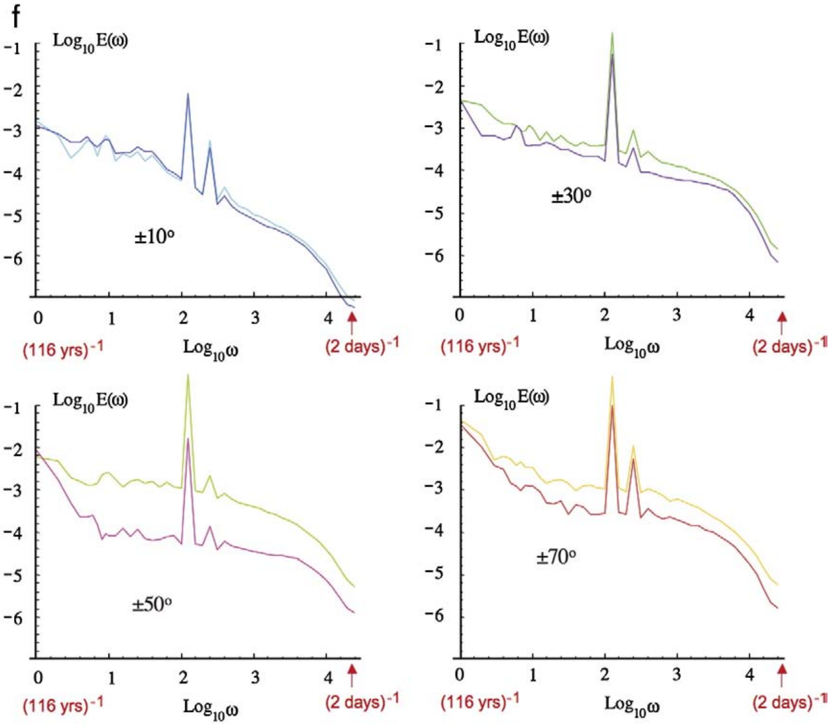

Fig. 16. a (top): The spectral plateau; reproduced from Lovejoy and Schertzer (1986). This is the average of 5 daily temperature series each 6 years long from a station in France. The red reference slope is -2; this is the estimate for β using $H=0.60$ (from Tables 3a, 3b) and an intermittency correction $K(2)=0.2$ (i.e. as predicted if the horizontal and temporal exponents are equal). The faint black reference lines have slopes 0, $-5/3$. Note the strong annual cycle and the change of about a factor of 10^2 between the daily variance and the low frequency variance. b (bottom): The spectrum is well reproduced by the multifractal model (Section 4.4) which is simply the extrapolation of the turbulence model to time scales longer than the lifetime of a planetary size eddy (taken here as 16 simulated days). We show the average of 12 simulations of daily temperature, over 90 years, see the details in Section 4.4. The straight line has the theoretical slope -1.47 corresponding to $\alpha=1.8$, $C_1=0.1$, $H=1/3$ (this was a simulation of the horizontal wind so the H was a little lower than for T, but this only slightly changes the slope at the high frequency "meteorological" part of the spectrum. c: Mean spectrum of daily pressure (P) and rain amount (R) from 24 stations with long (60 year; 22,200 days) records, from a 2° grid. The reference slope is -0.25, and the spectrum was averaged over 1d$B\omega$ bins (i.e. 10 per order of magnitude in frequency), every 2° from 30–50 NS, -105 to -71 EW. Note that the actual spectral spike at 1 year is much narrower than this log discretised plot indicates, also the spectra have been nondimensionalized by their variances. d: Same as c but for variables with slightly steeper "plateau", here the reference line has slope -0.5 (dew point temperature, temperature and relative humidity). e: Same as c but for the variables displaying a new low frequency scaling regime: wind (v), "gusting wind" (v_{max}) and "effective" extinction coefficient (inverse visibility). The reference slopes are -1, -0.5. f: 20th C reanalysis spectra of daily temperatures by latitude band. In each graph, the top of the two is always northern hemisphere, the bottom of two is the corresponding southern hemisphere curve. Each is averaged over 10 bins per order of magnitude in frequency.

multiplicative cascade behaviour are for scales larger than around 5000 km. Finally here, although the scale by scale exponents are nearly the same ($C_{1EW}=0.095$, $C_{1NS}=0.092$), the "trivial" anisotropy is quite strong, the effective outer scales being 6×10^4 km in the EW direction but in the NS direction it is only 12,500 km. This implies that the variability of the turbulent fluxes is greater in the EW direction than in the NS direction; this is contrary to the observations of Δv gradients in Fig. 15a, b. We conclude that the cascading quantity is only approximately the energy flux; this underscores the nontrivial relations between the cascades and the observables (here the wind).

4.1.3. The weather–climate transition, the "spectral plateau"

We have mentioned that early workers noted a maximum in plots of $\log\omega-\omega E(\omega)$ at the "synoptic maximum", which — due to the apparent validity of the Kolmogorov law in the horizontal — we have identified with the eddy turn over time of planetary scale structures. If the same spectra are plotted on $\log\omega-\log E(\omega)$ plots then the appearance is no longer of a "maximum" with a fall-off on either side, but rather a range with a "spectral plateau"; at low frequencies and a linear fall-off at higher frequencies. More precisely, at frequencies lower than $1/T$, the spectrum is roughly flat (β is low; see below) while at higher frequencies (ignoring possible spikes at diurnal frequencies and harmonics) it is roughly a power law. In other words, we apparently have a transition between two power law regimes (or at least between a high frequency power law and a broad low frequency transition regime). Given the foregoing, it is natural to identify the high frequency one with the weather, and the low frequency one with the climate. Indeed, breaks with similar interpretations in temporal scaling have been observed in temperature spectra (Lovejoy and Schertzer, 1986) and in spectra of rain rates from gauges (Ladoy et al., 1991; Tessier et al., 1996; Koscielny-Bunde et al., 1998; Pellieter and Turcotte, 1999; Talkner and Weber, 2000). Fig. 16a shows the temperature spectrum for a station in France which — at least for scales less than ≈2 months — is very close to the IR satellite spectra from MTSAT (see below) as well as to a the temporal extrapolation of the space–time turbulent "weather" model (Fig. 16b) discussed in Section 4.4.

Please cite this article as: Lovejoy, S., Schertzer, D., Towards a new synthesis for atmospheric dynamics: Space–time cascades, Atmos. Res. (2010), doi:10.1016/j.atmosres.2010.01.004

Using more recent analyses from stations from the eastern United States. We can study the behaviour of other fields, see Fig. 16c, d, e. The stations were taken from a $2^o \times 2^o$ grid from 30^o–50^o north, 105^o to 71^o west and only those with particularly long records (daily for 22,200 days ≈60 years) were selected so as to identify possible very low frequency scaling regimes. The available data type and number of near complete long series stations were for rain rate (3 stations), pressure (7 stations), temperature (39 stations), dew point (23 stations), wind (36 stations), maximum wind (27 stations), humidity (23 stations) and effective extinction coefficient (inverse visibility; 33 stations). We see that the plateau is not really flat, and that at least for wind and the "effective" extinction coefficient (inverse visibility) that there appears to be a new low frequency regime (with $\beta \approx 1$) for frequencies below ≈ $(1\text{ year})^{-1}$.

The station data analyzed in Fig. 16c, d, e are from a relatively narrow latitude band (continental US) so that it is interesting to study the effect of latitude variation. Fig. 16f shows this using the near surface (0.995 sigma level) temperature fields form the 20thC reanalysis. We see that the plateau is most pronounced (flattest) at midlatitudes and is symmetric with respect to the equator (the main exception being $\pm 50^o$). Indeed, the plateau all but disappears into a continuous scaling regime near the equator ($\pm 10^o$). In addition, all the figures show evidence of a new low frequency regime at frequencies $<(10\text{ years})^{-1}$. This is roughly consistent with the in situ station spectrum (Fig. 16d) and indicates long range correlations in the climate system. Note that this contradicts the usual assumption that the correlations decay exponentially on decadal time scales with little correlation remaining after 10–20 years (Fig. 17). These are conclusions are strongly supported by the analyses of Huybers and Curry, 2006.

The same transition from a power law $E(\omega) \approx \omega^{-\beta}$ with exponent $\beta \approx 1.5$–2 for frequencies $> \approx (10\text{ days})^{-1}$ to the lower frequency plateau has been reproduced by several authors (Koscielny-Bunde et al., 1998; Pellieter and Turcotte, 1999; Talkner and Weber, 2000), but most researchers study the climate regime directly by considering monthly averaged data effectively studying the spectral plateau directly. See for example (Blender and Fraedrich, 2003; Huybers and Curry, 2006) who find β closer to 0 over land and to 1 over oceans, with the "plateau" regime extending at least to decades.

The scale break marking the weather/climate transition has been used as the empirical basis for the Stochastic Linear Forcing (SLF) paradigm modeling of climate scale fluctuations, and the analysis procedure called "Linear Inverse Modelling" (LIM). The idea is to use the weather/climate scale separation to define rapidly-varying fluctuations with respect to lower frequency (e.g. weekly, monthly) averages and to exploit the short range correlations of the resulting fluctuations, and the apparently near white noise spectral "plateau" region discussed above; see (Hasselmann, 1976; Penland, 1996). SLF models, when interpreted as providing the most probable forecast, assumes the plateau to be nearly Gaussian; however, Gaussianity is not required for most of SLF's diagnostic products, as long as the dynamical description is well approximated as linear. Today, for many purposes —including sea surface temperature anomalies, diabatic heating rates and El Nino — SLF techniques are among the best available for forecasting (Penland and Sareshmuhk, 1995; Newman et al., 2003; Sardeshmuhk et al., 2000). At present, the impact on LIM techniques of possible long range correlations in the spectral plateau region — or of the near log-Levy long-tailed flux distributions discussed below are not clear.

In the next subsection we extend the anisotropic spatial turbulence model discussed in Section 3 to anisotropic space–time turbulence (Section 4.1.1); we will see that this analysis justifies the above interpretation quite straightforwardly. In any case, convincing justification of the model requires the systematic establishment of space–time relations over the entire range of small to large scales. This is our task in Sections 4.2.4 and 4.3 where we extend the empirically determination of space–space to space–time diagrammes.

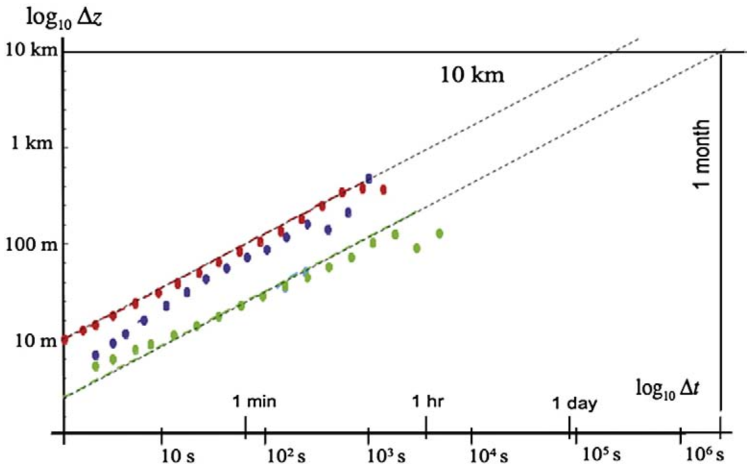

Fig. 17. The is a space–time (vertical/time) diagramme obtained from the first order structure functions of 3 lidar time series at 1 s (red) and 2 s (blue, green) resolutions. At the largest scales, the statistics are not as good. We see that that troposphere thickness (which corresponds roughly to planetary sizes in the horizontal) has a time scale of several weeks to a month, see Section 4.1.2. Assuming that $l_s = 1$ m, the top line corresponds to $v = 60$ m/s, The bottom line to 5 m/s. If instead $l_s = 10$ cm, the top line implies 400 m/s, the bottom line to 30 m/s. This is estimated using the formula: $v\Delta t/l_s = (\Delta z/l_s)^{1/H_z}$. We thank A. Radkevitch for the help with this analysis.

Please cite this article as: Lovejoy, S., Schertzer, D., Towards a new synthesis for atmospheric dynamics: Space–time cascades, Atmos. Res. (2010), doi:10.1016/j.atmosres.2010.01.004

4.1.4. From the spectral plateau to very low frequencies

Lovejoy and Schertzer (1986) proposed a general scaling framework for analyzing climate fluctuations over huge ranges, covering the scale range of minutes to hundreds of thousands of years (using temperatures and paleotemperatures). They divided up the frequency domain into three basic regimes all with roughly power law spectra: the high frequency weather regime up to scale T with $\beta\approx1.8$, an intermediate "spectral plateau" with β small (near zero) and then — starting at a low frequency corresponding to scales of several hundred years, another $\beta\approx1.8$ regime becoming again a plateau for $\omega<(40{,}000\text{ years})^{-1}$. The same basic scaling framework was also adopted by Schmitt et al. (1995), Pellieter and Turcotte (1999) and Huybers and Curry (2006) all of whom came to very similar conclusions. For example, Lovejoy and Schertzer (1986) and Pellieter and Turcotte (1999) argue on the basis of a nearly four century long series from central England that the plateau finally ends at scales of several hundred years. The same conclusion was reached with the help of paleo temperatures in Lovejoy and Schertzer (1986), Schmitt et al. (1995) and Huybers and Curry (2006). Beyond the end of the low β plateau these studies as well as (Ashkenazy et al., 2003) estimated that a new scaling regime then begins with agreement that the lower frequency exponents β are in the range $\approx$1.3–1.8 and they concur that the latter scaling regime is apparently again replaced by a new plateau at frequencies below $\approx(40{,}000\text{ years})^{-1}$. Lovejoy and Schertzer (1986) also point out that once the time scale of the beginning of this new scaling regime is determined, that the exponent is fairly tightly constrained (according to them, near $\beta\approx1.7$) by the requirement that the extraoplation to the end of the regime at $\omega\approx(40{,}000\text{ years})^{-1}$ leads to plausible variations in the mean glacial/inter glacial temperature changes.

The explanation for the end of the low frequency part of the spectral plateau is not clear, although we could mention the proposal in Lovejoy and Schertzer (1986). Based on the observation that the spectra of spatially averaged northern hemisphere temperatures show that the plateau only continues out to about five years (rather than several hundred for the spatially "local" temperatures discussed above), they quantitatively showed that the extrapolation of the mean instrumental northern hemisphere temperature fluctuations from about 5 years to longer periods would lead them to dominate the local variations at about 300 years. In other words for scales longer than this, the primary signal is the fluctuation in the entire temperature of the earth whereas for shorter scales, it is predominantly due to local variations.

4.1.5. Limits to predictability, forecasting

Clear knowledge of space–time relations are also needed in forecasting. This is because small scale perturbations grow progressively, "polluting" the larger scales via an inverse cascade of errors (Lorenz, 1969). To see how this works, approximate the inverse cascade via a series of cascade steps, each over an octave in scale. The time for the error to propagate from one octave to the next larger one is roughly the corresponding eddy-turn over time/lifetime. The overall limits to predictability are obtained by summing over all the octaves from smallest to largest. If we now consider the classical 2-D/3-D paradigm, we find in 3-D turbulence (dominated by energy fluxes ε) a structure of size L has the lifetime $\tau_e=\varepsilon^{-1/3}L^{2/3}$. In 2-D enstrophy cascades it is independent of size $\tau_e=\zeta^{-1/3}$ where ζ is the enstrophy flux. The result is that in 3-D the overall limit is the sum of a converging algebraic series (nearly equal to the turn-over time of the largest structure), whereas in 2-D it can in principle be much larger than this depending on the overall number of octaves in the enstrophy cascade. In our anisotropic cascade model, the horizontal is still dominated by ε so that the limits to predictability are still roughly equal to the eddy turn over time of the largest eddy, i.e. about 10 days. This is indeed the frequently cited predictability limit (see e.g. Lorenz, 1969) which is based on a statistical closure; see the update (Rotunno and Snyder, 2008)). It should be mentioned that the above picture needs important nuances, since Schertzer and Lovejoy (2004) show that in multifractal cascades, the error growth is actually highly intermittent, coming in "puffs".

4.2. Anisotropic space–time turbulence

4.2.1. Space–time scale functions

In Sections 2 and 3 we have argued that atmospheric variables including the wind have wide range (anisotropic) scaling statistics. Dimensionally, a velocity is needed to connect space and time and physically the wind advects the fields. Therefore it is hard to avoid the conclusion that spatially scaling fields should also be (anisotropically) scaling in space–time (and hence be the result of space–time cascade processes). While we argue that this is indeed true, space–time scaling is unfortunately somewhat more complicated than pure spatial scaling. At meteorological time scales this is because we must take into account the mean advection of structures and the Galillean invariance of the dynamics. At longer climatological time scales, this is because we consider the statistics of many lifetimes ("eddy-turn-over times") of structures. We first consider the shorter timescales. This discussion is a summary of a more detailed one in Lovejoy et al. (2008).

In order to illustrate the formalism, we shall discuss the example of the horizontal wind v. Let us consider the 23/9D model (Section 3) in which the energy flux ε dominates the horizontal and the buoyancy variance flux dominates ϕ the vertical so that horizontal wind differences follow:

$$\begin{aligned}\Delta v(\Delta x) &= \varepsilon^{1/3}\Delta x^{1/3}; a \qquad (20)\\ \Delta v(\Delta y) &= \varepsilon^{1/3}\Delta y^{1/3}; b\\ \Delta v(\Delta z) &= \phi^{1/5}\Delta z^{3/5}; c\\ \Delta v(\Delta t) &= \varepsilon^{1/2}\Delta t^{1/2}; d\end{aligned}$$

where Δx, Δy, Δz, Δt are the increments in horizontal coordinates, vertical coordinate and time respectively. Eqs. (20a), (20b) describe the real space horizontal Kolomogorov scaling and 20 c the vertical Bolgiano–Obukhov (BO) scaling for the velocity, the equality signs should be understood in the sense that each side of the equation has the same scaling properties. The anisotropic Corrsin–Obukov law for passive scalar advection is obtained by the replacements $v\rightarrow\rho$; $\varepsilon\rightarrow\chi^{3/2}\varepsilon^{-1/2}$ where ρ is the passive scalar density, χ is the passive scalar variance flux. We have

Please cite this article as: Lovejoy, S., Schertzer, D., Towards a new synthesis for atmospheric dynamics: Space–time cascades, Atmos. Res. (2010), doi:10.1016/j.atmosres.2010.01.004

included Eq. (20d) which is the result for the pure time evolution in the absence of an overall advection velocity; this is the classical Lagrangian version of the Kolmogorov law.

Following the developments in Section 3, we can express the scaling (Eq. (20)) in a single expression valid for any space–time vector displacement $\underline{\Delta R}=(\underline{\Delta r},\Delta t)=(\Delta x,\Delta y,\Delta z,\Delta t)$ by introducing a scalar function of space–time vectors called the "(space–time) scale function", denoted $[\![\underline{\Delta R}]\!]$, which satisfies the fundamental (functional) scale equation:

$$[\![\lambda^{-G_{st}}\underline{\Delta R}]\!]=\lambda^{-1}[\![\underline{\Delta R}]\!];\ G_{st}=\begin{pmatrix}G_s & 0\\ 0 & H_t\end{pmatrix};\ H_t=(1/3)/(1/2)=2/3 \tag{21}$$

where G_s is the 3×3 matrix spatial generator (Eq. (16)) and G_{st} is the extension to space–time.

Using the space–time scale function, we may now write the space–time generalization of the Kolmogorov law (Eq. (20)) as:

$$\Delta v(\underline{\Delta R})=\varepsilon_{[\![\underline{\Delta R}]\!]}^{1/3}[\![\Delta R]\!]^{1/3} \tag{22}$$

where the subscripts on the flux indicate the space–time scale over which it is averaged.

The result analogous to that of Section 3, the corresponding simple ("canonical") space–time scale function is:

$$[\![\underline{\Delta R}]\!]_{can}=l_s\left(\left(\frac{\|\underline{\Delta r}\|}{l_s}\right)^2+\left(\frac{|\Delta t|}{\tau_s}\right)^{2/H_t}\right)^{1/2} \tag{23}$$

(see Marsan et al., 1996). Where $\tau_s=\phi^{-1/2}\varepsilon^{1/2}$ is the "sphero-time" analogous to the sphero-scale $l_s=\phi^{-3/4}\varepsilon^{5/4}$.

4.2.2. Advection and Gallilean invariance

The above is missing a key ingredient: advection. When studying laboratory turbulence generated by an imposed flow with velocity V with superposed turbulent fluctuations, (Taylor, 1938) proposed that the turbulence is "frozen" such that the pattern of turbulence blows past the measuring point sufficiently fast so that it doesn't have time to evolve; i.e. he proposed that the spatial statistics could be obtained from time series by the deterministic transformation $V\Delta t->\Delta x$. While this transformation has been frequently been used in interpreting meteorological series, it can only be properly justified by assuming the existence of a scale separation between small and large scales so that the large scales really do blow the small scale (nearly "frozen") structures past the observing point. Since we have argued that there is no scale separation in the atmosphere this becomes problematic.

However, if we are only interested in the statistical relation between time and space and the system is scaling, then advection can be taken into account using the Gallilean transformation matrix A:

$$A=\begin{pmatrix}1 & 0 & 0 & u\\ 0 & 1 & 0 & v\\ 0 & 0 & 1 & w\\ 0 & 0 & 0 & 1\end{pmatrix} \tag{24}$$

where the mean wind vector has components: $\underline{v}=(u,v,w)$ (Schertzer et al., 1998). The new generator is $G_{st,advec}=A^{-1}G_{st}A$ and the scale function $[\![\Delta R]\!]_{advec}$ which is symmetric with respect to $G_{st,advec}$ is: $[\![\Delta R]\!]_{advec}=[\![A^{-1}\underline{\Delta R}]\!]$. The canonical advected scale function is therefore:

$$[\![\Delta R]\!]_{advec,\,can}=[\![A^{-1}\Delta R]\!]_{can}=l_s\left(\left(\frac{\Delta x-u\Delta t}{l_s}\right)^2+\left(\frac{\Delta y-v\Delta t}{l_s}\right)^2+\left(\frac{\Delta z-w\Delta t}{l_s}\right)^{2/H_z}+\left(\frac{\Delta t}{\tau_s}\right)^{2/H_t}\right)^{1/2} \tag{25}$$

Note that since $D_{st,advec}=TrG_{st,advec}=Tr(A^{-1}G_{st}A)=TrG_{st}=D_{st}$, constant advection does not affect the elliptical dimension (see however below for the "effective" G, D).

4.2.3. Advection in the horizontal

Formula 25 is valid due to the Gallilean invariance of the equations and boundary conditions; it assumes that the advection velocity is essentially constant over the region and independent of scale. We now consider this in more detail. We will only consider horizontal advection (put $w=0$; the interesting but nontrivial effects of the vertical velocity on the temporal scaling are discussed in Lovejoy et al. (2008b)). If we apply the formula over a finite region with relatively well-defined mean horizontal velocity, then it should apply (see the discussion in (Lovejoy et al., 2008b)). But what about applying it to very large e.g. global scale regions where the mean velocity is small (if only because of rough north–south symmetry)? However, even if we consider a flow with zero imposed mean horizontal velocity (as argued by (Tennekes, 1975)) in a scaling turbulent regime with $\Delta v_l\approx\varepsilon^{1/3}l^{1/3}$, the typical largest eddy (size L) will have a mean velocity $V\approx\Delta v_L\approx\varepsilon_L^{1/3}L^{1/3}$ and will survive for the corresponding eddy turn over time $\tau_{\varepsilon,L}=T=L/V=\varepsilon_L^{-1/3}L^{2/3}$ estimated as ≈ 10 days above. In other words, if there is no break in the scaling then we expect that structures will be advected by the largest structures in the scaling regime.

With this estimate of the horizontal velocities to insert in Eq. (25), let us compare them to the Lagrangian term $(\Delta t/\tau_s)^{1/H_t}$ considering only the temporal variations (i.e. take $\Delta x=\Delta y=\Delta z=0$) and taking horizontal axes such that the advection term is $V\Delta t/l_s$. By definition, the sphero-time τ_s satisfies: $l_s=\varepsilon^{1/2}\tau_s^{1/2}$ and since $T=V^2/\varepsilon$ we see that the condition that the pure temporal evolution term is negligible (i.e. that $V\Delta t/l_s>(\Delta t/\tau_s)^{3/2}$) is $\Delta t<T$ so that the term $(\Delta t/T)^3$ only becomes important for $\Delta t>T\approx 10$ days. However, since the physical size of the eddies with lifetime $\Delta t=T$ is already the size of the planet (L), presumably the term ceases to be valid for scales $\Delta t>T$. Nevertheless, it may play a modest role in breaking the scaling for Δt comparable to T, i.e. for the transition from weather to climate.

Neglecting the Δt^3 term, we can now use this information to rewrite the horizontal scale function (Eq. (25) with $w=0$) in terms of L, T and V instead of l_s, τ_s. First consider overall (non-random) advection (v_x,v_y), the nondimensional scale function is:

$$\begin{aligned}[\![\underline{\Delta r}]\!]&=\left(\left(\frac{\Delta x-v_x\Delta t}{L}\right)^2+\left(\frac{\Delta y-v_y\Delta t}{L}\right)^2\right)^{1/2}\\&=\left(\left(\frac{\Delta x}{L}\right)^2+\left(\frac{\Delta y}{L}\right)^2+\left(\frac{\Delta t}{T}\right)^2-2\left(v_x\frac{\Delta x}{L}+v_y\frac{\Delta y}{L}\right)\left(\frac{\Delta t}{T}\right)\right)^{1/2};\ \Delta t<T\end{aligned} \tag{26}$$

where $T=L/(v_x^2+v_y^2)^{1/2}$. The statistics of the intensity gradients of real fields influenced by random turbulent velocity fields should involve powers of scale functions such as the above but with "average" velocities. In this case we introduce the nondimensional variables:

$$\Delta x' = \frac{\Delta x}{L};\ \Delta y' = \frac{\Delta y}{L};\ \Delta t' = \frac{\Delta t}{T};\ \mu_x = \frac{\langle v_x\rangle}{V};\ \mu_y = \frac{\langle v_y\rangle}{V} \qquad (27)$$

with:

$$T = \frac{L}{V};\quad V = \left(\left\langle v_x^2\right\rangle + \left\langle v_y^2\right\rangle\right)^{1/2} \qquad (28)$$

Note that here V is a large-scale turbulent velocity whereas $<v_x>$, $<v_y>$ are given by the overall mean advection in the region of interest. In terms of the nondimensional quantities:

$$\|\underline{\Delta r}\| \approx \left(\underline{\Delta r}'^{T} B\, \underline{\Delta r}'\right)^{1/2};\ B = \begin{pmatrix} 1 & 0 & -\mu_x \\ 0 & 1 & -\mu_y \\ -\mu_x & -\mu_y & 1 \end{pmatrix}; \qquad (29)$$
$$\underline{\Delta r}' = \left(\Delta x', \Delta y', \Delta t'\right)$$

If we assume that the structure function of a field I (e.g. an IR radiance) is scaling, then this implies the scaling of the spectral density (P in a space dimension with $D=3$), with a (different) Fourier space (represented by a tilda) scale function:

$$\left\langle \Delta I^2 \right\rangle \approx \|\underline{\Delta r}\|^{2H};\ P\left(\underline{K}\right) = \left\langle \left|\tilde{I}\left(\underline{K}\right)\right|^2 \right\rangle \approx \|\underline{K}\|^{-s};\ s = D-2H$$
$$\|\underline{K}\| = \left(\underline{K}^T \underline{\underline{E}}\ \underline{K}\right)^{1/2};\ \underline{\underline{E}} = \frac{1}{1-\left(\mu_x^2 + \mu_y^2\right)} \times \begin{pmatrix} 1-\mu_y^2 & \mu_y\mu_x & -\mu_x \\ \mu_y\mu_x & 1-\mu_y^2 & -\mu_y \\ -\mu_x & \mu_y & 1 \end{pmatrix};\ \underline{K} = \left(k_x, k_y, \omega\right) \qquad (30)$$

These equations imply that the space–time anisotropy can be approximated by ellipsoids whose characteristics are determined by the magnitude of the dimensionless horizontal wind. But these ellipsoids have the same shapes at all scales; in space–time the scale by scale anisotropy is thus "trivial", the effective space time generator $G_{s,eff}$ in (x,y,t) space is the identity. In Pinel (in preparation), this spectral form was used to analyze the MTSAT images discussed in section 4.3.1; with optimum parameters $s=3.5$, $L=35{,}000$ km, $T=930$ *hrs* (=39 days), $V=9.3$ m/s and $<v_x>=-3.1$ m/s and $<v_y>=0.0$ m/s.

The turbulence analysis just described can be compared with the more traditional wave space–time analyses. Wheeler and Kiladis (1999), Hendon and Wheeler (2008) have pioneered the use of space–time spectra of daily mean fields of outgoing long wave radiation to infer the presence and activity of various atmospheric wave modes. Aside from certain minor (preprocessing) differences, probably the most significant difference is that in order to find evidence of waves, the Wheeler–Kiladis technique attempts to remove an ill-defined "background". This is necessary since any wave signal is very small compared to the main spectral level. Our method on the contrary attempts to analyse/model this main "background" (i.e. turbulence) signal, ignoring residual wave contributions. Work in progress attempts to bring the wave induced residuals into a scaling framework.

4.2.4. Space–time diagrammes from lidar

Following the construction of the "space–space" diagramme showing the relation of horizontal to vertical scales (Section 3), we can use first order structure functions to determine "space–time" or "Stommel" diagrammes from the lidar (z,t) data described in Radkevitch et al. (2007), Radkevitch et al. (2008). To do this, for a given Δt, the corresponding $\Delta z(\Delta t)$ is determined by the solution of the implicit equation for the first order structure functions $\langle|\Delta B(\Delta z)|\rangle = \langle|\Delta B(\Delta t)|\rangle$ (B is the lidar backscatter ratio). For three of the longer (z,t) sections from Section 4.3.1, the results are shown in Fig. 18a, we see that the data follow reasonably accurately the theoretical curve (assuming horizontal wind dominated temporal statistics and $H_z = 5/9$). In addition, if the sphero-scale is assumed to be 1 m (roughly what was determined for the vertical section data in Fig. 13c), then we find horizontal wind in the range 5–60 m/s which is quite reasonable. We also see that the space–time diagramme gives direct evidence that the top of the troposphere (10 km) corresponds to the outer time scale ≈2 weeks.

4.3. Evidence from satellite radiances: horizontal–time analyses

4.3.1. MTSAT thermal IR

The lidar data considered in the previous section allows us to determine the space–time properties of vertical spatial scales up to kilometers and time scales of seconds to hours. If we seek to study the relation of horizontal to temporal scales, then satellite data is ideal. In Section 2.3 we used TRMM and MTSAT satellite radiances to examine the large horizontal scale statistical properties of passive and active microwaves, visible and infra red radiation. We can use the same methodology — the systematic degradation of fluxes estimated from absolute gradients — to degrade the same data in the time domain. For this purpose, the TRMM satellite has the disadvantage of having an average 2–4 day return time (depending on the wavelength and location) so that it has poor temporal resolution. Let us therefore first examine the MTSAT thermal IR data with 1 hour resolution. Since we find that 1 hour corresponds to about ≈30 km, we degraded the nominally 5 km resolution data to 30 km; Fig. 18a shows the result using 2 months of data (1440 images each between 30° *N* and 40° *S* by 130° east–west). The temporal statistics are shifted left–right on the log–log plot so that they coincide almost exactly with the east–west spatial statistics; this implies that the spatial statistics are identical to temporal statistics if time is transformed into space with a velocity of ≈900 km/day (≈10 m/s) which is nearly the same as that determined using space–time spectra (9.3 m/s; the same data, Section 4.2.3) and which is similar to that determined earlier from the mean energy flux and from the lidar space–time diagramme.

We can now use the normalized flux moments to determine the space–time diagramme, here the Δz, Δt relation is determined by $M_q(\Delta t) = M_q(\Delta z)$ where M_q is the normlized q^{th} order moment. Note that in principle, we could obtain a different space–time relation for low and high order moments q (corresponding to different relations for weak and intense events/structures). However inspection of Fig. 18a shows that since the time and space moments for all q are very similar, that there will be only very small

Please cite this article as: Lovejoy, S., Schertzer, D., Towards a new synthesis for atmospheric dynamics: Space–time cascades, Atmos. Res. (2010), doi:10.1016/j.atmosres.2010.01.004

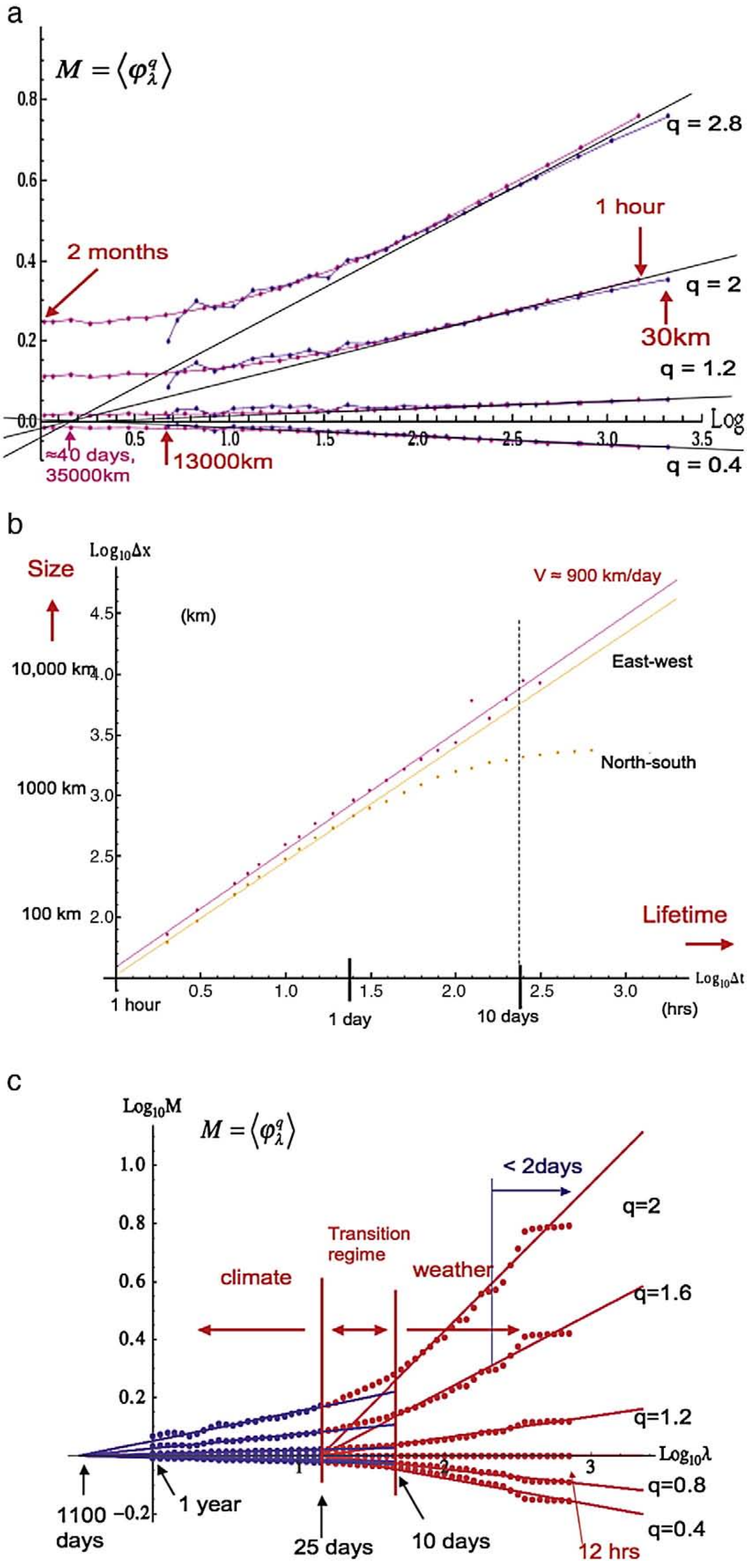

Please cite this article as: Lovejoy, S., Schertzer, D., Towards a new synthesis for atmospheric dynamics: Space–time cascades, Atmos. Res. (2010), doi:10.1016/j.atmosres.2010.01.004
]

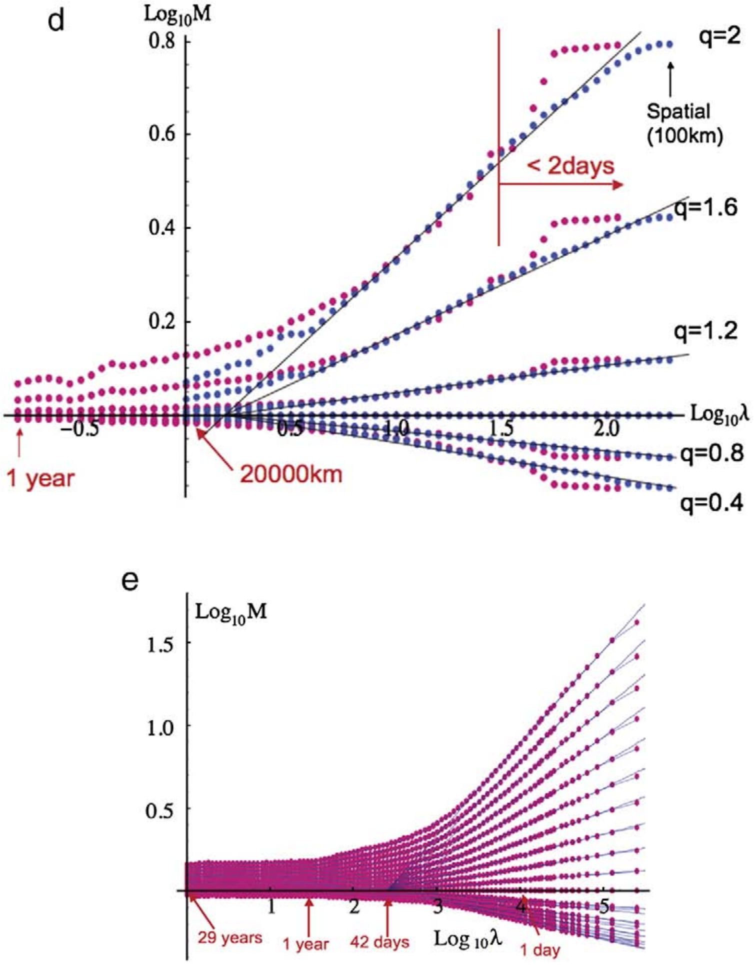

Fig. 18. a: An intercomparison of $\log_{10}M_q(\Delta t)$ for east west radiance fluxes (blue) and time (pink) for $q = 0.4$, 1.2, 2, 2.8. λ is defined with respect to a time scale of 2 months for the temporal analyses. The spatial $\log_{10}M_q(\Delta x)$ has been shifted so as to superpose as closely as possible on the $\log_{10}M_q(\Delta t)$ curves. The corresponding speed is ≈900 km/day (10 m/s) and the outer cascade scale is ≈40 days in time, ≈35,000 km in space. The deviations from scaling become important at about ≈5000 km or about ≈6 days. Compare this with the nearly perfectly scaling Fig. 7f which is the mean of the east west above with the north–south analysis (from Pinel, in preparation). b: The horizontal space–time diagramme constructed from panel a (red) and the corresponding diagramme from the north–south M_q (orange, from Pinel, in preparation). c: The normalized moments of the TRMM thermal IR data averaged over 100 × 100 km pixels at 12 hour resolution from 5300 orbits (1 year corresponding to $\lambda = 1$). The long time variability has been fit to a cascade with outer scale at 1100 days, but it is not clear that this is a good model (see Section 4.4). We thank V. Allaire for the help with this analysis. d: The same normalized moments of the TRMM thermal IR data as Fig. 18a but with temporal and spatial moments superposed corresponding to a velocity of 400 km/day. The pink is the temporal analysis (from Fig. 18c), the blue is the east–west spatial analysis (corresponding to Fig. 7d except that the analysis is not along orbit, and is at lower resolution). We thank V. Allaire for the help with this analysis. e: CPC hourly precipitation, 29 years (254,040 points in each series, 21 × 13 series over continental US, see Section 2.3.1). $C_1 = 0.37$, outer scale = 42 days.

differences, Fig. 18b shows the corresponding space–time diagramme. Comparing this with the mean east–west/north–south statistics (Fig. 7f) we see that the latter is very similar to the TRMM thermal IR (at typically in the NE or NSW directions, i.e. at ≈45° to the equator); it has excellent scaling. However, taken individually the north–south and east–west scalings are not so good at the largest scales, but nevertheless, time and (east–west) space are virtually identical including the deviations from scaling at large scales. The result is that the east–west space–time diagramme is nearly perfectly scaling over the entire range.

4.3.2. TRMM thermal IR

Returning to the TRMM data at a 12 hour resolution we averaged one year (≈5300 orbits) of the thermal IR over 100X100 km grids. The results are shown in Fig. 18a. Note that the below 2 days the statistics are poor since only a fraction of the 100X100 “pixels” are visited at time intervals less than this. We see that the plot can be divided into three regions. Up to about 10 days, the moments are relatively linear as expected from space–time multiplicative cascade processes. If we extrapolate the lines to larger scales, they cross at about 25 days; the variability at less than 10 days is accurately that which would result from multiplicative cascade starting at 25 days. At scales larger than this they have yet another behaviour which we discuss later. To aid in the interpretation, Fig. 18b shows the superposition of the east–west spatial analysis of the same data. We see that although the resolution is much lower and hence the scaling region much shorter — that up to about 10,000 km and 10–

Please cite this article as: Lovejoy, S., Schertzer, D., Towards a new synthesis for atmospheric dynamics: Space–time cascades, Atmos. Res. (2010), doi:10.1016/j.atmosres.2010.01.004

15 days, the fit is comparable to that of the MTSAT although the velocity is somewhat smaller, ≈400 km/day. According to our theoretical discussion about space–time statistics in anisotropic turbulence, it is natural to identify the scales where the space–time relation is linear with the weather, and those at scales larger than the outer temporal cascade scale

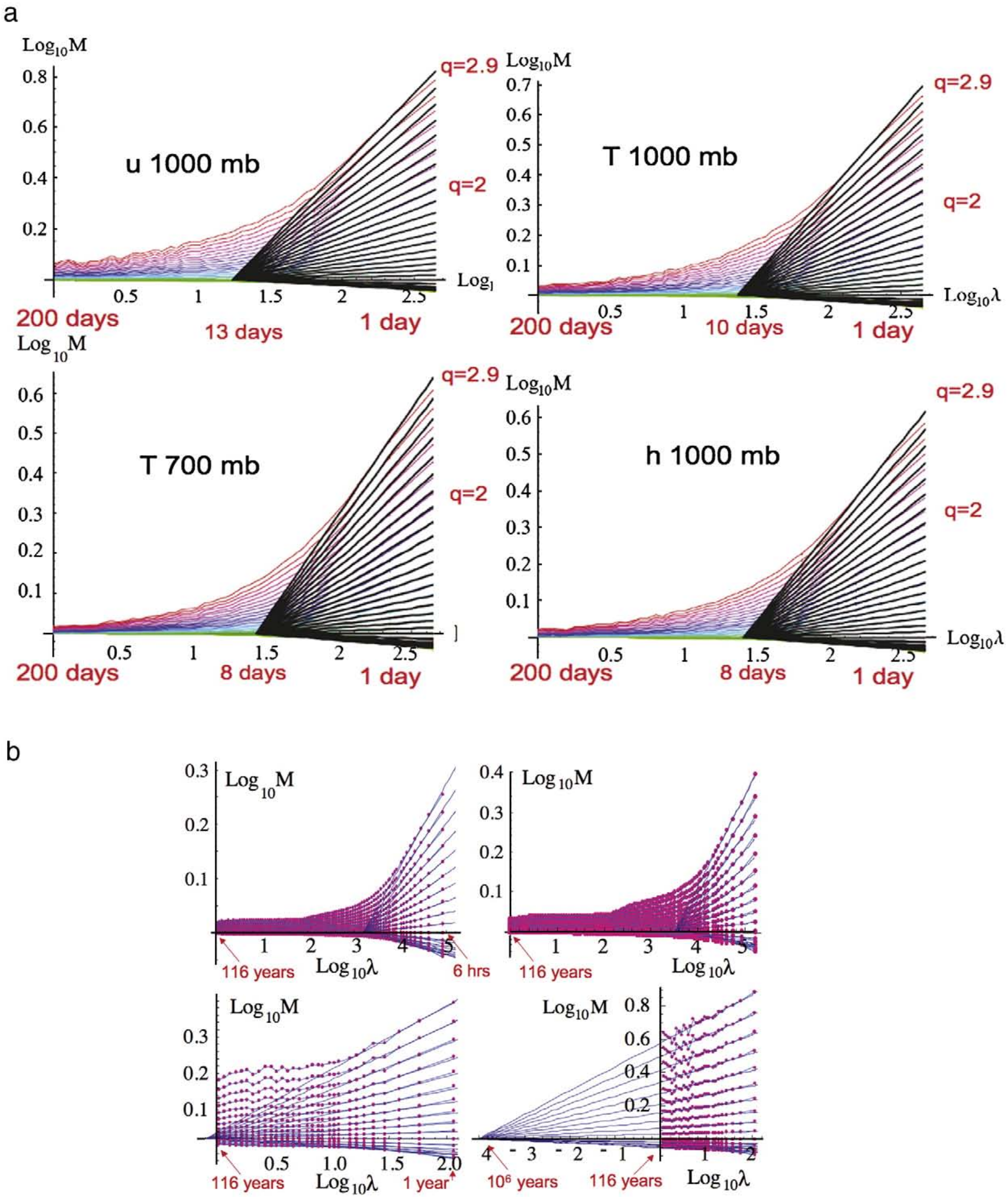

Fig. 19. a: These are the temporal cascades estimated from the GEM data, every 6 h, temporal (second derivative) flux estimates. Reproduced from Stolle et al. (submitted for publication). b: Temporal cascades in the 20th century reanalysis. This is the temporal companion to Fig. 6a. The top row shows the analysis of the Laplacian estimate of the flux at "weather scales" (resolution 1 day for the 700 mb zonal wind (u), left and 6 h for the surface pressure (right), both shown for 42°N, averaged over all longitudes). The parameters are: $C_1 = 0.085$, outer scale = 27 days, $C_1 = 0.11$, outer scale = 16 days respectively. The bottom shows the corresponding analysis of the temporal (second) fluctuation but of annually averaged Laplacians. The pressure shows some evidence of long range climate variations. The parameters are: $C_1 = 0.08$, outer scale = 150 yrs, $C_1 = 0.061$, outer scale ≈ 10^6 yrs respectively.

with the climate, with an intermediate “transition” region between the two; we return to this in Section 4.4.

4.3.3. Hourly precipitation

In Section 2.3.1 we already discussed the spatial cascades displayed by NOAA's CPC hourly US precipitation product up to scales of ≈4000 km (Fig. 7b). This data set is perhaps the highest time resolution set of its sort (254,040 points in each of 21x13 series) so that it is of interest to examine its temporal cascade structure, Fig. 18e shows the result. Note that the scaling was slightly improved by detrending the strong daily and annual cycles. Interestingly, C_1 was found to be a little lower (≈0.37) than for the corresponding spatial analyses — ($C_1 \approx 0.50$), and were more compatible with radar reflectivities (Z) using Z–R relations classical exponents $\beta \approx 1.6$; see the discussion in Section 2.3.1). The outer temporal cascade scale is 42 days compared with ≈32,000 km in space which implies a (reasonable) mean velocity of ≈760 km/day. However, this should be taken with caution since the spatial and temporal C_1's are somewhat different, so that either the space–time relation is nonlinear (so that a scale dependent velocity must be used), or the moments are affected by the poorly estimated low and zero rain rate statistics (or other artifacts of the data and the preprocessing to “homogenize” it onto a regular grid).

4.3.4. Temporal cascades in Numerical models

We can also perform scale by scale temporal analyses of the numerical model fluxes discussed in Section 2.2 and compare them with the corresponding spatial analyses. Fig. 19a shows typical results for the GEM (the full results are in (Stolle, 2009)). We see that it is very similar both qualitatively and quantitatively to the thermal IR, although with somewhat smaller external cascade scales (varying between 8 and 13 days). The best space–time transformations typically correspond to a velocities of ≈400–600 km/day which is comparable to that of the IR imagery. (Stolle, 2009) makes the comparable analyses for the ERA40 and GFS model and calculates many space–time diagrammes; the results are sufficiently similar that we do not repeat them here. Table 7 summarizes and compares the parameters for various fields showing only a weak latitude dependency and even little field to field variation in outer time scales or intermittency parameter C_1.

Because it is particularly long (116 years), we also show results from the 20th century reanalysis project, Fig. 19b. These are the same 700 mb zonal wind and surface pressure fields analyzed spatially in Fig. 6a, we show both analyses at “meteorological scales” (top row) and “climate scales” (annually averaged fields, bottom row). Considering the meteorological scales, we see the familiar cascades signature of converging straight lines (although here with slightly larger outer scales, 17, 26 days), and we note that after a year or so that the moments are nearly constant. If there were no more correlations, increasing the averaging scale would continue to smooth out, hence decrease the moments; this constancy indicates the presence of long range correlations. In the lower row at climate scales — analyzing a different (nontrivial!) flux — the Laplacian fluctuation of the annual mean fields — we see evidence for cascades at climate scales. The behaviour of the zonal wind is not clear: either the converging lines at the smaller time scales (those shown) indicate a cascade with outer scale of the order of a century, or — possibly more likely given the pressure cascade, lower right — it could simply represent convergence to a cascade with a much larger outer scale. In any event, the mere existence of near constant or linear regimes indicates the presence of long range statistical dependencies. In the next section, we back this up further by considering “Levy collapses” of the moments.

Table 7
Parameters characterizing the temporal cascade for the tropical (±30°) and the midlatitude (±45°) regions. Adapted from Stolle et al. (submitted for publication).

Field	α		C_1		T_{eff} (days)	
	±30°	±45°	±30°	±45°	±30°	±45°
u ERA40 1000 mb	1.8	1.7	0.14	0.15	38	48
h_s ERA40 700 mb	1.6	1.6	0.15	0.15	15	15
T GEM 1000 mb	1.8	1.8	0.14	0.14	17	18
T GEM 700 mb	2.0	2.0	0.12	0.13	42	34
u GFS 700 mb	1.7	1.7	0.13	0.13	30	25
h_r GFS 1000 mb	1.7	1.7	0.14	0.14	25	25

4.3.5. Levy collapse and universality

Up until now, we have primarily concentrated on establishing the fundamental prediction of multiplicative cascade models, Eq. (1). However, we also argued that there are basic physical, mathematical reasons (essentially the existence of a kind of multiplicative central limit theorem) that make it plausible that the model fields fall into special universality classes in which the basic scale invariant exponent $K(q)$ is given by Eq. (2) characterized by just two parameters C_1, α. In the analysis of spatial cascades (Stolle et al., submitted for publication), it was directly shown that universality works well — at least up to a critical moment q_c beyond which there is a “multifractal phase transition” where K becomes asymptotically linear (a sample size dependent effect corresponding to the domination of the statistics by the largest flux values present, (Schertzer et al., 1993)). If the flux follows Eq. (1) with K given by Eq. (2), it implies that the generator Γ of the cascade ($=\log \varphi$) is a Levy variable, index α. In that case, one can attempt to “collapse” the moments M_q to a unique curve by dividing log M_q by the theoretical $K(q)$ for (say) $C_1=1$, i.e. by dividing it by $(q^\alpha - q)/(\alpha-1)$; if M_q does indeed follow Eqs. (1) and (2) with parameters C_1, α, then we obtain $(\alpha-1)\ \log M_q/(q^\alpha - q) = C_1 \log\lambda$ which is independent of the moment q so that all the curves with different q values “collapse” onto a single curve whose slope is given by C_1. The interest of such plots goes beyond just testing for the universal cascade behaviour: on a single plot we can independently evaluate both the scaling (the straightness of the collapsed lines) as well as the log-Levy nature of the generator — by the thinness of the collection of lines i.e. how well at a given scale the different moments collapse, how well they follow the form $(q^\alpha - q)$. this is particularly interesting in the weather/climate transition region since a breakdown in Eq. (1) does not necessarily imply that the distribution is no longer log-Levy (see the next section), it need only retain a more general multiplicative structure. This means that the moment curves $(\alpha-1)\ \log M_q/(q^\alpha - q)$ can still “collapse” even if there is no longer scaling.

Please cite this article as: Lovejoy, S., Schertzer, D., Towards a new synthesis for atmospheric dynamics: Space–time cascades, Atmos. Res. (2010), doi:10.1016/j.atmosres.2010.01.004

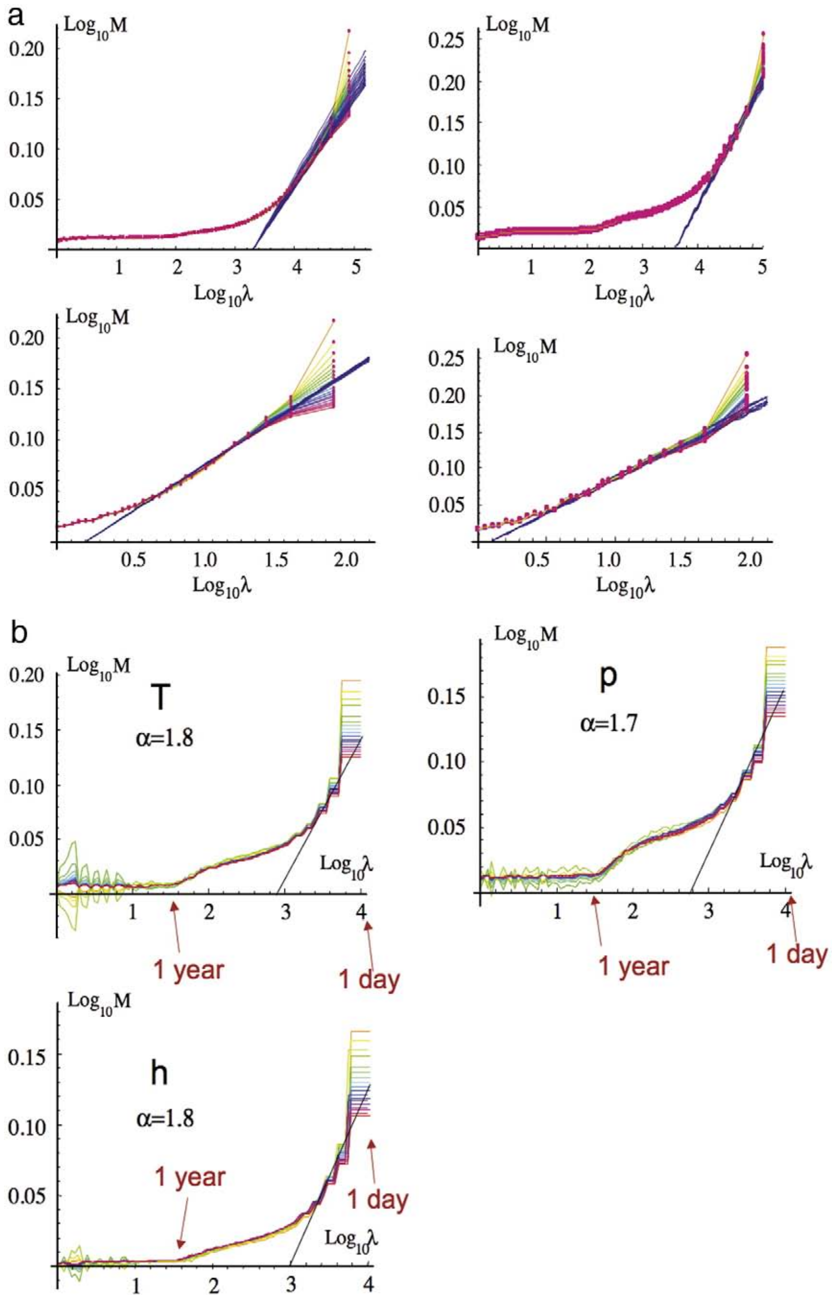

Fig. 20. a: These are the Levy collapses for the 700 mb zonal wind (left column) and surface pressure (right column) from the 20th century reanalysis, top in the time domain (6 hours resolution), bottom in the spatial domain. These are the collapses of the cascades shown in Figs. 6a and 19b. The α for the collapse (to the nearest 0.1) and the C_1 values corresponding to the linear (cascade regime) are: (1.9, 0.090), (1.9, 0.085) (zonal wind, time, space respectively, outer scales 21 days and 12,600 km) and surface pressure, time, space (1.9, 0.11), (1.9, 0.10), outer scales 10 *days* and 15,800 km. b: These are Levy collapses of the analyses of US daily station data discussed in Section 4.1.3 (Fig. 16c, d, e), series 12,400 days long (≈34 years, 1975–2008; the series were shorter and hence more numerous set of stations were used to get the best statistics), moments up to $q = 3.8$ were used. The number of stations used were: pressure (18 stations), temperature (158 stations) humidity (84 stations), the collapses used the Greek α values shown.

In Fig. 20a we see that the collapse for the 20th century reanalyses is excellent, and this out to scales way into the "climatological" regime (typically the spread of the collapsed curves about the mean is 2–10 percent of the mean, comparable to that in found in spatial analyses, see Stolle et al., submitted for publication) for other examples. Note that the largest deviations are at the very smallest scales (largest octave in λ) due to the "finite size" effects mentioned earlier, and at the very largest scales (smallest λ) where the statistics are poor. The apparent Log–Levy nature of the fluxes even at very long time scales is significant and hints at a deep relationship between weather and climate processes. These conclusions are supported by analysis of the daily station data for T, p, h shown in Fig. 20b. Although the statistics are much poorer than those of the 20th century reanalysis — leading to visible statistical fluctuations at the longer time scales — they nevertheless support the Log–Levy (hence presumably multiplicative) character of the fluxes out to scales of a year or more. In Section 4.4 we discuss a simple weather/climate model which roughly reproduces this behaviour.

4.4. The climate as a dimensional transition from the weather: extending the cascade model to long time periods

4.4.1. Discussion

Considering just the horizontal and time domains, we have argued that the velocity scale linking time and space should be precisely the typical velocity of the largest eddy V which is determined by the external spatial scale L (the size of the planet) and the driving global mean energy flux ε_L (itself determined by the solar radiation modulated by the clouds and dynamics; $V=\varepsilon_L^{1/3}L^{1/3}$ and $T=L/V$). In other words, L, V, T are determined from basic principles, they are not simply adjustable model parameters. Considering the scale function for a planetary scale region with small overall mean velocity (but not small rms velocity V), we argued that for scales $l<L$ and $\tau<T$, it was essentially isotropic (Eq. (29), $G_{eff}=$the identity, trivial anisotropy only).

While we have spent effort testing the prediction of the basic model for scales $l<L$ and $\tau<T$, we have not examined the behaviour of the model for scales $\tau>T$. Can the same model account for the weather — climate transition, and to what extent can it account for the climate regime (e.g. the spectral plateau)? In other words, what are the limits of the model, at what scales does it finally break down?

As a step toward answering this question, we turn to explicit space–time stochastic cascade models. We now recall the basic features of (continuous in scale) cascade model for the turbulent flux ε. First, since it is assumed to be a multiplicative process, it can be expressed in terms of the exponential of an additive generator Γ:

$$\varepsilon\left(\underline{r},t\right) = \langle\varepsilon_L\rangle e^{\Gamma\left(\underline{r},t\right)} \tag{31}$$

where Γ is the (dimensionless) generator. If we assume that the basic statistics are translationally invariant in space–time (statistically homogeneous, statistically stationary), then G is given by a convolution between a basic noise $\gamma(\underline{r},t)$ (independent, identically distributed random variables), and $g(\underline{r},t)$ is a Green's function (a deterministic weighting function that correlates them over (potentially) large space–time distances):

$$\Gamma\left(\underline{r},t\right) = \gamma\left(\underline{r},t\right) * g\left(\underline{r},t\right) \tag{32}$$

For the stable and attractive processes leading to universal multifractals, $\gamma(\underline{r},t)$ is taken as a unit (and extremal) Levy noise, index α, i.e. whose second characteristic function is $\log\langle e^{\gamma q}\rangle = q^{\alpha}/(\alpha-1)$. In addition for universal multifractals, g must have a particular form:

$$g\left(\underline{r},t\right) = n_D C_1^{1/\alpha}\left[\!\left[\left(\underline{r},t\right)\right]\!\right]^{-D/\alpha} \tag{33}$$

with the singularity cutoff at the inner, dissipation scale and D the dimension of space time (= the trace of the scale generator G for isotropic space–time), n_D is a normalization constant, C_1 the intermittency parameter of the mean intermittency, α is the Levy index of the (extremal) uncorrelated space–time unit amplitude Levy noise $\gamma(\underline{r},t)$ (see (Schertzer and Lovejoy, 1987) for the basic model, (Marsan et al., 1996) for the extension to causal space–time processes, (Lovejoy et al., 2008b) for the extension to turbulence driven waves, and (Lovejoy and Schertzer, in press) for a technical treatment of numerical issues.

The observable v (e.g. a horizontal wind component) whose statistics obeys Eq. (20) can be obtained from the flux by taking:

$$v\left(\underline{r},t\right) = \varepsilon\left(\underline{r},t\right)^{1/3}L^{1/3} * \left[\!\left[\left(\underline{r},t\right)\right]\!\right]^{-(D-H)} \tag{34}$$

(the $L^{1/3}$ is needed since the scale function is nondimensional).

In Eqs. (33), (34), we have ignored the issue of causality which can be taken into account with the use of a Heaviside function in the convolutions (Marsan et al., 1996); for our present purposes, this complication will be ignored; Eq. (34) for the observable is called the "Fractionally Integrated Flux model".

4.4.2. A simple model of (x, t) sections of the weather, the transition and the climate

We will now consider the consequences of assuming that a multiplicative model of the type defined by Eqs. (30)–(33) holds for climate scales $\tau\gg T$. In order to understand the

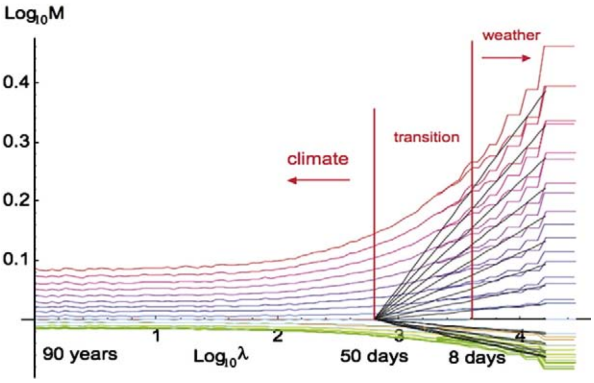

Fig. 21. The result of averaging over 12 realizations of the (x, t) section of the cascade weather–climate model on a $2^4\times2^{15}$ point grid (discussed in the text) with $C_1=0.1$, $\alpha=1.8$, $H=1/3$. The resolution is taken as 1 day in time, ≈1200 km in space (1/16 of T, 1/16 of L respectively, so that according to the analysis, the model temporal outer scale has been increased a bit with respect to the theoretical T). The curves are for the moments $q=0.1, 0.2, \ldots 1.9$, the spatial and temporal analyses are shown superposed.

Please cite this article as: Lovejoy, S., Schertzer, D., Towards a new synthesis for atmospheric dynamics: Space–time cascades, Atmos. Res. (2010), doi:10.1016/j.atmosres.2010.01.004

basic features of the weather, the transition and the climate we can study restrict our attention to a $D=2$, $(x-t)$ section of the full (x, y, z, t) model. The spectrum of such a model was shown in Fig. 15b, and in Fig. 21, we show the corresponding normalized moments. If we rewrite Eq. (31), Eq. (32) nondimensionalizing x with L and t with T, then we obtain for the generator $\Gamma(x,t)=\log(\varepsilon(x,t)/\langle\varepsilon_L\rangle)$:

$$\Gamma\left(\underline{r},t\right) = \int_{\Lambda_w^{-1}}^{1}\int_{\Lambda_w^{-1}}^{1}\gamma(\underline{r}-\underline{r}',t-t')g(\underline{r}',t')d\underline{r}'dt' + \int_1^{\Lambda_c}\int_{\Lambda_w^{-1}}^{1}\gamma\left(\underline{r}-\underline{r}',t-t'\right)g\left(\underline{r}',t'\right)d\underline{r}'dt' \qquad (35)$$

$\Lambda_w=L/L_i=T/T_i$ is the total range of meteorological scales $\Lambda_c=T_o>T$ is the overall outer scale of the weather/climate process. Denoting the first term by $\Gamma_w(x,t)$ "w" for "weather" and the second climate scale term $\Gamma_c(t)$ ("c" for "climate") then for $T_o>>T$, we have approximately:

$$\begin{aligned}\Gamma(x,t)&\approx\Gamma_w(x,t)+\Gamma_c(t)\\ \Gamma_w(x,t)&=\int_{S_{\Lambda_w}}\gamma\left(x-x',t-t'\right)g\left(x',t'\right)dx'dt'\\ \Gamma_c(t)&=\int_1^{\Lambda_c}\overline{\gamma}\left(t-t'\right)g\left(0,t'\right)dt'\end{aligned} \qquad (36)$$

where $\overline{\gamma}\left(t-t'\right)$ is a spatially integrated Levy noise and S_Λ is the quarter unit circle in (x,t) space with the quarter circle around the origin of radius Λ_w^{-1} removed (or squares: for our present purposes the difference is unimportant). The approximation in Eq. (36) consists in assuming $g(x,t)\approx g(0,t);\quad t>\;>x$ so that for long enough lags the spatial lags are unimportant. $\Gamma_w(x,t)$ is a 2D (space–time) integral corresponding to the contribution to the variability from the weather regime ($t<1$, $x<1$), and the second $\Gamma_c(x,t)$ is a 1D (purely) temporal contribution due to the climate regime. This drastic change of behaviour due to the change of space–time dimension over which the basic noise driving the system acts is a kind of "dimensional transition" between weather and climate processes.

In this simplest model it is only this separation into independent weather and climate terms with correlated noises integrated over spaces of different effective dimensions which is responsible for the statistical difference between weather and climate, at the level of the fluxes it means that the climate process modulates the weather process at the larger time scales:

$$\varepsilon_{\Lambda_{w,1^{-1}}}(x,t)\approx e^{\Gamma_w(x,t)+\Gamma_c(x,t)}=\varepsilon_{\Lambda_{w,1^{-1}}}(x,t)\varepsilon_{\Lambda_{w,1^{-1}}}(t) \qquad (37)$$

with $\varepsilon_{\Lambda_{w,1^{-1}}}(x,t)$, having the high frequency variability, $\varepsilon_{1,\Lambda_c}(t)$ the low frequency. The generic result is a "dimensional transition" in the form of a spectral plateau which we investigate in more detail in (Lovejoy and Schertzer, in preparation), see also Fig. 15b.

To understand the statistics of the model we can calculate the second characteristic functions of $\log\varepsilon$ $(=\log\langle e^{q\Gamma}\rangle)$; we can use the general formulae (valid of the i.i.d. Levy noise g and deterministic function and any positive function f):

$$f=\int\gamma(s)g(s)ds;\quad log\left\langle e^{fq}\right\rangle=\frac{q^\alpha}{\alpha-1}\int g^\alpha(s)ds \qquad (38)$$

We find:

$$\begin{aligned}\left\langle\varepsilon^q_{\Lambda_{w,1^{-1}}}\right\rangle&\approx e^{\frac{q^\alpha}{\alpha-1}\int_{S_\Lambda}^{1}g^\alpha\left(x',t'\right)dx'dt'}\\ \left\langle\varepsilon^q_{1,\Lambda_c}\right\rangle&\approx e^{\frac{q^\alpha}{\alpha-1}\int_1^{\Lambda_c/\Lambda}g^\alpha\left(0,t'\right)dt'}\end{aligned} \qquad (39)$$

To see how the weather term results in a multiscaling power law we use the scale function appropriate for a mean $<\underline{v}>\approx0$ but $<v^2>=V^2$, (Eq. (27)) and nondimensionalizing x, t we have:

$$\begin{aligned}g(x,t)&=n_DC_1^{1/\alpha}[\![(x,t)]\!]^{-D/\alpha}=n_DC_1^{1/\alpha}\left(x^2+t^2+t^3\right)^{-1/\alpha}\\ &\approx n_DC_1^{1/\alpha}\left(x^2+t^2\right)^{-1/\alpha};\qquad t<1\end{aligned} \qquad (40)$$

where we have used $D=2$ and (the cubic – pure time development term – is only significant near $t=1$). If we now use polar coordinates $r^2=x^2+t^2$, $dxdt=rdrd\theta$, we see that choosing $n_D=(\pi/2)^{-1/\alpha}$ the integral (over a quarter circle) in expression for ε_w yields the required log behaviour. In addition, normalizing ε_w by dividing by the mean so that $<\varepsilon_w>=1$, we obtain $\langle\varepsilon^q_{\Lambda w}\rangle\approx\Lambda_w{}^{K(q)}$ with $K(q)=C_1(q^\alpha-q)/(\alpha-1)$.

The key point about the weather–climate transition is thus the dimensional transition; the difference in the dimensions of space over which the integrals in the weather and climate terms of Eqs. (36), (39) are carried out. In order for the climate regime to display multiscaling, we require $g(0,t)\approx t^{-1/\alpha}$ for $t>1$ whereas the extrapolation of the weather $g(x,t)$ yields $g(0,t)\approx t^{-2/\alpha}$ which falls off too quickly. In other words, unless the weather noise becomes substantially more correlated (i.e. the exponent for g becomes lower for $t>1$) for the climate regime, the correlations will be relatively short ranged leading to the spectral-plateau white noise – like regime of Fig. 15.

In summary, this model predicts the following for the fluxes:

a) the flux statistics factorize into a weather and climate contribution:

$$\varepsilon(x,t)\approx e^{\Gamma_w(x,t)+\Gamma_c(x,t)}=\varepsilon_w(x,t)\varepsilon_c(t) \qquad (41)$$

with ε_w having the high frequency variability, ε_c the low frequency. The generic result is a "dimensional transition" in the form of a spectral plateau.

b) Since weighted sums of independent Levy variables are still Levy variables, this models predict that the climate variability $\varepsilon_c(t)$ (estimated by space–time averaging over the weather scales) has the same (Log Levy) form at time scales much larger than T. In other words, a prediction that follows simply from Eqs. (31), (32) (i.e. the multiplicative nature of the process), is that $[\log(\langle\varepsilon^q_\lambda\rangle/\langle\varepsilon_\lambda\rangle^q)]/K(q)\approx F(\lambda)$ where F is a function only of λ, not q. In Section 4.3.5 we have shown that this is apparently well verified both on daily in situ data and on reanalyses, in the latter case for scales up to 100 years (Fig. 19b). This is evidence that the multiplicative model applies at least to some climate scales.

c) If we consider an observable $v=\varepsilon*g$, then we again have a separation of the convolution into a space–time integral

Please cite this article as: Lovejoy, S., Schertzer, D., Towards a new synthesis for atmospheric dynamics: Space–time cascades, Atmos. Res. (2010), doi:10.1016/j.atmosres.2010.01.004

over the weather scales and (approximately) a time only integral for the climate scales, we again have a dimensional transition at T.

The model shows that at least some of the statistical features of the transitional and climate regimes — particularly the white noise like spectral plateau — are simply long time ($>T$) consequences of the same basic fluid physics that describes the weather regime at scales ($<T$). A future task is to see how far we can take the model before it breaks down (see the discussion in Section 4.1.3) and the relation of this to the stochastic linear forcing approach which is used in the "near climate" regime of weeks and months.

5. Conclusions

5.1. Outstanding issues

We have proposed a synthesis of state-of-the-art data and nonlinear theory which potentially unifies atmospheric dynamics over huge ranges of space–time scales. However, in many respects this picture is still tentative; below we list just a few of the outstanding scientific issues that it raises.

5.1.1. The relation between the phenomenological cascade model and the underlying dynamical equations

Although it would be satisfying to be able to rigorously derive the cascade model from the underlying dynamical equations, we should recall some history. The embarrassing fact is that in spite of intense efforts over more than 50 years, analytic approaches have been surprisingly ineffective at deducing the statistical properties of turbulence. The development of explicit multiplicative cascade models starting in the 1960's, was precisely an attempt to overcome the limitations of statistical closure, renormalization, and other kindred analytical techniques. Indeed, in understanding high Reynolds number turbulence (whether geophysical or otherwise), we are increasingly faced with two main alternatives: brute force numerics and phenomenological models, especially cascades.

While to our knowledge there have been no attempts to directly check the validity of multiplicative cascades (Eq. (4)) on either direct numerical simulations (DNS) or (until (Stolle et al., 2009)) on geophysical numerical simulations, there have been some relevant developments. The closest is perhaps the multifractal characterization of time signals in turbulent shell models (Biferale, 2003) or in "scaling cascade of gyroscopes" models (Chigirinskaya and Schertzer, 1996; Chigirinskaya et al., 1998). While the former discretizes the Navier Stokes equations in Fourier space while keeping a small and fixed number of degrees of freedom per octave in scale, the latter more realistically discretizes the equations on a dyadic tree structure such that the number of degrees of freedom increases with wavenumber. Other relevant connections between the cascade prediction, Eq. (4), and dynamical equations are the studies of temporal scaling (Syroka and Toumi, 2001; Blender and Fraedrich, 2003; Fraedrich and Blender, 2003), and temporal multifractality of climate models (Royer et al., 2008).

In spite of slow progress in reconciling the cascades with classical numerical models, the finding that atmospheric models accurately respect cascade structures over essentially their entire ranges will surely provide an impetus for resolving this basic issue.

5.1.2. The relevant fluxes: their physical nature

We have criticized the classical turbulence approach for deciding *a priori* which turbulent fluxes are relevant, and this coupled with additional *a priori* isotropy assumptions. Indeed, the (occasionally spectacular) confirmations of the predictions of cascades detailed throughout this review were possible because we only made use of the weaker assumption of scaling — which in any case we tested — and we did so without the need to assume in advance the physical nature of the fluxes.

We now need to investigate this further. On the one hand using high quality space–time remotely sensed data sets — or outputs from numerical models — we can use the classical techniques of turbulence theory to study fluxes in Fourier space i.e. the wavevector/frequency domain. Since the turbulent fluxes are Fourier space fluxes (e.g. large to small scale energy transfers), this is the natural framework for doing this. On the other hand, we must try and clarify the physical nature of the cascading fluxes, and eventually their inter-relations, including basic questions such as the number of different cascades and the nature of their inter-relations, inter-dependencies.

5.1.3. The robustness of the exponents

Anisotropic cascades involve two qualitatively different sets of exponents: the first characterize the change in the statistics of the fluctuations with scale, (H, C_1, α) the second, the exponents that define the notion of scale itself (G). Each is characterized by a (mathematical) group and its generator. From a theoretical point of view, the difficulty is that without knowing G, we can't rigorously define the scales and hence determine the statistical exponents H, C_1, α. The solution adopted in the empirical analyses was to take advantage of two rough empirical facts a) that in the horizontal, the anisotropy was not so strong: or at least not strong enough to prevent most of its effects being washed out by using isotropic analysis techniques (such as averaging over wave vector directions to obtain isotropic spectra), and b) that the vertical eigenvector of G is roughly perpendicular to the horizontal direction. These two properties allowed us to effectively avoid the very difficult estimation of off-diagonal elements of G ((Lewis et al., 1999); although the latter are presumably important for cloud and other morphologies).

Bearing in mind this need to "bootstrap" our analyses by first guessing an appropriate definition of scale (G, $\|(\underline{r},t)\|$), and then using it to estimate the statistics (H, C_1, α), we must then consider the robustness of the parameter estimates. This has two aspects: first there must be attempts at reproducing the existing exponent estimates with other instruments, other methodologies, different analysis techniques. This is especially true of in situ measurements which typically have nontrivial problems (Section 2). Second, we mentioned that there are already indications that there appear to be some systematic variation of exponents with altitude (especially the horizontal wind); and why not with latitude? In principle such spatial variations can be accounted for in a scaling cascade framework, but at the price of introducing a nonlinear generator G.

Please cite this article as: Lovejoy, S., Schertzer, D., Towards a new synthesis for atmospheric dynamics: Space–time cascades, Atmos. Res. (2010), doi:10.1016/j.atmosres.2010.01.004

5.1.4. Scale functions and stratification

The justification of generalized scale invariance is that one should not impose *a priori* notions of scale (such as isotropic metrics), one should rather allow them to be determined by the nonlinear dynamics; the appropriate scale notions are expected to be "emergent quantities" determined by the turbulent fluxes. This idea is similar to general relativity where the distribution of matter and energy determine the distance notion — the metric — although here the scale function need not be a metric. In the simplest model, there would be a single space–time scale function valid for all the atmospheric fields. Although this idea is seductive there are indications that things are more complicated; for example our inter-comparison of the empirical stratification parameter H_z (Table 6) suggests that there may be at least two scale functions needed — one for the humidity and passive scalars, and one for temperature, potential temperature and horizontal velocity.

The stratification issue could also be profitably studied with the help of numerical models of the atmosphere. At present, the models that have been examined (Section 2.2) are hydrostatic and the vertical statistics have not been fully investigated because in the vertical the model levels are so unevenly spaced that the statistics are difficult to interpret. However, preliminary investigations on the ECMWF interim reanalysis suggest that to within intermittency corrections, the vertical scaling of the horizontal wind has $H=1$ (i.e. it is statistically linear) and that the isobaric wind spectra are apparently different from the isoheight spectra. This is because of the scaling stratification of the wind combined with the small but non negligible slopes of the isobars. In addition, there are physically based (meteorological) correlations between the wind and pressure fields. At present it is therefore not clear that the numerical models are at all capable of reproducing the observed scaling stratification. However, due to the importance of stratification — and the acknowledged unsatisfactory nature of the hydrostatic approximation, it would be worth returning to vertical model analyses perhaps using nonhydrostatic models with more evenly spaced vertical levels.

5.1.5. The weather–climate transition and the limits of the model and stochastic linear modelling

We have given evidence that the cascade picture extends up to planetary scales and to time scales of a week or more. We have argued that the observed weather–climate transition is in fact a generic consequence of the basic multiplicative cascade model; that it follows because at long time scales, the spatial correlations are essentially cut-off by the finite size of the earth. We even gave evidence that at least into the beginning of the climate range (beyond the scaling regime, even up to tens of years) that the model may still apply (Section 4.4). This would mean that at least up to these scales that in some respects, climate variability is still fundamentally of the same type as the weather variability. It is therefore important to determine its real temporal outer limits. The validity of the model — even over just part of the climate range — would be important in improving our understanding of natural climate variability, of SLF type linear stochastic modelling, and our ability to discern anthropogenic effects.

5.2. Applications

Atmospheric science labors under the misapprehension that its basic science issues have long been settled and that its task is limited to the application of known laws — albeit helped by ever larger quantities of data themselves processed in ever more powerful computers and exploiting ever more sophisticated algorithms. Atmospheric science is thus increasingly being reduced to the application of techniques, to the development of "products". We have already argued that a consequence of its undervalued theoretical component is the failure to profit from the technological manna itself to reach a consensus on the atmosphere's basic scale by scale properties. Unfortunately in many areas we have reached the point where even the expenditure of vast resources on urgent applications have been (and will continue to be) inadequate for overcoming longstanding problems, precisely because often these problems are linked to issues of extreme variability, heterogeneity and space–time resolution.

Conversely, if the cascade synthesis is even approximately correct, it will open up new vistas for applications, many of which are of as yet difficult to discern. Below we list a few of the more immediate ones.

5.2.1. The development of resolution independent remote sensing algorithms, resolution independent objective analyses

The empirical analyses summarized in earlier sections directly demonstrate the strong scale dependencies of many atmospheric fields, showing that they depend in a power law manner on the space–time scales over which they are measured. While remotely sensed fields are radiances — in themselves usually of limited interest — they are often used to determine surrogates for dynamic and thermodynamic fields (e.g. satellite "products"). Well-known examples include radar estimates of rain rates or passive microwave estimates of temperature and humidity profiles. In many cases, considerable effort is exerted to calibrate ("validate") algorithms using in situ data. This leads to two resolution dependent difficulties: first that the space–time resolution of the calibration data is not equivalent to those of the radiances, and second that even if the radiance based surrogate is well calibrated at the calibration scale, this may not be true at any other scale. Yet there is typically nothing special about the surrogate resolution beyond the fact that it is the best available with existing technology; it is essentially a subjective limitation. A typical symptom of this implicit resolution problem is that when new satellites with improved resolutions become available, that the (sometimes numerous) algorithm/calibration constants have to seriously revised.

On the contrary, if we use the space–time scaling exponents to characterize the resolution dependencies, then these can be used as the basis for developing new scale/resolution invariant techniques (Lovejoy et al., 2001), possibly including resolution-independent Bayesian techniques. As an example, estimates of the earth's radiation budget should be revisited taking into account the cascade scaling of the radiances discussed in Section 2.3. The failure of current

Please cite this article as: Lovejoy, S., Schertzer, D., Towards a new synthesis for atmospheric dynamics: Space–time cascades, Atmos. Res. (2010), doi:10.1016/j.atmosres.2010.01.004

energy budget estimates to take these strong resolution dependencies into account implies the likely presence of biases.

5.2.2. Stochastic Forecasting, stochastic parametrisation

In the introduction, we mentioned the ongoing ensemble forecasting revolution, the fact that today meteorologists' goal is increasingly a stochastic one: to predict the possible states of the atmosphere as well as their corresponding probabilities of occurrence. However, the current ensemble forecasting technique is essentially a stochastic — deterministic hybrid which is indirect and problematic on several counts. The main difficulties are a) that it is based on a deterministic framework for the initial objective analysis — which uses statistics only to describe measurement errors — and not the fields themselves — and b) which assumes that the fields evolve according to deterministic nonlinear partial differential equations. While deterministic assumptions may be appropriate for descriptions and models at the dissipation scale, stochastic ones are more appropriate at lower space–time resolutions (if only because an infinite number of different dissipation scale fields give rise to the same low resolution analysis fields). The reason that ensemble forecasts are ultimately stochastic is that one attempts to deduce an initial probability distribution of atmospheric states at $t = 0$ ("ensemble breeding"), and then the model maps this initial distribution onto a future distribution. In this approach, even the final step — the analysis of the members of the forecast ensemble is nontrivial.

In contrast, cascades have the important advantage of (potentially) providing a consistent and natural stochastic initial distribution followed by an optimum stochastic forecast. First, the initial state of the atmosphere can be specified in terms of probabilities conditioned by the observations (at the appropriate space–time resolutions). They can then (in principle) take this initial conditional probability distribution and give the (theoretically optimum) stochastic forecast, i.e. the conditional expectations or conditional probabilities of the fields at future times, and this at whatever space–time resolutions are required (see e.g. Salvadori et al., 2001) for an attempt in this direction). While this purely stochastic forecast procedure has yet to be proven in practice, it has the additional advantage that it can in principle (statistically) take into account as wide a range of scales as necessary rather than the current 10^2–10^3. At present, its main limitations are that it has mostly been developed for handling individual scalar fields; generalizations are needed for vector cascades to describe the evolution of atmospheric state vectors (Schertzer and Lovejoy, 1995).

While pure stochastic forecasts are not likely any time soon (except perhaps for nowcasting, (Macor et al., 2007)), it should be soon possible to apply cascade models to "stochastic parametrisation" of the type introduced by (Buizza et al., 1999; Palmer, 2001b). Stochastic parametrisation is an attempt to increase the variability of the deterministic forecasts so as to increase the rate that the different members of the ensemble diverge from each other. It does this by introducing random numbers at each pixel, representing the random effect of the unmodeled sub grid scales. While at present this is done on a fairly ad hoc basis, the finding that the stochastic structure of the models can be described by cascades promises to put this on a more sound theoretical basis.

5.2.3. Distinguishing natural from anthropogenic variability and the problem of outliers

Conclusions about anthropogenic influences on the atmosphere can only be drawn with respect to the null hypothesis, i.e. one requires a theory of the natural variability, including knowledge of the probabilities of the extremes at various resolutions. At present, the null hypotheses are classical so that they assume there are no long range statistical dependencies and that the probabilities are thin-tailed (i.e. exponential). However we have seen that cascades involve long range dependencies and (typically) have fat tailed (algebraic) distributions in which extreme events occur much more frequently and can persist for much longer than classical theory would allow. Indeed, the problem of statistical "outliers" may generally be a consequence of the failure of highly variable cascade data to fit into relatively homogeneous, regular, classical geostatistical frameworks.

5.3. Perspectives

In this paper, we have given an overview of a body of work carried out over the last 25 years aiming at a scale by scale understanding of the space–time statistical structure of the atmosphere and its models. The new synthesis we propose would not be possible without technologically driven revolutions in both data quantity and quality as well as in numerical modeling and data processing. Also key for this synthesis are advances in our understanding of nonlinear dynamics (especially cascades, multifractals, and their anisotropic extensions), and in the corresponding data analysis techniques. Although there are many gaps to fill, it is remarkable that a relatively simple picture of the atmosphere as a system of interacting anisotropic cascades seems to be consistent with some of the largest and highest quality satellite, lidar, drop sonde and aircraft campaigns to date collectively measuring passive and active radiances over the long and short wave regimes, as well as in situ wind, temperature, humidity, potential temperature, pressure and other variables. It also holds remarkably well for reanalyses and other numerical models of the atmosphere. It leads to a natural distinction between the weather and climate and successively predicts the transition to the climate at ≈10 days as a dimensional transition from a weather system (where both long range space and time correlations are important) to a climate system dominated by long range temporal correlations.

At first sight, it may seem surprising that this essentially phenomenological model works so well. However, it is basically a generalization of the most successful laws of classical turbulence, those of Kolmogorov, Obukhov, Corrsin and Bolgiano and it is based three basic features of the governing equations: the scale invariance of the nonlinear terms, the existence of scale by scale conserved fluxes, and the fact that interactions are strongest among structures with similar sizes. The key points of the generalization are to anisotropy so that the finite scale thickness of the atmosphere need not break the horizontal scaling, and to intermittency to account for the extraordinary variability of the atmosphere explained in this picture as a

Please cite this article as: Lovejoy, S., Schertzer, D., Towards a new synthesis for atmospheric dynamics: Space–time cascades, Atmos. Res. (2010), doi:10.1016/j.atmosres.2010.01.004

consequence of the wide range of scales over which the variability builds up.

Although taken individually different parts of the picture presented here can (and must) be criticized. However, given the coherence of all the pieces and the fact that the synthesis is based on fundamental symmetries, we feel it is a promising paradigm for unifying atmospheric dynamics. In any case, some coherent picture is urgently needed to replace the aging and untenable (but still dominant!) 2D isotropic/3D isotropic turbulence model. We are confident that the challenge of improving or replacing this new synthesis will help atmospheric science forward during a period where scientific understanding has all too often been sacrificed for operational expediency.

Acknowledgements

We would like to thank John Snow for encouraging us to undertake this mini review. We also thank J. Stolle and C. Penland for the helpful comments. Lovejoy acknowledges NSERC for discovery grants although most of the work described here was unfunded.

References

Ashkenazy, Y., Baker, D., Gildor, H., Havlin, S., 2003. Nonlinearity and multifractality of climate change in the past 420,000 years. Geophys. Res. Lett. 30, 2146.

Bacmeister, J.T., et al., 1996. Stratospheric horizontal wavenumber spectra of winds, potnetial temperature, and atmospheric tracers observed by high-altitude aircraft. J. Geophys. Res. 101, 9441–9470.

Bak, P., Tang, C., Weiessenfeld, K., 1987. Self-Organized Criticality: An explanation of 1/f noise. Phys. Rev. Lett. 59, 381–384.

Balmino, G., 1993. The spectra of the topography of the Earth, Venus and Mars. Geophys. Res. Lett. 20 (11), 1063–1066.

Balmino, G., Lambeck, K., Kaula, W., 1973. A spherical harmonic analysis of the Earth's topography. J. Geophys. Res. 78 (2), 478–481.

Bartello, P., 1995. Geostrophic adjustment and inverse cascades in rotating stratified turbulence. J. Atmos. Sci. 52, 4410.

Bell, T.H., 1975. Statistical features of sea floor topography. Deep-Sea Res. 22, 883–891.

Blender, R., Fraedrich, K., 2003. Long time memory in global warming simulations. Geophys. Res. Lett. 30, 1769.

Boer, G.J., Shepherd, T.G., 1983. Large Scale two-dimensional turbulence in the atmosphere. J. Atmos. Sci. 40, 164–184.

Borde, R., Isaka, H., 1996. Radiative transfer in mulitfractal clouds. J. Geophys. Res. 101, 29,461–429,478.

Brunt, D., 1939. Physical and dynamical meteorology. Cambridge Univ Press, New York.

Buizza, R., Miller, M., Palmer, T.N., 1999. Stochastic representation of model uncertainties in the ECMWF Ensemble Prediction System. Quart. J. Roy. Meteor. Soc. 125, 2887–2908.

Charney, J.G., 1971. Geostrophic Turbulence. J. Atmos. Sci. 28, 1087.

Chen, T.-C., Wiin-Nielsen, A., 1978. Non-linear cascades of atmospheric energy and enstrophy in a two-dimensional spectral index. Tellus 30, 225–230.

Cho, J., Lindborg, E., 2001. Horizontal velocity structure functions in the upper troposphere and lower stratosphere i: Observations. J. Geophys. Res. 106, 10223–10232.

Compo, G., Whitaker, J.S., Sardeshmuhk, P., 2006. Feasibility of a 100-year reanlysis using only surface pressure data. Amer. Meteor. Soc. 175–190.

Compo, G.P., et al., in preparation. The Twentieth Century Reanalysis Project., Bull. Amer. Meteor. Soc.

Corrsin, S., 1951. On the spectrum of Isotropic Temperature Fluctuations in an isotropic Turbulence. J. Appl. Phys. 22, 469–473.

Davis, A., Lovejoy, S., Schertzer, D., 1993. Supercomputer simulation of radiative transfer inside multifractal cloud models. In: A.A., et al. (Ed.), International Radiation Symposium 92, Deepak, Hampton, Virginia, pp. 112–115.

Dewan, E., 1997. Saturated-cascade similtude theory of gravity wave sepctra. J. Geophys. Res. 102, 29799–29817.

Dewan, E., Good, R., 1986. Saturation and the "universal" spectrum vertical profiles of horizontal scalar winds in the stratosphere. J. Geophys. Res. 91, 2742.

Doswell III, C.A, Lasher-Trapp, S., 1997. On Measuring the Degree of Irregularity in an Observing Network. J. Atmos. Ocean. Technol. 14, 120–132.

Fox, C.G., Hayes, D.E., 1985. Quantitative methods for analyzing the roughness of the seafloor. Rev. Geophys. 23, 1–48.

Gage, K.S., Nastrom, G.D., 1986. Theoretical Interpretation of atmospheric wavenumber spectra of wind and temperature observed by commercial aircraft during GASP. J. Atmos. Sci. 43, 729–740.

Gagnon, J.S., Lovejoy, S., Schertzer, D., 2006. Multifractal earth topography. Nonlin. Proc. Geophys. 13, 541–570.

Gao, X., Meriwether, J.W., 1998. Mesoscale spectral analysis of in situ horizontal and vertical wind measurements at 6 km. J. Geophys. Res. 103, 6397–6404.

Gardner, C., 1994. Diffusive filtering theory of gravity wave spectra in the atmosphere. J. Geophys. Res. 99, 20601.

Gardner, C.S., Hostetler, C.A., Franke, S.J., 1993. Gravity Wave models for the horizontal wave number spectra of atmospheric velocity and density flucutations. J. Geophys. Res. 98, 1035–1049.

Gibert, D., Courtillot, V., 1987. Seasat altimetry and the South Atlantic geoid 1. Spectral analysis. J. Geophys. Res. 92 (B7), 6235–6248.

Gifford, F.A., 1988. A similarity theory of the tropospheric turbulence energy spectrum. J. Atmos. Sci. 45, 1370–1379.

Giordano, F., Ortosecco, I., Tramontana, L., 2006. Fractal structure of marine measuring networks. Il Nuovo Cimento C 02512177–02512182. doi:10.1007/BF02512018.

Halsey, T.C., Jensen, M.H., Kadanoff, L.P., Procaccia, I., Shraiman, B., 1986. Fractal measures and their singularities: the characterization of strange sets. Phys. Rev. A 33, 1141–1151.

Hamilton, K., Takahashi, Y.O., Ohfuchi, W., 2008. Mesoscale spectrum of atmopsheric motions investigated in a very fine resolution global general ciruculation model. J. Geophys. Res. 113, D18110. doi:10.11029/12008JD009785.

Hasselmann, K., 1976. Stochastic Climate models, part I: Theory. Tellus 28, 474–485.

Hendon, H.H., Wheeler, M., 2008. Some space-time spectral analyses of tropical convection and planetary waves. J. Atmos. Sci. 65, 2936–2948.

Higgins, R.W., Shi, W., Yarosh, E., Joyce, R., 2000. Improved United States Precipitation Quality Control System and Analysis. NCEP/Climate Prediction Center ATLAS Camp Springs, MD 20746, USA, p. 40.

Hock, T., Franklin, J., 1999. The NCAR GPS Dropsonde. Bull. AMS 407.

Högström, U., Smedman, A.N., Bergström, H., 1999. A Case Study Of Two-Dimensional Stratified Turbulence. J. Atmos. Sci. 56, 959–976.

Hovde, S.J., Tuck, A.F., Lovejoy, S., Schertzer, D., 2009. Vertical Scaling of the Atmosphere: Dropsondes from 13 km to the Surface. Quart. J. Roy. Meteor. Soc.

Huybers, P., Curry, W., 2006. LInks between annual, Milankovitch and continuum temperature variability. Nature 441, 329–332.

Julian, P.R., Washington, W.M., Hembree, L., Ridley, C., 1970. On the spectral distribuiton of large-scale atmospheric energy. J. Atmos. Sci. 376–387.

Kalnay, E., 2003. Atmospheric Modelling, Data Assimilation and Predictability. Cambridge University Press, Cambridge.

Kolesnikov, V.N., Monin, A.S., 1965. Spectra of meteorological field fluctuations. Izvestiya, Atmos. Ocean. Phys. 1, 653–669.

Korvin, G., Boyd, D.M., O'Dowd, R., 1990. Fractal characterization of the South Australian gravity station network. Geophys. J. Int. 100, 535–539.

Koscielny-Bunde, E., et al., 1998. Indication of a universal persistence law governing atmospheric variability. Phys. Rev. Lett. 81, 729.

Kraichnan, R.H., 1967. Inertial ranges in two-dimensional turbulence. Phys. Fluids 10, 1417–1423.

Ladoy, P., Lovejoy, S., Schertzer, D., 1991. Extreme Variability of climatological data: Scaling and Intermittency. In: Schertzer, D., Lovejoy, S. (Eds.), Non-linear variability in geophysics: Scaling and Fractals. Kluwer, pp. 241–250.

Landahl, M.T., Mollo-Christensen, E., 1986. Turbulence and random processes in fluid mechanics. Cambridge University press, Cambridge. 154 pp.

Lavallée, D., Lovejoy, S., Schertzer, D., Ladoy, P., 1993. Nonlinear variability and landscape topography: analysis and simulation. In: De Cola, L., Lam, N. (Eds.), Fractals in geography. Prentice-Hall, Englewood, N.J., pp. 171–205.

Leith, C.E., 1968. Diffusion approximation for two-dimensional turbulence. Phys. Fluids 11, 671–673.

Lewis, G., Lovejoy, S., Schertzer, D., Pecknold, S., 1999. The Scale Invariant Generator Technique for parameter estimates in Generalized Scale Invariance. Comput. Geosci. 25, 963–978.

Lilley, M., Lovejoy, S., Strawbridge, K., Schertzer, D., 2004. 23/9 dimensional anisotropic scaling of passive admixtures using lidar aerosol data. Phys. Rev. E 70, 036307-036301-036307.

Lilley, M., Lovejoy, S., Schertzer, D., Strawbridge, K.B., Radkevitch, A., 2008. Scaling turbulent atmospheric stratification, Part II: empirical study of the the stratification of the intermittency. Quart. J. Roy. Meteor. Soc. doi:10.1002/qj.1202.

Lilly, D.K., 1983. Stratified turbulence and the mesoscale variability of the atmopshere. J. Atmos. Sci. 40, 749–761.

Lilly, D.K., 1986a. The structure, energetics and propagation of rotating convective storms. Part I: Energy exchange with the mean flow. J. Atmos. Sci. 43, 113–125.

Lilly, D.K., 1986b. The structure, Energetics and Propagation of Rotating Convective Storms. Part II: Helicity and Storm Stabilization. J. Atmos. Sci. 43, 126–140.

Lilly, D.K., 1989. Two-dimensional turbulence generated by energy sources at two scales. J. Atmos. Sci. 46, 2026–2030.

Lindborg, E., Cho, J., 2001. Horizontal velocity structure functions in the upper troposphere and lower stratosphere ii. Theoretical considerations. J. Geophys. Res. 106, 10233–10241.

Lorenz, E.N., 1969. The predictability of a flow which possesses many scales of motion. Tellus 21, 289–307.

Lovejoy, S., Schertzer, D., 1986. Scale invariance in climatological temperatures and the spectral plateau. Annal. Geophys. 4B, 401–410.

Lovejoy, S., Schertzer, D., 1995. Multifractals and Rain. In: Kunzewicz, Z.W. (Ed.), New Uncertainty Conceps in Hydrology and Water Ressources. Cambridge University Press, pp. 62–103.

Lovejoy, S., Schertzer, D., 2006. Multifractals, cloud radiances and rain. J. Hydrol. doi:10.1016/j.hydrol.2005.02.042.

Lovejoy, S., Schertzer, D., 2007. Scale, scaling and multifractals in geophysics: twenty years on. In: J.E., Tsonis, A.A. (Eds.), Nonlinear dynamics in geophysics. Elsevier.

Lovejoy, S., Schertzer, D., in press. On the simulation of continuous in scale universal multifractals, part I: spatially continuous processes. Comput. Geosci.

Lovejoy, S., Schertzer, D. in preparation. The weather - climate transition, Nonlin. Proc. Geophys.

Lovejoy, S., Schertzer, D., Ladoy, P., 1986. Fractal characterisation of inhomogeneous measuring networks. Nature 319, 43–44.

Lovejoy, S., Gabriel, P., Davis, A., Schertzer, D., Austin, G.L., 1990. Discrete Angle Radiative Transfer, Part I: scaling and similarity, universality and diffusion. J. Geophys. Res. 95, 11699–11715.

Lovejoy, S., Schertzer, D., Tessier, Y., 2001. Multifractals and Resolution independent remote sensing algorithms: the example of ocean colour. Inter. J. of Remote Sensing 22, 1191–1234.

Lovejoy, S., Schertzer, D., Tuck, A.F., 2004. Fractal aircraft trajectories and nonclassical turbulent exponents. Phys. Rev. E 70, 036306-036301-036305.

Lovejoy, S., Tuck, A.F., Hovde, S.J., Schertzer, D., 2007. Is isotropic turbulence relevant in the atmosphere? Geophys. Res. Lett. L14802. doi:10.1029/2007GL029359.

Lovejoy, S., Schertzer, D., Allaire, V., 2008a. The remarkable wide range scaling of TRMM precipitation. Atmos. Res. doi:10.1016/j.atmosres.2008.02.016.

Lovejoy, S., Schertzer, D., Lilley, M., Strawbridge, K.B., Radkevitch, A., 2008b. Scaling turbulent atmospheric stratification, Part I: turbulence and waves. Quart. J. Roy. Meteor. Soc. doi:10.1002/qj.1201.

Lovejoy, S., Tuck, A.F., Hovde, S.J., Schertzer, D., 2008c. Do stable atmospheric layers exist? Geophys. Res. Lett. 35, L01802. doi:01810.01029/02007GL032122.

Lovejoy, S., Schertzer, D., Allaire, V., Bourgeois, T., King, S., Pinel, J., Stolle, J., 2009a. Atmospheric complexity or scale by scale simplicity? Geophys. Res. Lett. 36, L01801. doi:10.1029/2008GL035863.

Lovejoy, S., Tuck, A.F., Hovde, S.J., Schertzer, D., 2009b. The vertical cascade structure of the atmosphere and multifractal drop sonde outages. J. Geophys. Res. 114, D07111. doi:07110.01029/02008JD010651.

Lovejoy, S., Tuck, A.F., Schertzer, D., Hovde, S.J., 2009c. Reinterpreting aircraft measurements in anisotropic scaling turbulence. Atmos. Chem. Phys. Discuss. 9, 3871–3920.

Lovejoy, S., Watson, B., Grosdidier, Y., Schertzer, D., 2009d. Scattering in Thick Multifractal Clouds, Part II: Multiple Scattering, 388, pp. 3711-3727.

Lovejoy, S., Tuck, A.F., Schertzer, D., 2009e. Interactive comment on "Comment on "Reinterpreting aircraft measurements in anisotropic scaling turbulence" by Lovejoy et al/ (2009)" by E. Lindborg et al. Atmos. Chem. Phys. Disc. 9, C7688–C7699.

Lovejoy, S., Tuck, A., Schertzer, D., 2010. The Horizontal cascade structure of atmospheric fields determined from aircraft data, J. Geophys. Res. doi:10.1029/2009JD013353.

Macor, J., Schertzer, D., Lovejoy, S., 2007. Multifractal methods applied to rain forecast using radar data | [Méthodes multifractales appliquées à la prévision de pluie en utilisant des données radar]. Houille Blanche 4, 92–98.

Mandelbrot, B.B., 1974. Intermittent turbulence in self-similar cascades: divergence of high moments and dimension of the carrier. J. Fluid Mech. 62, 331–350.

Marsan, D., Schertzer, D., Lovejoy, S., 1996. Causal space-time multifractal processes: predictability and forecasting of rain fields. J. Geophys. Res. 31D, 26,333–326,346.

Mazzarella, A., Tranfaglia, G., 2000. Fractal Characterisation of Geophysical Measuring Networks and its Implication for an Optimal Location of Additional Stations: An Application to a Rain-Gauge Network. Theor. Appl. Climatol. 65, 157–163. doi:110.1007/s007040070040.

Meneveau, C., Sreenivasan, K.R., 1987. Simple multifractal cascade model for fully develop turbulence. Phys. Rev. Lett. 59, 1424–1427.

Monin, A.S., 1972. Weather forecasting as a problem in physics. MIT press, Boston Ma.

Monin, A.S., Yaglom, A.M., 1975. Statistical Fluid Mechanics. MIT press, Boston Ma.

Naud, C., Schertzer, D., Lovejoy, S., 1996. Fractional Integration and radiative transfer in multifractal atmospheres. In: Woyczynski, W., Molchansov, S. (Eds.), Stochastic Models in Geosystems. Springer-Verlag, New York, pp. 239–267.

Newman, M.P., Sardeshmuhk, P.D., Winkler, C.R., Whitaker, J.S., 2003. A study of subseasonal predictability. Mon. Weather Rev. 131, 1715–1732.

Ngan, K., Straub, D.N., Bartello, P., 2004. Three-dimensionalisation of freely-decaying two-dimensional flows. Phys. Fluids 16, 2918–2932.

Nicolis, C., 1993. Optimizing the global observational network - a dynamical-approach. J. Appl. Meteor. 32, 1751–1759.

Novikov, E.A., Stewart, R., 1964. Intermittency of turbulence and spectrum of fluctuations in energy-disspation. Izv. Akad. Nauk. SSSR. Ser. Geofiz. 3, 408–412.

N.R.C. Committee on Radiative Forcing Effects on Climate, 2005. Radiative Forcing of Climate Change: Expanding the Concept and Addressing Uncertainties. National Acad. press. 224 pp.

Obukhov, A., 1949. Structure of the temperature field in a turbulent flow. Izv. Akad. Nauk. SSSR. Ser. Geogr. I Geofiz 13, 55–69.

Palmén, E., 1959. In: Bolen, B. (Ed.), The atmosphere and the Sea in Motion. Oxford Univ, Press, pp. 212–224.

Palmer, T., 2001a. A nonlinear dynamical perspective on model error: a proposal for non-local stochastic-dynamic paramterisation in weather and climate prediction models. Quart. J. Roy. Meteor. Soc. 279–304.

Palmer, T., 2001b. Predicting uncertainty in numerical weather forecasts. In: Pierce, R.P. (Ed.), Meteorology at the Millenium. Royal Meteorological Society, pp. 3–13.

Panofsky, H.A., 1969. The spectrum of temperature. J. Radio Sci. 4, 1101–1109.

Pellieter, J.D., Turcotte, D., 1999. Self-Affine Time series II. Applications and models. Adv. Geophys. 40, 91–166.

Penland, C., 1996. A stochastic model of IndoPacific sea surface temperature anomalies. Physica D 98, 534–558.

Penland, C., Sareshmuhk, P.D., 1995. The optimal growth of tropical sea surface temperature anomalies. J. Climate 8, 1999–2024.

Pinel, J., in preparation. The space-time cascade structure of the atmosphere. Physics, McGill, Montreal.

Radkevitch, A., Lovejoy, S., Strawbridge, K., Schertzer, D., 2007. The elliptical dimension of space-time atmospheric stratification of passive admixtures using lidar data. Physica A. doi:10.1016/j.physa.2007.03.046.

Radkevitch, A., Lovejoy, S., Strawbridge, K.B., Schertzer, D., Lilley, M., 2008. Scaling turbulent atmospheric stratification, Part III: empIrical study of Space-time stratification of passive scalars using lidar data. Quart. J. Roy. Meteor. Soc. doi:10.1002/qj.1203.

Richardson, L.F., 1926. Atmospheric diffusion shown on a distance-neighbour graph. Proc. Roy. Soc. A110, 709–737.

Riehl, H., Malkus, J.S., 1958. ON the heat balance in the equatorial trough zone. Geophysica (Helsinki) 6, 503–538.

Rotunno, R., Snyder, C., 2008. A Generalization of Lorenz's Model for the Predictability of Flows with Many Scales of Motion. J. Atmos. Sci. 65.

Salvadori, G., Schertzer, D., Lovejoy, S., 2001. Multifractal objective analysis and interpolation, Stoch. Environ. Res. Risk Anal. 15, 261–283.

Sardeshmukh, P.D., Sura, P., 2009. Reconciling non-gaussian climate statistics with linear dynamics. J. Climate 22, 1193–1207.

Sardeshmuhk, P., Compo, G.P., Penland, C., 2000. Changes in probability assoicated with El Nino. J. Climate 13, 4268–4286.

Schertzer, D., Lovejoy, S., 1985a. Generalised scale invariance in turbulent phenomena. Phys.-Chem. Hydrodyn. J. 6, 623–635.

Schertzer, D., Lovejoy, S., 1985b. The dimension and intermittency of atmospheric dynamics. In: Launder, B. (Ed.), Turbulent Shear Flow 4. Springer-Verlag, pp. 7–33.

Schertzer, D., Lovejoy, S., 1987. Physical modeling and Analysis of Rain and Clouds by Anisotropic Scaling of Multiplicative Processes. J. Geophys. Res. 92, 9693–9714.

Schertzer, D., Lovejoy, S., 1995. From scalar cascades to Lie cascades: joint multifractal analysis of rain and cloud processes. In: Feddes, R.A. (Ed.), Space/time Variability and Interdependance for various hydrological processes. Cambridge University Press, New-York, pp. 153–173.

Please cite this article as: Lovejoy, S., Schertzer, D., Towards a new synthesis for atmospheric dynamics: Space–time cascades, Atmos. Res. (2010), doi:10.1016/j.atmosres.2010.01.004

Schertzer, D., Lovejoy, S., 1997. Universal Multifractals do Exist! Comments on "A statistical analysis of mesoscale rainfall as a random cascade". J. Appl. Meteor. 36, 1296–1303.

Schertzer, D., Lovejoy, S., 2004. Uncertainty and Predictability in Geophysics: Chaos and Multifractal Insights. In: Sparks, R.S.J., Hawkesworth, C.J. (Eds.), State of the Planet, Frontiers and Challenges in Geophysics. American Geophysical Union, Washington, pp. 317–334.

Schertzer, D., Lovejoy, S., Lavallée, D., 1993. Generic Multifractal phase transitions and self-organized criticality. In: Perdang, J.M., Lejeune, A. (Eds.), Cellular Automata: prospects in astronomy and astrophysics. World Scientific, pp. 216–227.

Schertzer, D., Lovejoy, S., Schmitt, F., Chigirinskaya, Y., Marsan, D., 1997. Multifractal cascade dynamics and turbulent intermittency. Fractals 5, 427–471.

Schertzer, D., Lovejoy, S., Schmitt, F., Naud, C., Marsan, D., Chigirinskaya, Y., Marguerit, C., 1998. New developments and old questions in multifractal cloud modeling, satellite retrievals and anomalous absorption. Proc. of the 7th Atmos. Rad. Meas. (ARM) meeting, San Antonio, 3/97, Dept. of Energy, USA, pp. 327–335.

Schmitt, F., Lovejoy, S., Schertzer, D., 1995. Multifractal analysis of the Greenland Ice-core project climate data. Geophys. Res. Lett. 22, 1689–1692.

She, Z.-S., Levesque, E., 1994. Phys. Rev. Lett. 72, 336.

Skamarock, W.C., 2004. Evaluating Mesoscale NWP models using kinetic energy spectra. Mon. Weather Rev. 132, 3020.

Smith, K.S., 2004. Comment on: “The k-3 and k-5/3 energy spectrum of atmospheric turbulence: Quasigeostrophic two-level model simulation”. J. Atmos. Sci. 61, 937–941.

Stolle, J. Space-time Cascade structure of numerical models of the atmosphere. Physics, McGill, Montreal (2009).

Stolle, J., Lovejoy, S., Schertzer, D., 2009. The stochastic cascade structure of deterministic numerical models of the atmosphere. Nonlin. Proc. Geophys. 16, 1–15.

Strauss, D.M., Ditlevsen, P., 1999. Two-dimensional turbulence properties of the ECMWF reanalyses. Tellus 51A, 749–772.

Takayashi, Y.O., Hamilton, K., Ohfuchi, W., 2006. Explicit global simulaiton of the meso-scale spectrum of atmospheric motions. Geophys. Res. Lett. 33.

Talkner, P., Weber, R.O., 2000. Power spectrum and detrended fluctuation analysis: Application to daily temperatures. Phys. Rev. E 62, 150–160.

Taylor, G.I., 1938. The spectrum of turbulence. Proc. R. Soc. Lond. 164, 476–490.

Tchiguirinskaia, I., Schertzer, D., Lovejoy, S., V., J.M., 2006. Wind extremes and scales: multifractal insights and empirical evidence. In: S,, P., Peinke, J. (Eds.), EUROMECH Colloquium on Wind Energy. Springer-Verlag.

Tennekes, H., 1975. Eulerian and Lagrangian time microscales in isotropic turbulence. J. Fluid Mech. 67, 561–567.

Tessier, Y., Lovejoy, S., Schertzer, D., 1994. The Multifractal Global Raingage Network: Analysis and simulation. J. Appl. Meteorol. 32, 1572–1586.

Tessier, Y., Lovejoy, S., Hubert, P., Schertzer, D., Pecknold, S., 1996. Multifractal analysis and modeling of Rainfall and river flows and scaling, causal transfer functions. J. Geophys. Res. 31D, 26,427–426,440.

Tuck, A., 2008. ATMOSPHERIC TURBULENCE: A Molecular Dynamics Perspective. Oxford University Press.

Tuck, A.F., Hovde, S.J., Bui, T.P., 2004. Scale Invariance in jet streams: ER-2 data around the lower-stratospheric polar night vortex. Quart. J. Roy. Meteor. Soc. 130, 2423–2444.

Uppala, S.M., 2005. Quart. J. Roy. Meteor. Soc. 131, 2961.

Van der Hoven, I., 1957. Power spectrum of horizontal wind speed in the frequency range from .0007 to 900 cycles per hour. J. Meteorol. 14, 160–164.

Van Zandt, T.E., 1982. A universal spectrum of buoyancy waves in the atmosphere. Geophys. Res. Lett. 9, 575–578.

Venig-Meinesz, F.A., 1951. A remarkable feature of the Earth-s topography. Proc. K. Ned. Akad. Wet. Ser. B Phys. Sci. 54, 212–228.

Watson, B.P., Lovejoy, S., Grosdidier, Y., Schertzer, D., 2009. Multiple Scattering in Thick Multifractal Clouds Part I: Overview and Single Scattering Scattering in Thick Multifractal Clouds. Physica A 388.

Wheeler, M., Kiladis, G.N., 1999. Convectively coupled equatorial waves: analysis of clouds and temperature in the wavenumber-frequency domain. J. Atmos. Sci. 56, 374–399.

Wilson, J., Schertzer, D., Lovejoy, S., 1991. Physically based modelling by multiplicative cascade processes. In: Schertzer, D., Lovejoy, S. (Eds.), Non-linear variability in geophysics: Scaling and Fractals. Kluwer, pp. 185–208.

Yaglom, A.M., 1966. The influence on the fluctuation in energy dissipation on the shape of turbulent characteristics in the inertial interval. Sov. Phys. Dokl. 2, 26–30.

Yano, J., 2009. Interactive comment on “Reinterpreting aircraft measurements in anisotropic scaling turbulence” by S. Lovejoy et al. Atmos. Chem. Phys. Discuss. 9, S162–S166.

Please cite this article as: Lovejoy, S., Schertzer, D., Towards a new synthesis for atmospheric dynamics: Space–time cascades, Atmos. Res. (2010), doi:10.1016/j.atmosres.2010.01.004